Lawrence Berkeley National Laboratory

Title
CROSSED BEAM REACTIVE SCATTERING OF OXYGEN ATOMS AND SURFACE SCATTERING STUDIES OF GASEOUS CONDENSATION

Permalink
https://escholarship.org/uc/item/0v94d13b

Author
Sibener, S.J.

Publication Date
1979-09-01

Peer reviewed

Lawrence Berkeley Laboratory
UNIVERSITY OF CALIFORNIA

Materials & Molecular
Research Division

CROSSED BEAM REACTIVE SCATTERING OF OXYGEN ATOMS AND
SURFACE SCATTERING STUDIES OF GASEOUS CONDENSATION

Steven Jay Sibener
(Ph. D. thesis)

September 1979

CROSSED BEAM REACTIVE SCATTERING OF OXYGEN ATOMS
AND SURFACE SCATTERING STUDIES OF GASEOUS CONDENSATION

Steven Jay Sibener

Materials and Molecular Research Division
Lawrence Berkeley Laboratory

and

Department of Chemistry
University of California
Berkeley, California 94720

September 1979

ABSTRACT

A high pressure, radio frequency discharge nozzle
beam source has been developed for the production of very
intense ($\geq 10^{18}$ atoms sr^{-1} sec^{-1}) supersonic beams of
oxygen atoms. This source is capable of producing seeded
beams of ground state $O(^3P_J)$ atoms when dilute oxygen-
argon mixtures are used, with molecular dissociation
levels exceeding 80% being realized for operation at
pressures up to 350 torr. When dilute oxygen-helium
mixtures are employed both ground state $O(^3P_J)$ and excited
state $O(^1D_2)$ atoms are present in the terminal beam, with
molecular dissociation levels typically exceeding 60%
being achieved for operation at pressures up to 200 torr.
Atomic oxygen mean translational energies from 0.14 to 0.50
eV have been obtained using the seeded beams technique,

with Mach numbers as high as 10 (FWHM $\Delta v/v \approx 20\%$) being realized.

This beam source has been used to study a wide variety of elementary chemical reactions, under single collision conditions, in crossed beam scattering experiments. To date, reactions involving $O(^3P_J)$ atoms and ICl, CF_3I, CS_2, C_6H_6, C_6D_6, and $C_6H_5CH_3$ have been studied, as have been the reactions of $O(^1D_2)$ atoms with H_2, D_2, and CH_4. In this thesis the ICl, CF_3I, C_6H_6, and C_6D_6 reactions are discussed in detail. The ICl and CF_3I studies have enabled us to determine an improved value for the bond energy of the IO radical: $D_o(IO) = 55 \pm 2$ kcal/mole. The IO product angular and velocity distributions have been used to generate Center-of-Mass flux contour maps, which indicate that these two reactions proceed via relatively long-lived collision complexes whose mean lifetimes are slightly shorter than their respective rotational periods. The experimental product translational energy distributions are compared with theoretical predictions based on the statistical RRKM-AM unimolecular decomposition model. The $O(^3P_J) + C_6H_6$ and C_6D_6 reactions were studied in order to elucidate the reaction mechanism, and, in particular, to identify the primary reaction products produced in these reactions.

After the initial electrophilic attack on the aromatic
ring, the reaction was shown to proceed *via* either
hydrogen (deuterium) elimination or nonradiative decay
of the initially formed triplet biradical to the S_o mani-
fold of phenol. The branching ratio between these two
reaction channels was found to be both isotope and energy
dependent, with the addition channel being favored with
respect to elimination for increasing collision energy
and deuterium substitution. CO elimination was shown
to be a relatively minor reaction channel, if it was
occurring at all.

Finally, a series of beam-surface scattering experi-
ments are described which examined the internal and
translational energy dependence of molecular condensation
probabilities for collisions involving either CCl_4 or SF_6
and their respective condensed phases. It has been con-
clusively demonstrated that excitation of a polyatomic
molecule's rotational and vibrational degrees of freedom
can inhibit its probability of sticking upon impact with
a cryogenically cooled surface. Scattered particle angular
and velocity distributions have been obtained for CCl_4,
SF_6, and Kr which have also permitted a detailed analysis
of energy and momentum exchange to be carried out for

collisions involving these species and their own condensed

phases.

Dedicated to the memory of my sister, Sharon

ACKNOWLEDGEMENTS

It has been both a pleasure and a privilege to study
under the guidance of Professor Yuan T. Lee for the past
four years. His boundless enthusiasm, constant encourage-
ment, and, of course, scientific insight have all left
distinct impressions with me which I shall always fondly
remember. At this time I extend my deepest gratitude to
him for helping make my years at Berkeley a period of
personal growth and scientific enlightenment.

I also wish to thank the many members of Yuan's research
group for their technical assistance, stimulating scientific
discussions, and friendship. Special thanks go to Dr.
Richard J. Buss for introducing me to the many subtleties
of crossed beam experiments, and for his collaboration
on many of the oxygen atom investigations. Dr. Cheuk Ng
is especially thanked for his assistance during my first
year at Berkeley. Many thanks are also extended to my
friends in the Chemistry Department for making these years
actually quite enjoyable and memorable. The friendship,
thoughts, and support offered by Linda Young were of
particular importance to me, as they were a constant joy
to experience and share.

Thanks are also extended to Ms. Ann Weightman for her
considerable patience and efforts during the typing of this
manuscript, and to the technical staff of the L.B.L. glass,

ceramic, machine, and electronic shops for their excellent
support during the course of this research. In particular,
I thank Mr. Dane H. Anderberg of the L.B.L. glass shop for
his expert assistance during the design and fabrication
of the extremely durable quartz nozzles which are used in
the atomic oxygen plasma beam source.

Finally, I extend my most heartfelt thanks to my
parents, and to my late sister, Sharon, for their unfailing
support, encouragement, understanding, and love.

CROSSED BEAM REACTIVE SCATTERING OF OXYGEN ATOMS
AND SURFACE SCATTERING STUDIES OF GASEOUS CONDENSATION

Contents

identify the primary molecular reaction products from isolated bimolecular reactive collisions. This is of especial importance in studying relatively "fast" reactions which involve transient atomic and radical species as the analysis of more traditional bulk kinetic studies can be severely hindered by multiple collisions, which in many instances obscure the primary pathways of these reactions.

Heterogeneous interactions and reactions can also be studied in great detail with modern gas-surface scattering techniques. Here again, as in the gas phase, scattering experiments are unique in that the gas-surface interaction potential can be probed in a very direct way. Several molecular beam laboratories around the world are currently investigating elastic, inelastic, and reactive gas-surface scattering events, with very well characterized surfaces and incident beams, in order to formulate a microscopic description of heterogeneous interactions on the molecular level. Valuable information on gas-surface interaction potentials, and the bound levels these walls support, can be obtained from diffractive scattering experiments in which selective adsorption effects are observed. Structural information about single crystal surfaces, and surfaces containing adsorbed layers, can

also be obtained due to the truly "surface sensitive"
nature of gas-surface scattering experiments. Inelastic
scattering studies can be used to probe a wide variety of
heterogeneous energy exchange processes. There are even
indications that the phonon dispersion relations of clean
surfaces may be obtained from inelastic scattering studies
employing high Mach number beams of either helium or atomic
hydrogen. Perhaps most importantly, the dynamics and
energetics of heterogeneous reactions can be studied in a
very controlled manner, enabling researchers to understand
the factors which dominate heterogeneous reaction kinetics.

Many major technological innovations have occurred
in the past fifteen years which have enabled both crossed
beam and gas-surface scattering experiments to be success-
fully carried out. In addition to the general improvement
of ultra-high vacuum (UHV) technology, the foremost
innovations have been the development by Lee et al.[1] of
extremely sensitive "universal", differentially pumped,
electron bombardment ionizer/quadrupole mass spectrometer
detectors, and the development of a diverse assortment of
high intensity beam sources. Of particular importance in
this regard was the development of supersonic nozzle beam
technology,[2] and the subsequent use of "seeded" beams[3] in
scattering experiments. This allowed intense beams of

relatively narrow velocity dispersion to be routinely generated over a wide energy range, alleviating the need to use relatively low intensity, velocity selected effusive beam sources.

In Chapter II of this thesis the design, construction, and operation of a novel supersonic atomic oxygen nozzle beam source is described in detail. This source has successfully generated atomic oxygen intensities in excess of 10^{18} atoms sr^{-1} sec^{-1}, with mean translational energies spanning the range from 0.14 - 0.50 eV being achieved with the seeded beam technique. In addition to producing $O(^3P_J)$ atoms, this source is capable of generating beams of $O(^1D_2)$ atoms when dilute oxygen-helium mixtures are discharged at high pressures. This capability is at the present time unique, and has allowed crossed beam reactions involving excited state $O(^1D_2)$ atoms to be carried out. To date, the following crossed beam experiments have been conducted in our group at Berkeley:

$$O(^3P_J) + ICl \longrightarrow \underline{IO} + Cl$$
$$CF_3I \longrightarrow \underline{IO} + CF_3$$
$$CS_2 \longrightarrow \underline{SO} + CS$$
$$C_6H_6 \longrightarrow C_6H_5OH, \underline{C_6H_5O} + H$$
$$C_6D_6 \longrightarrow C_6D_5OD, \underline{C_6D_5O} + D$$
$$C_6H_5CH_3 \longrightarrow \text{(under current investigation)}$$

$$O(^1D_2) + H_2 \longrightarrow \underline{OH} + H$$
$$D_2 \longrightarrow \underline{OD} + D$$
$$CH_4 \longrightarrow \underline{CH_3O} + H$$
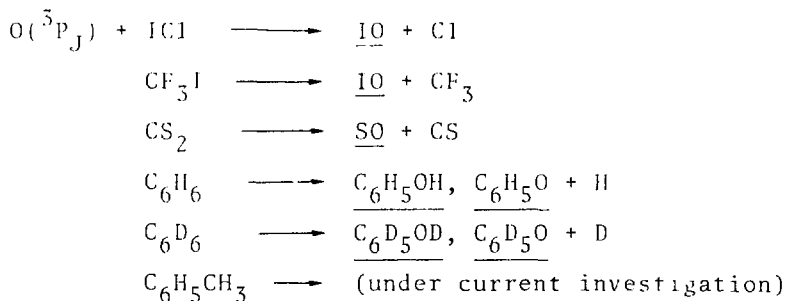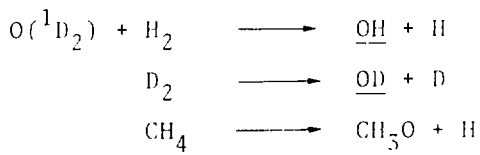
The three $O(^1D_2)$ reactions listed above were the first singlet oxygen atom reactions ever studied in crossed beam scattering experiments.

Chapter III describes the $O(^3P_J) + ICl$ and CF_3I experiments, which were the initial systems studied with the high pressure plasma beam source. These experiments allowed us to determine an improved value for the IO radical's bond energy: $D_o(IO) = 55 \pm 2$ kcal/mole. The IO product translational energy distribution for the CF_3I reaction agrees quite well with RRKM-AM predictions when the above IO bond energy is used in the statistical calculation. Also, the two reactions proceed via collision complexes whose mean lifetimes are slightly shorter than their respective rotational periods. The absence of ClO product in the ICl experiment also seems to indicate that the reaction proceeds adiabatically on a triplet potential surface, and that the least electronegative atom does rest in the central position of the triatomic reaction complex, in agreement with Walsh's electronegativity ordering rule.

The $O(^3P_J)$ + benzene reaction, discussed in Chapter IV, was chosen for inclusion in this thesis as it clearly

demonstrates the utility of the crossed beams method for
unambiguously identifying the reaction products of
elementary reactions. The reaction was shown to proceed
by the initial formation of a triplet biradical adduct,
which subsequently decays *via* either hydrogen elimination
or nonradiative transition to the S_o manifold of phenol.
The branching ratio between these two reaction channels
was found to be both isotope and energy dependent, with
the addition channel being favored with respect to elimina-
tion for increasing collision energy and deuterium sub-
stitution. These experiments also indicated that CO
elimination, if occurring at all, is a relatively minor
reaction channel.

Finally, Chapter V describes a series of gas-surface
scattering experiments which were conducted in order to
study, on the microscopic level, the process of gaseous
condensation. In particular, the translational and
internal energy dependence of molecular sticking prob-
abilities were examined, along with the energy and momentum
transfer characteristics of collisions involving CCl_4,
SF_6 and Kr and their respective condensed phases. These
studies conclusively demonstrate that excitation of a
polyatomic molecule's rotational and vibrational degrees
of freedom leads to an increase in its reflection

probability (decrease in sticking probability) upon
collision with a cryogenically cooled surface, and that
these internal energy effects become increasingly more
important in the limit of low incident translational
energy.

- 8 -

REFERENCES

1. Y. T. Lee, J. D. McDonald, P. R. LeBreton, and D. R. Herschbach, Rev. Sci. Instrum. <u>40</u>, 1402 (1969).

2. J. B. Anderson, R. P. Andres, and J. B. Fenn, in <u>Adv. Chem. Phys.</u>, Vol. 10, J. Ross, Ed. (John Wiley and Sons, New York, 1966), p.275.

3. N. Abauf, J. B. Anderson, R. P. Andres, J. B. Fenn, and D. G. H. Marsden, Science <u>155</u>, 997 (1967).

II. DEVELOPMENT OF A SUPERSONIC $O(^3P_J)$, $O(^1D_2)$ ATOMIC OXYGEN NOZZLE BEAM SOURCE

INTRODUCTION

The interactions and reactions of oxygen atoms are of considerable interest and importance due to the fundamental role they play in combustion processes and atmospheric chemistry. The reactions of ground state $O(^3P_J)$ atoms are of particular interest to researchers studying high temperature combustion processes,[1] laser systems based on the reactions of oxygen atoms which lead to products having vibrationally inverted population distributions,[2] and surface chemistry.[3] A thorough understanding of ground state oxygen atom chemistry is also of immediate practical importance since the space shuttle will orbit the earth at altitudes where the major constituent of the atmosphere is $O(^3P_J)$ atomic oxygen. The reactions of excited state $O(^1D_2)$ atoms are of primary importance due to their major role in the chemistry of the stratosphere.[4] The ability of singlet oxygen atoms to insert in a variety of chemical bonds also makes their chemistry a fascinating subject to explore.[5]

In our laboratory a high pressure, supersonic, radio frequency discharge nozzle beam source has been developed in order to determine the products, energetics, and reaction

dynamics of atomic oxygen reactions in crossed molecular beam scattering experiments. The motivation for constructing this nozzle beam source, rather than relying on much more simple effusive sources, is that supersonic nozzle sources characteristically produce beams of far greater intensity and smaller translational velocity dispersion than effusive sources.[6] The translational energy of nozzle beams can also be varied over a very wide range, from hypothermal to hyperthermal, by using the seeded beam technique.[7] In this technique the peak velocity of the "seed" gas velocity distribution can ideally approach that of the pure "carrier" gas for very dilute gas mixtures. This is accomplished by accelerating or decelerating the seed gas during hydrodynamic expansion through the nozzle by diluting it in either a lighter or heavier carrier gas. Supersonic beams therefore offer several clear advantages over simple effusive sources for conducting dynamical studies in molecular beam experiments.

The successful operation of a discharge beam source depends strongly on the characteristics of its plasma. In particular, the production of a stable and efficiently coupled high pressure discharge for the generation of atomic species is much more difficult than the production of a low pressure (~1 torr) discharge. Impedance matching

of the plasma to the radio frequency power source as a
function of gas pressure, temperature, and composition is
required. Plasma localization directly behind the orifice
must also be achieved in order to limit atomic recombina-
tion before the expansion. Sufficient cooling of the
nozzle in order to prevent melting of its orifice, and
to limit atomic recombination at the nozzle walls (while
not interfering with power coupling to the plasma) is
mandatory. Finally, the high pressure plasma must operate
in a stable, reproducible, and uniform discharge mode
(no beads or streamers) whose temperature is sufficiently
high to generate atomic species, but not high enough to
melt the orifice of the nozzle. The beam source described
in this paper meets all of the above criteria. A 'oron
nitride skimmer is used and is found to be completely
stable with respect to the seeded atomic oxygen beam.

Other high pressure atomic oxygen beam sources have
been previously reported in the literature. Miller and
Patch[8] have described in detail a radio frequency dis-
charge beam source which produces ~35% dissociation at
60 torr for a 5% oxygen-helium mixture. Gorry et al.[9]
have reported a microwave discharge source with dissocia-
tion characteristics similar to those of Miller and Patch.
The impedance matching scheme, nozzle construction and,

in particular, plasma localization techniques described
in this paper permit a higher degree of molecular dissocia-
tion to be achieved at significantly higher operating
pressures than the sources mentioned above. The current
limitation on the atomic oxygen beam intensity produced
by our source is not atomic recombination at high pressures
but rather the speed of the diffusion pump which backs the
source region. In some cases the characteristics (for
example, gas temperature) of the high pressure plasmas
we have generated to date also become a concern when
pressures exceeding 400 torr are used. The source has
been operated at pressures exceeding 200 torr for oxygen
helium mixtures with greater than 50% molecular dissocia-
tion, producing atomic oxygen intensities of $\geq$ 5 x 10^{18} atoms
sr^{-1} sec^{-1}. Oxygen-argon mixtures have been discharged at
pressures exceeding 300 torr with greater than 80% dissocia-
tion, and with measured atomic oxygen intensities of ca.
5 x 10^{17} atoms sr^{-1} sec^{-1}.

The beam source described in this paper was originally
designed in order to produce intense supersonic beams of
ground state $O(^3P_J)$ atoms. However, we find that when
dilute oxygen-helium mixtures are discharged the beam is
composed of a mixture of atomic quantum states including
excited state $O(^1D_2)$ atoms. The concentration of $O(^1D_2)$
atoms in this beam has proven to be of sufficient magnitude

to permit the study of $O(^1D_2)$ reactions in crossed molecular beam experiments. This exciting development will eliminate the need to use powerful and expensive UV pulsed lasers for the photodissociative production of $O(^1D_2)$ atomic beams when the presence of other chemical species in the beam, such as $O(^3P_J)$ and $O_2(^1\Delta_g)$, will not seriously complicate the chemistry under study.

SOURCE DESIGN AND CONSTRUCTION

A cross-sectional view of the source mounted in the differential pumping region of our universal scattering machine is shown in Fig. 1, with an enlarged view of the internal source components and nozzle tip appearing in Fig. 2. The important design and construction consider-ations which led to this final form of our plasma beam source will now be discussed.

A.   Nozzle Construction

The first question to be dealt with was that of nozzle material.   Quartz and alumina were the two materials con-sidered based upon their relatively high melting points. Initially 99.8% purity alumina tubes[10] with laser drilled holes were tested.   They were unsatisfactory for two reasons.

They tended to crack when subjected to large thermal
gradients, and arcing occurred between the outer surface
of the alumina tubes and the radio frequency coupling
coil whenever the outer diameter of the tube came into
physical contact with the coil. After this brief test
period it was decided that quartz nozzles would have to
be fabricated. The final shape of these nozzles can be
seen in Fig. 1(c) and Fig. 2(c). A water cooling jacket
was incorporated in our final nozzle design to prevent
the quartz orifice from melting and enlarging during
the expansion of the extremely hot gas mixture. The
nozzle tip geometry shown in Fig. 2(L) was ultimately
found to be stable with respect to orifice enlargement.
Here the water coolant flows directly over the junction
between the inner, plasma containing tube (6 mm O.D.
commerical grade fused quartz, 1 mm wall thickness, as
bubble free as possible) and the quartz water jacket
(12 mm O.D., 1 mm thick). The short tip on the front
of the inner tube is approximately 1 mm long and allows
the coolant to flow as close as possible to the orifice.
This is important due to the poor thermal conductivity
of quartz. In addition to preventing melting of the nozzle,
water cooling is also desirable since the efficiency of

quartz to promote atomic oxygen recombination decreases
with lower surface temperatures.[11]

Low electrical conductivity water of 5 μmho/cm con-
ductivity is used as the nozzle coolant and is flowed
through the concentric water jacket at a rate of 10 cm^3/sec.
Use of regular conductivity water as the coolant is pre-
cluded due to excessive radio frequency power loss to the
water. As an added benefit, the cooling jacket completely
eliminated the arcing problem mentioned above. This arcing
was found to occur for both alumina and quartz plasma
containing tubes which were not physically separated from
the coil by another insulating layer.

The nozzle fabrication procedure is quite reproducible
and is briefly outlined here. The graded seal water inlet
and outlet arms along with their solid quartz support rod
(Fig. 2, E,G,H,I) are initially assembled and put aside for
later use. Next, the inner tube is prepared. This pre-
paration consists of three operations: Flaring one end just
to clear the I.D. of the outer tube, creating the import-
ant tip on its front end (Fig. 2, L), and fusing three
small quartz physical support standoffs to the inner tube.
These three small "droplets" of quartz should be placed at
120° with respect to each other and positioned from 6-7.5
cm from the tip. They should be sized just to clear the

I.D. of the outer tube and will be used to hold the inner tube concentric with the water jacket. The inner tube assembly is then slid inside of the outer tube with the outer tube extending past the inner front tip by about 5 cm. At this time the three inner tube support standoffs are fused to the I.D. of the outer tube and should be adjusted until the two tubes are concentric. A ring seal is then made between the flared rear end of the inner tube and the outer tube. Quartz tubulations are then blown onto the outer tube which will ultimately be attached to the water coolant arms. Next, the 5 cm outer tube exten-sion is pared off with a torch and a carbon tool. The objective of this is to create a 1 mm thick quartz face which seals off the front of the outer tube without touch-ing the tip of the inner tube. This front surface should be as perpendicular as possible to the concentric tube axis and should be just shy of touching the inner tip. The assembly is completed by joining the inner tip and the newly created quartz nozzle face with a ring seal.

At this point the most critical stage of the nozzle fabrication procedure is carried out. The nozzle assembly, with the water arms still detached, is mounted in a glass-blower's lathe. The orifice is now blown on a spinning lathe in an operation requiring two people. Using a

hydrogen-oxygen flame the front face of the nozzle is
heated at a wide angle until the quartz is ready to be
blown.   The flame is then quickly removed and a hole is
blown in the tube.   This hole should be slightly larger
than the desired diameter of the nozzle orifice.   One
person now locally heats the tip of the quartz nozzle
while the other simultaneously views the hole diameter
with a 60X power measuring microscope.   The hole is allowed
to shrink slowly until the desired diameter is reached.
Hole size readjustment can be carried out with this pro-
cedure until the orifice is within 0.005 mm of the desired
diameter.

       When an orifice of the desired size is obtained its
straightness is always checked by placing a small positive
pressure of oxygen behind the nozzle.   This produces a
small oxygen jet at the orifice.   The shape profile of this
jet is then made visible by aiming a small gas torch at the
jet while the entire nozzle is rotated in the lathe.   If
any wobble or precession of the flame jet is detected
the orifice is reblown.   We consistently find that the
straightest orifices are produced by shrinking a larger
diameter hole down to the proper size rather than by
enlarging a hole which is too small.   Nozzle diameters
are typically 0.076 mm for ogyxen-argon discharges and

0.191 mm when oxygen-helium mixtures are used. The reasons
for using two differently sized nozzles will be covered in
the next section of this paper. Nozzle assembly is then
completed by attaching the coolant inlet and outlet arms
to the water jacket and by briefly etching the inner quartz
tube with a dilute solution of hydrofluoric acid. This
acid rinse is believed to inhibit atomic recombination on
the walls of the tube.[12]

B. Electrical Design

Two distinct radio frequency circuit arrangements can
be used for generating electrodeless discharges in gases.[13]
One arrangement involves the use of a self-excited power
oscillator. In this configuration the tube containing
the gas to be discharged is placed through the tank coil
of a free running power oscillator. Large amounts of radio
frequency power can be coupled to a discharge in this manner,
but it is inherently inefficient and can pull out of
oscillation as the circuit loading changes. Loading varia-
tions can occur when the pressure of the discharge is
varied over several hundred torr. Its most serious draw-
back is that impedance matching between the plasma and the
oscillator's circuitry, while the oscillator is in opera-
tion, is very difficult to achieve. The other circuit

option, and the one which we have adopted, uses a driven
oscillator-amplifier arrangement in which a variable fre-
quency oscillator is separated from the load by one or
more stages of amplification. In this manner the oscillator
is very well isolated from load variations induced by
changing plasma characteristics. More importantly, this
arrangement allows the impedance of the gaseous discharge
to be carefully matched to that of the radio frequency
electronics. This ensures efficient use of the available
radio frequency power. It also offers the desirable option
of separating the electronics from the plasma coupling LC
tank circuit.

The radio frequency (hereafter, RF) power for our
beam source is supplied by a Viking Valiant radio trans-
mitter which can deliver a maximum output of 140 watts
over a continuously variable frequency range several hun-
dred kilohertz wide, centered at 14 MHz. (It is difficult
to obtain wide fequency tunability in the coupling tank
circuit of this beam source at frequencies significantly
higher than 25 MHz due to the stray capacitance associated
with its physical layout.) When higher power levels are
required a linear amplifier capable of providing RF output
levels of up to ca. 750 watts is used. However, RF levels
exceeding 200 watts are rarely needed due to the highly

efficient impedance matching scheme which is employed.
The plasma coupling tank coil and capacitor can be seen
in Fig. 1. The variable air capacitor (Bud #1615, 0-75
pf, 0.762 cm airgap) is mounted outside of the vacuum to
facilitate the initial frequency matching of the coupling
tank circuit to the electronics. A grid dip meter is
used for this preliminary tuning of the beam source.

A novel impedance matching scheme is used which
enables the source to operate routinely at a standing
wave ratio (SWR) of less than 1.05:1. Impedance matching
is necessary since the effective plasma impedance which
varies as a function of plasma condition, is much larger
than the 50 ohm output impedance of the electronics.
Figure 3 shows a schematic outline of the impedance
matching circuitry which can best be understood when
viewed in two stages. First, a variable group tap on
the tank coil (Fig. 2,A) is used to produce a large
stepdown of the plasma impedance, as seen by the RF
electronics, ideally to 50 ohms. This large stepdown
of the plasma impedance is accomplished with the coupling
coil-ground tap arrangement acting as an RF autotransformer.
Since this is an RF circuit, the impedance transformation
(for a uniformly wound coil) goes only approximately[14] as
the square of the turns ratio, $(N/n)^2$, where N is the total

number of coil turns and n is the numbers of turns from
the rear of the coil to the ground tap. This impedance
transformation creates a large voltage stepup at the
front of the coil (nearest the nozzle tip) and necessi-
tates the use of a high voltage ceramic feedthrough for
the RF return, as is shown in Fig. 1,J. This large,
but approximate impedance transformation allows the RF
power to be delivered to the beam source from a remote
location by RG-215/U coaxial cable. In a procedure which
must be carried out only once when the source is first
constructed, the source must be repeatedly tested with
the position of the ground tap varied in order to deter-
mine optimum placement of the ground tap. This placement
is found by noting the tap location which minimizes the
standing wave ratio between the final RF amplification
stage and the tank circuit. For the source geometry shown
in Fig. 1 the optimum tap locations are 2-1/4 turns from
the rear end of the coil for discharging oxygen-helium
mixtures at 200 torr, and 2-1/2 turns from the rear end
for oxygen-argon discharges operated at up to 350 torr
total pressure. Standing wave ratios are always less than
3:1 with these tap locations and are frequently much
lower.

Next, a PI-network, series capacitor arrangement is
used to critcially fine tune the impedance match until
standing wave ratios of 1.1:1 or less are achieved. This
circuit arrangement represents a quite diverse impedance
matching scheme in that the PI-network can be used to
match purely resistive load mismatches while the series
capacitor can be used for tuning out any reactive impedance
components presented to the RF electronics by the plasma
coupling tank circuit. We find that the circuit impedance
changes when the plasma is first started, varies rapidly
as the nozzle pressure is raised from 1 to about 50 torr,
and then varies more slowly as the pressure is further
raised to several hundred torr. It is also found to vary
with RF power level and gas composition. These impedance
variations arise from the changing reactance of the coupl-
ing coil, which can be attributed to the changing perme-
ability of the region inside the tank coil. In the
original design and testing of this circuit a highly vari-
able PI-network, series capacitor arrangement was con-
structed having an intended circuit Q of 10. The equations
used for the design of the PI-network[15,16] were (for $R_1 >$
R_2):

$$X_{C1} = \frac{R_1}{Q} \tag{1}$$

$$X_{C2} = R_2 \sqrt{\frac{R_1/R_2}{Q^2+1 - (R_1/R_2)}} \tag{2}$$

$$X_{L1} = \frac{QR_1 + (R_1R_2/X_{C2})}{Q^2 + 1} \tag{3}$$

where X_{C1}, X_{C2}, and X_{L1} represent the reactances of the components shown in Fig. 3, R_1 and R_2 represent the impedances of the tank circuit and RF electronics, respectively, and Q is the quality factor of the matching network. Particular attention should be focused on R_1 in the above equations, noting that it is related to the stepped-down resistive impedance of the gaseous discharge. The series capacitor, C3 in Fig. 3, completes the impedance matching circuitry and is varied during the SWR minimization procedure in order to eliminate any reactive components of the tank circuit impedance. In the initial design of this circuit both C1 and C2 were variable up to 750 pf and were comprised of several high voltage ceramic and air variable capacitors which were connected in parallel. Also in the initial design, capacitor C3 was variable up to 250 pf while the inductor, L1, had a maximum calculated inductance of 6.9 µH. It consisted of a 7.6 cm diameter by 15.2 cm long, 15 turn tapped coil which was constructed out of 0.64 cm diameter copper tubing. The tap could be attached to

the coil in 30 positions distributed evenly along the length of the coil, making LI values well below 1 μH possible. This circuit worked very well but was eventually replaced (for ease of operation) by a slightly modified, commerically available network.[17] In this commerical unit C1 and C3 are 20-245 pf air variable capacitors, C2 is variable in discrete jumps up to 2160 pf, and LI consists of a 5.1 cm diameter by 9.1 cm long, 9 turn coil which is tapped on its fifth turn for 14 MHz operation. The tuning of these impedance matching circuits is greatly facilitated by the continuous use of in-line RF watt-meters and a standing wave ratio bridge. Power coupling to the plasma is found to be extremely efficient (≥ 99%) and power levels must be carefully limited in order to avoid melting the orifice of the quartz nozzle. Stray RF fields radiating from the source have been minimized by completely enclosing the top of the beam source with electrically grounded copper mesh.

Figure 4 shows a block diagram of the RF circuitry. Note that the beam source is always operated in a doubly interlocked condition. Nozzle meltdown protection is provided by a paddlewheel flow switch[18] which can quickly turn off the RF power should the nozzle coolant flow rate drop below a predetermined level. Similarly, the RF

electronics are protected by a fast electronic meter relay
which has been incorporated into an SWR bridge circuit.
This relay can rapidly turn off the RF power when the SWR
rises above some preset value, which is usually chosen
as an SWR of 2.5:1.

Finally, we have been successful in localizing the
plasma directly behind the orifice of the nozzle. This
spatial localization of the plasma is of critical importance
if an atomic beam of high molecular dissociation is to be
produced from a high pressure discharge. Without this
plasma localization at the nozzle tip extensive atomic
recombination would occur. The localization has been
achieved by placing around the nozzle tip (outside of the
water jacket and *not* along the front face of the nozzle)
a carefully shaped, electrically grounded block of aluminum
(Fig. 2,J). The discharge appears to change gradually
from an inductively coupled plasma at low pressures to a
capacitively coupled discharge at high pressures. This
coupling at high pressures occurs beween the front, small
diameter tank coil turns, and the grounded aluminum block.
As this coupling becomes stronger the plasma localizes
towards the front of the discharge tube. Photographic
studies have shown that the discharge region protrudes
past the front plane of the grounding block and actually

extends up to the nozzle tip, ensuring a high degree of
molecular dissociation directly behind the nozzle at high
pressures.

The tank coil (Fig. 2,D) has been differentially
wound in order to further localize the plasma and to
increase its energy density at high pressures. The first
6-1/2 coil turns nearest to the nozzle tip are 1.37 cm
I.D. by 6.0 cm long while the 5 large turns are 5.08 cm
I.D. by 6.5 cm long. The larger turns decouple from the
plasma as the pressure is raised, and therefore the energy
density of the localized plasma is considerably increased.
The coil is constructed of 0.32 cm O.D. copper tubing and
was wound around correctly sized metal tubes on a low-
speed lathe. The small diameter coil windings should be
uniformly spaced and carefully shaped in order to avoid
any inhomogeneities in the RF field. These inhomogeneities,
if present, can cause the uniform plasma to collapse into
streamers at high pressures. The coil is water cooled
with low electrical conductivity water at a flow rate of
4 cm^3/sec in order to improve the long term mechanical,
and hence electrical, stability of the tank circuit. Also
note that the entire tank circuit, as seen in Fig. 1, is
floated with respect to electrical ground. That is re-
quired if the RF coupling and localization schemes, as
described here, are to be effectively used.

The pumping requirements for this beam source vary greatly depending upon the gas mixture which is to be used. It was originally pumped by a 4200 l/sec diffusion pump which was separated from the source by a sliding gate valve. This pumping arrangement was recently replaced by an 8000 l/sec pump which was directly joined to the source. This large pumping speed is desirable while running high pressure oxygen-argon mixtures, for which the pressure must be kept below 7×10^{-5} torr. For higher background pressures the RF power decouples from the nozzle and a glow discharge of the entire source region occurs. This glow discharge is a problem which currently constrains the nozzle orifice diameter to 0.075 mm for gas mixtures containing argon. Nozzle pressures exceeding 350 torr have been successfully run with argon as the carrier gas. Helium seeded beams do not have this operational constraint. This allows much larger orifices to be used for helium seeded beams operating at high nozzle stagnation pressures, provided that sufficient pumping speed is available for backing the foreline of the diffusion pump.

Significant effort was also devoted to fabricating a skimmer which would not degrade when exposed to the atomic oxygen beam. Skimmers made of electrically conducting

materials, including stainless steel, were not stable over long time periods due to sputtering by high energy ions. Apparently, ions emanating from the nozzle were being accelerated towards the ground potential of these metallic skimmers. Boron nitride[19] skimmers with 0.81 mm openings were found to be completely stable with respect to the oxygen beam. The electrical insulating properties, machinability, and density of boron nitride actually make it an ideal skimmer material for use with this beam source.

C. Source Operation

The tuning and operating of the beam source is quite straightforward. The plasma coupling tank circuit should first be tuned to the desired resonant frequency by adjusting the tank circuit's variable air capacitor, which is mounted on top of the beam source. The resonant frequency of this circuit can be easily monitored by placing the probe of a grid dip meter adjacent to the tank circuit capacitor, which is conveniently located outside of the vacuum. During this tune-up procedure the coaxial cable which brings the RF power to the source should be disconnected from the source to ensure correct tuning of the circuit. Next, the RF power should be turned on (~100 watts) with the impedance matching network and high power amplifier temporarily bypassed, and with the

nozzle evacuated to $\leq$ 1 torr. The variable frequency
oscillator is then varied until the SWR between the beam
source and the electronics is minimized. If the discharge
is not ignited when the SWR minimum is reached the RF
power should be quickly switched off and then on again.
Invariably the discharge will be ignited by this procedure.
Gas should now be flowed into the nozzle while simultane-
ously retuning the oscillator's frequency to maintain the
SWR at a minimum. When pressures on the order of 100 torr
are reached, the RF power level may be safely increased to
sustain the discharge at higher pressures. The pressure
may then be further increased, again with the simultaneous
retuning of the RF electronics, until the final operating
pressure is reached. We consistently find that the
resonant frequency of the plasma coupling circuit increases
slowly with increasing gas pressure. As an example of
this, a 5% O_2-He, 130 watt discharge is found to require a
0.006 MHz frequency increase when its pressure is raised
from 120 to 220 torr. At this point the plasma should be
switched off, the gas mixture in the beam source evacuated,
and then the impedance matching circuitry along with any
high power amplifiers inserted in-line. The source can
now be reignited and tuned for optimum performance
at high RF power levels. After a few minutes of
operation at the final power and pressure settings the

electronics should again be slightly retuned to correct for any drift during this initial stabilization period. It should be clearly stated here that the minimum SWR which can be achieved *before* the matching network is connected is completely dependent on the placement of the coupling coil's ground tap (Fig. 2,A). As was discussed earlier, the correct location for this tap must be found in a trial and error process which need be done only once when the source is initially constructed.

After the overall tuning procedure has been completed the source can be operated without further major retuning for a period lasting several weeks. Typically the source is turned on by evacuating the nozzle to about 1 torr, switching on the RF power, and rapidly increasing the pressure to the desired operating level. Within a few minutes of reigniting the discharge the operating characteristics always return to their steady state value. Most importantly, the beam characteristics are extremely reproducible for day to day operation of the source, allowing experimental scattering data to be taken over a period several weeks long if necessary, without concern for fluctuating beam characteristics. The quartz orifice does not enlarge at all when the source is operated at the power levels discussed in the next section of this

paper. However, sputtering of the front surface of the quartz nozzle does place a lmit on the lifetime of any given nozzle. This sputtering results when ions which leave the nozzle are accelerated back towards its front surface by the large RF fields present in that region. Periodic visual inspections of the nozzle tip are carried out to monitor the nozzle degradation. The nozzles are replaced when the sputtering errosion becomes severe. They can be recycled by rebuilding the nozzle face and reblowing the orifice. Some of the ions which emanate from the nozzle actually pass through the skimmer. These are deflected out of the beam by a 5000 V/cm deflecting field which is placed before the collision region of our apparatus (Fig. 1,N). The beam characteristics for different nozzles operated under the same conditions have been found to be fairly repr ducible, with slight differences in Mach number and peak velocity being noted. These differences can be attributed to the slight coil shape and positioning changes which invariably occur during each reassembly of the beam source.

BEAM CHARACTERIZATION

A.   Confirmation of Atomic Oxygen Production

The atomic oxygen beams produced by this beam source
have been thoroughly characterized in order to improve
our understanding of the source's operation and to
optimize its performance. A wide variety of diagnostic
techniques have been used for this analysis. Chronologic-
ally, our first goal was to experimentally verify the
presence of oxygen atoms in the terminal beam. This was
unambiguously demonstrated by measuring the differential
elastic scattering cross section for O-He and O_2-He in our
universal crossed molecular beam apparatus.[20] In these
measurements the elastically scattered mass 16 and mass 32
number densities were recorded, with the discharge on, when
the oxygen beam was crossed at 90° with a supersonic beam
of pure helium. For this preliminary experiment a 5%
O_2-Ar mixture was discharged in the source at 95 torr total
pressure by 95 watts of RF power. The Newton velocity
diagrams[21] for these two collision systems are shown in
Fig. 5a, and clearly reveal how the presence of atomic
oxygen in the terminal beam can be confirmed by these
experiments. They show that the heavier molecular oxygen
is kinematically constrained to scatter within a LAB angle

of approximately 24° while the lighter atomic oxygen, if
present in the beam, could be scattered to 44° in the
LAB reference frame. These differential cross sections
would also be expected to have a rather broad peak in
the vicinity of these cutoff angles due to the nature of
the transformation Jacobian which relates the LAB and
Center-of-Mass reference frames. Figure 5b shows the
experimentally measured differential elastic cross sections
for these two systems. The mass 16 (O-He) scan can be seen
in this figure to have a qualitatively different shape from
the mass 32 (O_2-He) scan. This difference indicates that
the mass 16 signal does not exclusively come from the
dissociative ionization of elastically scattered molecular
oxygen in the ionizer of our quadrupole mass spectrometer.
More importantly, the mass 16 scan does in fact peak and
begin to fall off around 40° while for the mass 32 scan
this occurs at 20°, in excellent agreement with the shapes
predicted from the most probable Newton diagrams shown in
Fig. 5a. The experimental curves actually extend past the
predicted cutoff angles due to the finite spread of
velocities in the two beams. The O-He experimental curve
shown in Fig. 5b has been corrected for the dissociative
ionization of elastically scattered molecular oxygen. We

conclude from the above data that oxygen atoms are
definitely present and, in fact, they are more abundant
than oxygen molecules in the terminal beam produced by
our high pressure, RF discharge beam source.

E.   Molecular Dissociation

The extent of O_2 dissociation in the terminal beam
has been carefully measured for several oxygen rare gas
mixtures as a function of gas pressure and RF power.
These measurements were made in our crossed beam apparatus
with the triply differentially pumped mass spectrometer
looking directly along the beam axis. The relative O
and O_2 number densities were actually measured by inter
grating the time-of-flight spectra of masses 16 and 32.
We have opted to integrate these time-of-flight spectra
rather than use our usual particle counting electronics
in order to eliminate any possible contributions from
VUV photons and high energy ions in the detected signals.
This separation of the true signal from VUV photon and
high energy ion contributions can easily be made in the
time regime with our time-of-flight (herafter, TOF)
instrumentation since the interferring factors always
have much shorter flight times that the true signal. The
ion deflecting field mentioned earlier was held at a field
strength of 5000 V/cm during these measurements and was

found to deflect virtually all of the ions emanating from the beam source. Only during very high power operation of the beam source did a few high energy ions apparently reach the detector.
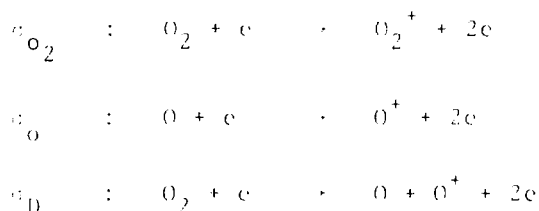
The TOF apparatus used in these studies consisted of a 17.78 cm diameter aluminum disk having four equally spaced 0.5 mm or 1.0 mm slots around its circumference. The disk was rotated at either 300 or 350 Hz during data acquisition. The detector aperature was narrowed to 0.125 mm diameter, and the distance between the TOF disk and the electron bombardment ionizer was 18.4 cm. The ionizer and quadrupole mass spectrometer have been previously described in detail,[20] and the ionizer's emission current was set sufficiently low to eliminate any space charge perturbations of the detected signal intensities and velocity distributions. A 256-channel scaler interfaced to an on-line NOVA minicomputer was used to record signal intensity as a function of flight time. The scaler was usually set at 2 μs dwell time for the helium mixtures and 4 μs for the argon mixtures.

The extent of molecular dissociation in the terminal beam was calculated with the following two equations:

$$R = \frac{N_O}{N_{O_2}} = \frac{(\sigma_D/\sigma_{O_2})}{\eta} \left(\frac{\sigma_{O_2}}{\sigma_O}\right) \left(\frac{I_O - \eta I_{O_2}}{I_{O_2}}\right) \qquad (4)$$

$$\text{Percent Dissociaton} = \frac{R}{R+2} \tag{5}$$

where I_0 and I_{0_2} are the experimentally observed mass 16 and 32 number densities, $\cdot$ is the experimentally observed I_0/I_{0_2} count ratio with the discharge off, and the cross sections represent the following processes:

$$\sigma_{0_2} \quad : \quad O_2 + e \quad \cdot \quad O_2^+ + 2e$$

$$\sigma_0 \quad : \quad O + e \quad \cdot \quad O^+ + 2e$$

$$\sigma_D \quad : \quad O_2 + e \quad \cdot \quad O + O^+ + 2e$$

For ionization with 250 eV electrons: $\sigma_{0_2} = 1.52 \text{ Å}^2$, $\sigma_0 = 1.15 \text{ Å}^2$, and $\sigma_D = 0.88 \text{ Å}^2$.[22,23] In their paper Miller and Patch[8] have used an equivalent expression for R, and have discussed the approximations and assumptions leading to the use of equations (4) and (5). The $(\sigma_D/\sigma_{0_2})/n$ term corrects for any differential detection of masses 16 and 32 by our detector. This difference in detection probability, if present at all, is partially due to the differential transmission of m/e = 16 and 32 through the quadrupole mass filter of our detector.

Figure 6 shows the pressure dependence of O_2 dissociation for four oxygen-rare gas mixtures under a variety of

RF power settings. These curves reveal the unique operating characteristics of this beam source. The molecular dissociation is seen to depend only weakly on the nozzle stagnation pressure, varying only a few percent over a several hundred torr pressure range. The actual extent of molecular dissociation in the beam is also found to be quite high over this large pressure range. Argon seeded mixtures regularly achieve moelcular dissociation levels of 80-90% while helium seeded mixtures operate with 50-65% dissociation. The weak pressure dependence and high dissociation levels described here can undoubtedly be attributed to the spatial localization of the plasma at the tip of the quartz nozzle. The dissociation percentages shown in Fig. 6 have been found to be reproducible to within about 5% for data taken over a several month time period with many different nozzles. Further examination of the curves shown in Fig. 6 indicates that the dissociation versus pressure curves for identical gas mixtures discharged by different RF power levels have similar slopes, with the higher power curves shifted to slightly greater dissociation. The 10% oxygen mixtures also appear to exhibit slightly lower dissociation values than their more dilute counterparts.

Figure 7 shows even more clearly the effect of RF power and O_2 concentration on molecular dissociation.

Increasing the RF power from 130 to 195 watts is seen to raise
the dissociation level by at most 10% for three different
gas mixtures. The two upper curves of this figure also
show that the extent of molecular dissociation is only
mildly influenced by raising the O_2 concentration from
5% to 10% when argon is used as the carrier gas. The 10%
O_2-Ar mixture is seen from Fig. 7 to exhibit the same RF
power dependence as the 5% O_2-Ar mixture, with its dissoci-
ation precentage lower by about 10%.

The information related in Figs. 6 and 7 has been very
useful for optimizing the performance of our oxygen atom
beam source. The very weak pressure dependences shown in
Fig. 6 indicate that the nozzle stagnation pressure should
be held as high as possible, subject to the limitations of
plasma stability and pumping speed availability, without
worry of severe recombination. These figures also tell us
that 10% O_2-rare gas mixtures should be used rather than
more dilute mixtures in order to increase the flux of
oxygen atoms leaving the nozzle. Finally, Fig. 7 informs
us that power levels approaching 200 watts should be quite
adequate for dissociating molecular oxygen in seeded argon
and helium gas mixtures. This is fortunate since power
levels exceeding 200 watts lead to orifice enlargement
when argon is used as the carrier gas. Power levels

exceeding 200 watts also appear to accelerate the quartz sputtering rate at the nozzle face for all gas mixtures tested.

C. Velocity Analysis

The true, undistorted atomic oxygen velocity distributions produced by our beam source have been recovered from the convoluted experimental TOF distributions by correcting the observed spectra for instrumental broadening effects (shutter function and finite ionizer length) and ion flight time offset. The peak velocity and Mach number of these distributions have been found to vary with both nozzle stagnation pressure and RF power level. Figure 8 indicates the dependence of peak velocity on nozzle pressure for seven different gas mixture - RF power combinations. The effect of seeding is immediately apparent here, with the oxygen seeded in helium beams having much higher velocities than the oxygen seeded in argon gas mixtures. The mean energy of the atomic oxygen beams generated in our laboratory span the range from 0.1 - 0.5 eV, with the highest energies being obtained for 5% O_2-He mixtures discharged with 200 watts. The shape of the curves shown in Fig. 8 indicates that velocity "slippage" occurs between the oxygen and carrier gases during the hydrodynamic nozzle expansion. Velocity slippage occurs when

the collision frequency is too low during the nozzle expansion to effect complete momentum and energy equilibrium between the seed and carrier species. Slippage is especially typical of low pressure, high temperature expansions due to the relatively low number density these systems have in the vicinity of the nozzle orifice. When slippage occurs it can usually be minimized by increasing the pressure behind the nozzle, which increases the number of collisions which occur during the expansion. This behavior is clearly seen in Fig. 8. The mixtures having helium as the carrier gas have their atomic oxygen peak velocities steadily *increasing* with increasing pressure until their terminal velocities are reached at pressures *approaching 150-200 torr.* The mixtures having argon as the carrier gas behave oppositely from this, with their peak oxygen velocities *decreasing* with increasing pressure until their terminal velocities are reached between 250 and 300 torr. The above behavior is expected since helium serves to accelerate atomic oxygen while argon decelerates atomic oxygen during coexpansion from the nozzle.

The influence of RF power on beam velocity has also been studied and is shown in Fig. 9 for four gas mixtures. In all cases the atomic oxygen velocity is found to increase monotonically with increasing RF power. This in turn

indicates that the effective plasma temperature does in
fact rise with increasing RF power. The translational
energy of the beam can therefore be tuned over a narrow
energy range about 0.1 eV wide by simply varying the RF
power used to run the discharge. This tunability may apply
to an even broader energy range when power levels exceeding
200 watts are used for running oxygen-helium mixtures.

In these experiments the raw TOF data is always
recorded as number density versus flight time. However,
TOF spectra are more readily interpretable when displayed
as flux versus velocity spectra. A typical TOF spectra
is shown in Fig. 10 which represents the velocity distri-
bution of a fast atomic oxygen beam. The correct Jacobian
transformation, $1/v^2$, was used for converting this and
other spectra from time space to velocity space, while the
resulting distributions were then multiplied by v to effect
the conversion from number density to flux. The oxygen
seeded in helium distribution shown in Fig. 10 has a FWHM
of 19% with a Mach number of 9.2 as calculated by a para-
metric fit to the deconvoluted distribution.[24,25] This
should be compared to the width of an effusive beam whose
velocity distribution is Maxwellian. Numerical solution
of the transcendental equation which defines the two half
intensity velocities of the distribution $I(v) \propto v^3 \exp(-v^2/\alpha^2)$

shows that the FWHM of a Maxwellian flux distribution is
95%. The relatively narrow velocity distributions pro-
duced by this beam source are one of its most important
characteristics, and are in general indicative of beams
produced from supersonic nozzle expansions. The slower
oxygen seeded in argon beams have typically 40% FWHM
distributions with Mach numbers ranging from 3 to 4. In
the future the use of neon rather than argon as the beam
carrier gas may enable narrower moderate energy beams to
be produced due to the smaller mass mismatch which exists
between neon and atomic oxygen relative to that of argon.

The terminal Mach number of a beam is a parameter
which is frequently used for characterizing the width of
its velocity distribution. It is defined as the ratio
of the mass flow speed to the local speed of sound in the
beam, v/c, where $c = (\gamma k T_b/m)^{1/2}$, γ is the usual ratio of
specific heats at constant pressure to constant volume,
and T_b is the temperature of the beam in the reference
frame moving with the bulk velocity, v. For seeded gas
mixtures which are expanded in the hydrodynamic regime
(Knudsen number < 1) collisions with the carrier gas initially
accelerate or decelerate the seed gas depending on whether
the carrier gas is lighter or heavier than the seed gas,
respectively. Subsequent collisions during the expansion

then serve to "cool" the seed gas and to narrow the width
of its velocity distribution.[26]   The total number of
binary collisions which occur during the expansion is
proportional to $n_0 D$, the product of the particle number
density at the orifice with the orifice diameter.   Figures
11 and 12 show how the atomic oxygen Mach number varies
respectively with nozzle stagnation pressure and RF power
for several operating conditions of the beam source.   The
nearly linear Mach number versus pressure curves shown in
Fig. 11 indicate that the cooling process does vary as
described above, and is not complete.   It is clear from
the slope of the curves shown in Fig. 11 that further
velocity distribution narrowing should be possible for
operation at still higher stagnation pressures.   This
statement particularly applies to helium containing mixtures,
where the addition of a Roots blower to our pumping system
will enable the source to operate with higher nozzle pres-
sures (or with a larger nozzle orifice, which would also
increase the terminal Mach number of the beam).   Figure 12
shows that the beam Mach number decreases as a function of
RF power level.   This is not surprising since the number
density at the orifice decreases as $1/T$, where T is the
effective plasma temperature at the orifice.   It is never-
theless important to understand the actual *extent* of Mach

number degradation with increasing RF power since future operation of the beam source at higher stagnation pressures may require the use of higher power levels.

D.   Plasma Temperature

The temperature of the gas at the nozzle orifice has been determined for a variety of source operating conditions with two different techniques. The first of these techniques depends on the flux change which occurs when the gas temperature at the orifice is varied. The flux emanating from the orifice at constant stagnation pressure depends on the gas temperature in the following way:

$$\mathrm{F}(T) \quad \propto \quad n(T) \cdot v(T) \quad \propto \quad 1/\sqrt{T} \tag{6}$$

where the particle number density, $n(T)$, varies as $1/T$ and the velocity of the particles emanating from the nozzle, $v(T)$, goes as $\sqrt{T}$. An approximate determination of the plasma temperature can therefore be made by measuring the pressure in the source with the discharge turned on and off:

$$\frac{P_1}{P_2} \quad \propto \quad \frac{\phi_1}{\phi_2} \quad \propto \quad \sqrt{\frac{T_2}{T_1}} \tag{7}$$

A Bayard-Alpert ionization gauge was used for making these
pressure measurements, and the gas temperature with the
discharge off was assumed to be 300K. Using equation (7)
the plasma temperature for high pressure oxygen-helium
mixtures is repeatedly found to range from 800-900K for
130 watt discharges, 850-1100K for 165 watts, and from
1150-1300K for 195 watts. Only a slight pressure dependence
is observed, with the temperature tending to decrease
slowly with increasing pressure. Oxygen-argon mixtures
are found to be considerably hotter: 1300-1500K for 130
watts, 1600-1750K for 165 watts, and 1750-2050K for 195
watt discharges at high pressures. The oxygen-argon dis-
charges also have much stronger pressure dependences than
the oxygen-helium discharges, with their temperatures
rising significantly as the stagnation pressure is lowered.
As a specific example of this a 5% O_2-Ar, 130 watt discharge
was found to increase in temperature from 1400K to 1750K
as the pressure was lowered from 250 torr to 100 torr. For
this reason extreme caution should be taken when igniting
(at low pressures) high power argon discharges. Immediately
after igniting high power argon discharges the pressure
should be quickly raised to at least 100 torr in order to
avoid melting of the quartz orifice. The above temperature
measurements are of course only approximate, but are very
useful for day to day plasma characterization. Also note

that the electron temperatures in the plasma are much hotter
than the above translational temperatures, with electron
temperatures on the order of 10,000K or higher being achieved
in the discharge.

More accurate plasma temperature determinations can
be made by monitoring the mole fractions and velocity
distributions of the three species (O, O_2, and either
helium or argon) which are present in the beam. These
temperature determinations may be carried out by assuming
the overall energy balance.[27,28]

$$(\Sigma X_i C_{p_i})T_o = \Sigma X_i C_{p_i} T_{bi} + \frac{1}{2} \Sigma X_i m_i v_i^2 \qquad (8)$$

where X_i is the mole fraction, C_{p_i} the heat capacity, v_i
the terminal velocity, m_i the mass, and T_{bi} the terminal
temperature of each component of the beam, and T_o is the
temperature of the gas at the orifice. The assumptions
which must be made in order to calculate T_o from equation
(8) have been thoroughly reviewed in Reference 8. The
mole fractions of each component have been calculated
using the molecular dissociation data which was discussed
earlier, taken in conjunction with the known composition
of the gas mixture under investigation. Figure 13 shows

the RF power dependence of gas temperature. at constant
pressure, for three different gas mixtures. Once again
we see that the argon containing mixtures generate signifi-
cantly hotter plasmas and exhibit stronger power dependences
than the helium containing ones. The data used in con-
structing these curves were intentionally taken at relatively
high operating pressures in order to ensure the validity
of equation (8). The pressure dependence of gas temperature,
at constant RF power, has also been studied for several gas
mixtures under a wide variety of operating conditions.
These studies again indicate that the gas temperature
decreases with increasing pressure. For example, helium
containing gas mixtures typically decreased 200 degrees,
from about 1000K to 800K, for a pressure change from 100 to
200 torr. Argon containing mixtures also exhibit this
temperature decrease with increasing gas pressure. We also
find that the assumptions which enable equation (8) to be
used for calculating gas temperature appear to break down
at low pressures for argon containing mixtures due to the
poor quality of these expansions. This statement especially
applies to high power, low pressure discharges which contain
argon.

In a final attempt to gauge the true gas temperature at the orifice we have also measured the velocity distribution of a pure helium beam which was produced from a 200 torr, 175 watt discharge. Its peak velocity was found to be 2.83×10^5 cm/sec. For an ideal nozzle expansion of a rare gas, where $v = \sqrt{5kT_o/m}$, this velocity corresponds to a gas temperature of 770K. This temperature can be considered to be in fairly good agreement with the temperatures determined above when we take into consideration the difference in gas composition which exists between this discharge and those previously discussed.

In concluding this section on plasma temperature characterization it should be mentioned that we have encountered some plasmas which were not suitable for generating atomic species. In particular, we have been unable to generate "hot" discharges for gas mixtures predominantly composed of helium when small nozzle orifices of ≤ 0.127 mm diameter were tested. These "cool" discharges would typically have temperatures on the order of only 400K for power levels up to 200 watts. These "cool" discharges are fortunately of little practical concern since orifices of ≥ 0.180 mm diameter are always used for running helium containing mixtures. The rate of gas flow out of the orifice is therefore seen to

influence the mode stability of discharges containing helium, with faster flow rates stabilizing the hotter mode (~1000K) relative to the cooler mode (~400K). Argon containing plasmas also have various discharge modes, with the two most important modes being the desired "hot mode" (~1750K) and the destructive "streamer" or "pencil" mode which can occur for operation at pressures in excess of 400-500 torr at high power levels. This latter mode is extremely hot and can cause rapid enlargement of the orifice. The inner diameter of the plasma containing quartz tube can influence the probability of this "hot mode" to "streamer mode" transition. The inner tube dimensions given earlier in this paper were chosen as a compromise between maximizing power coupling to the discharge and minimizing the probability of streamer formation at high pressures.

E. Beam Intensity

Absolute beam flux measurements have been carried out in a differentially pumped beam source test facility in which a Bayard-Alpert gauge having a 52 mm sidearm extension was used as the particle detector. For these measurements the long sidearm of the detector gauge was pointed directly into the beam and was terminated with a small 1.58 mm conical aperature. The pressure rise, ΔP, which is registered

by the gauge when the beam is turned on can be used for
calculating the absolute intensity of the beam when the
distance between the source skimmer and the detector
entrance aperature, d, is accurately known. This inten-
sity determination is possible since the pressure rise,
ΔP, reflects the new rate equilibrium which is established
between molecules entering the detector and those effusing
from it. The rate at which molecules enter the detector
can therefore be found by calculating the rate at which
molecules effuse out of the detector. This effusion rate
can be expressed as: $\phi = \frac{1}{4} n_o v_o A$, where $n_o = \Delta P/RT$,
$v_o = \left(\frac{8kT}{\pi m}\right)^{\frac{1}{2}}$, A is the area of the detector entrance aperature,
and T is assumed to be 300K. The long sidearm extension
was added to the ionization gauge to ensure the validity of
this last assumption. The absolute intensity of the beam
in terms of solid angle units can be obtained by dividing
ϕ by ΔΩ, the solid angle subtended by the detector aperature,
where $\Delta\Omega = A/d^2$. Examination of the above relationships
reveals that the actual area of the detector aperature does
not influence the outcome of the beam intensity determina-
tion as it cancels out in the final step of the calculation.
The detector-skimmer distance, d, was fixed at 86.54 mm for
these studies. Pure argon discharges which were operated
at power levels between 165 and 195 watts at stagnation

pressures up to 350 torr were found to have beam fluxes
of 3.6 x 10^{18} atoms sr^{-1} sec^{-1}. The atomic oxygen mole
fraction present in the terminal beam of 10% O_2-Ar
discharges, run under the same power and pressure
settings as above, is known to be 0.15 from molecular
dissociation experiments. By combining the above data
the absolute oxygen atom flux produced by discharging
oxygen-argon mixtures is found to be ca. 5 x 10^{17}
atoms sr^{-1} sec^{-1}. Pure helium discharges which were
run at 200 torr with power levels again between 165
and 195 watts produced beam fluxes of 5.5 x 10^{19} atoms
sr^{-1} sec^{-1}. Combining this figure with the measured
atomic oxygen mole fraction for 10% O_2-He discharges,
X = 0.10, leads to an absolute atomic oxygen flux of ca.
5 x 10^{18} atoms sr^{-1} sec^{-1} for oxygen-helium discharges.
The pure rare gas beam intensities produced by this source,
as described above, are comparable in magnitude to the
intensities which have been reported in the literature
for other nozzle beam sources.[29,30] The ionization gauge
readings which were used for these and subsequent beam
intensity calculations were corrected for the differences
in gauge sensitivity which exist for the various gases
under study. The gauge readings were actually divided
by 1.19, 0.15, and 0.85 in order to find the true pressure

changes due to Ar, He, and O_2, respectively.[31] These
represent the correct gauge sensitivity conversion factors
as the detector gauge was calibrated for N_2.

The pressure rises due to oxygen-rare gas beams were
also measured in order to perform an approximate check
on the atomic oxygen flux estimates described above. Pre-
dictions for the seeded beam pressure rises were based on
the pure rare gas data, and were calculated in the follow-
ing way: $\Delta P_{mix}(\text{predicted}) = (X_{RG} + X_{O_2}(\frac{0.85}{S}))\Delta P_{RG}$, where
X_{RG} and X_{O_2} represent the rare gas and oxygen concentrations
of the gas mixture, ΔP_{RG} is the pressure rise registered
by the gauge for a pure rare gas beam run under the same
stagnation pressure and RF power settings, ΔP_{mix} is the
predicted gauge pressure rise due to the seeded beam, and
S is the gauge sensitivity conversion factor for either
helium or argon. The measured gauge pressure increases
for oxygen-argon discharges agreed well with the predicted
gauge deflections, falling consistently within 10% of
ΔP_{mix}. However, the measured pressure rises for oxygen-
helium beams were usually 20% higher than the predicted
gauge deflection. This discrepancy can be explained if
the mole fraction of oxygen (O and O_2) along the beam
axis is larger in the terminal beam than in the initial
gas mixture. This explanation is supported by the fact

that the heavier particles of a seeded gas mixture are preferentially focused on the beam centerline during hydrodynamic nozzle expansion,[32] and are attenuated less than lighter particles in the region between the nozzle orifice and the skimmer. In summary, we therefore find the atomic oxygen flux to be about 5×10^{17} atoms sr^{-1} sec^{-1} for oxygen seeded in argon beams and $\geq 5 \times 10^{18}$ atoms sr^{-1} sec^{-1} for oxygen seeded in helium beams. For these determinations a $40°$ inner-$60°$ outer cone angle, 0.82 mm diameter boron nitride skimmer was fixed at a nozzle-skimmer distance of 5.08 mm, a second collimating skimmer of 1.04 mm diameter was placed 31.78 mm from the orifice, and a flat slot of variable dimensions was placed 52.76 mm from the orifice in the wall which separated the differential and detector sections of the apparatus. The total gas flow emanating from the nozzle is typically 0.75 torr-l/sec for 200 torr, 165-195 watt oxygen-helium dis- charges (0.191 mm diameter orifice) and 0.25 torr-l/sec for 350 torr, 165-195 watt oxygen-argon discharges (0.076 mm diameter orifice).

The ability of this beam source to produce intense atomic oxygen beams at high pressures, without suffering significant intensity loss due to atomic recombination, is one of its most novel and important operating

characteristics. This behavior is clearly demonstrated in Fig. 14 where the atomic oxygen number density, as measured with a quadrupole mass spectrometer, is plotted as a function of increasing stagnation pressure for four gas mixture-RF power level combinations. In Fig. 14a the relative $m/e = 16$ number density is seen to rise linearly with increasing stagnation pressure over the entire pressure regimes which were explored for two argon containing gas mixtures: up to 300 torr for a 5% O_2-Ar, 165 watt discharge and 350 torr for a 10% O_2-Ar, 195 watt discharge. The 10% O_2-He, 165 watt number density curve shown in Fig. 14b behaves in a similar manner, up to a maximum pressure of 200 torr, as those described above. However, the 5% O_2-He, 130 watt curve shown in this figure turns over at pressures higher than 200 torr. This indicates that power levels $\geq$ 165 watts should always be used for running oxygen-helium discharges above 200 torr total pressure. The $m/e = 16$ curves shown in Fig. 14 have all been corrected for the slight contributions arising from dissociative ionization of the molecular oxygen which is present in the beam. The high pressure segments of these curves are also representative of the relative atomic oxygen *fluxes* produced by this source, as a function of increasing pressure, due to the weak dependence beam velocity has on gas pressure at high stagnation pressure.

F. $O(^1D_2)$ Production

When dilute oxygen-helium gas mixtures are discharged in this beam source a mixture of atomic oxygen quantum states including ground state $O(^3P_J)$ and excited state $O(^1D_2)$ atoms is present in the terminal beam. When helium is used as the carrier gas the $O(^1D_2)$ flux has in fact proven to be of sufficient magnitude to permit differential reactive scattering experiments to be carried out. This represents a very significant development in the realm of molecular beam technology as prior to this no other $O(^1D_2)$ beam source has been reported in the literature.

$O(^1D_2)$ production was experimentally confirmed in our universal crossed molecular beam apparatus by observing the production of OH from the reaction

$$O(^1D_2) + H_2 \longrightarrow OH + H \qquad \Delta H = -43.5 \text{ kcal/mole} \qquad (9)$$

For this study a supersonic hydrogen beam (peak velocity = 2.66×10^5 cm/sec, Mach number = 21) was collided at $90°$ with an oxygen seeded in helium beam (peak atomic oxygen velocity = 2.38×10^5 cm/sec, Mach number = 9) at a relative collision energy of 2.7 kcal/mol . The oxygen beam was produced by discharging a 200 torr, 5% O_2-He gas mixture

with 200 watts of RF power. Under these experimental
conditions the OH could not have been produced by the
ground state reaction

$$O(^3P_J) + H_2 \longrightarrow OH + H \qquad \Delta H = 1.9 \text{ kcal/mole} \qquad (10)$$

due to the large 8.9 kcal/mole activation energy[33] which
is associated with this process. Further support of the
Reaction (9) process comes from the angular and velocity
distributions of the OH reaction product. The OH LAB angular
distribution shown in Fig. 15 extends as far as the OH(v=0)
Center-of-Mass velocity circle permits based upon a reaction
exoergicity of 43.5 kcal/mole, while the OH velocity distri-
butions obtained with cross correlation time-of-flight
techniques[34,35] fall off with velocities indicative of
this exoergicity. These experimental distributions also
indicate that the concentration of $O(^1S_0)$ atoms in the
terminal beam must be extremely low as no OH product was
observed at the high energies characteristic of the process

$$O(^1S_0) + H_2 \longrightarrow OH + H \qquad \Delta H = -94.7 \text{ kcal/mole} \qquad (11)$$

When 10% O_2-He gas mixtures were discharged rather than

5% O_2-He mixtures a 30% decrease in OH signal was observed relative to the 3000 counts/sec counting rate of the more dilute mixture. This indicates that the number of collisions occurring between $O(^1D_2)$ atoms and other oxygen species should be minimized during the expansion if extensive quenching of the $O(^1D_2)$ is to be avoided. When dilute oxygen-argon gas mixtures were tested no OH product was detected, indicating that, within the accuracy of the determination, oxygen seeded in argon beams contain no $O(^1D_2)$. This is fortunate as it enables $O(^3P_J)$ reactions to be studied in an environment free of $O(^1D_2)$ contamination when argon is used as the beam carrier gas.

The presence of $O(^1D_2)$ in beams having helium as the carrier gas can be attributed to the extremely small quenching rate constant of the process

$$O(^1D_2) + He(^1S_0) \longrightarrow O(^3P_J) + He(^1S_0)$$

$$\Delta H = -45.4 \text{ kcal/mole} \tag{12}$$
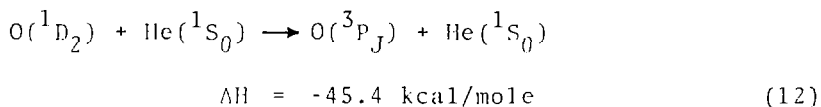
which has been experimentally found to be: $k^Q_{O-He} < 10^{-16}$ cm^3 molecule^{-1} sec^{-1}.[36] This value can be compared to the "gas kinetic" rate constant in order to crudely estimate the number of collisions needed for quenching to occur:

$k_{O-He}^{GK} = 8 \times 10^{-10}$ cm^3 molecule^{-1} sec^{-1}. This gas kinetic rate constant was approximated by $k^{GK} = (\pi r_m^2)(\frac{8kT}{\pi\mu})^{1/2}$, where r_m is the experimentally determined Lennard-Jones (12,6) parameter for $O(^3P_J)$-He collisions,[37] T is the plasma temperature, taken as 1000K, and μ is the reduced mass of the collision partners. The above indicates that, on the average, about 10^6 $O(^1D_2)$-He collisions must occur before quenching takes place. Since only about 10^2 collisions occur during the expansion[38] it is not sur- prising that some $O(^1D_2)$ atoms are present in the terminal beam. In fact, most $O(^1D_2)$ quenching probably occurs during collisions between $O(^1D_2)$ and other oxygen species which are present in the beam. In contrast to this, the experimentally determined rate constant for $O(^1D_2)$ quenching by Ar, $k_{O-Ar}^Q = 3 \times 10^{-13}$ cm^3 molecule^{-1} sec^{-1},[36] is only about three orders of magnitude smaller than the O-Ar "gas kinetic" rate constant, $k_{O-Ar}^{GK} \approx 6 \times 10^{-10}$ cm^3 molecule^{-1} sec^{-1}, which was calculated assuming a plasma temperature of 1500K and using the r_m value for $O(^3P_J)$-Ar given by Reference 37. The $O(^1D_2)$-Ar collisions therefore deactivate a significant fraction of the $O(^1D_2)$ atoms during expansion, with the remaining $O(^1D_2)$ atoms being deactivated by collision with the other atomic and molecular oxygen species which are present in the beam ($k_{O-O_2}^Q = 3.7 \times 10^{-11}$ cm^3 molecule^{-1} sec^{-1}).[36] An analysis of the collision dynamics

for Reaction (9) is currently being prepared for publication, and will be presented elsewhere in the literature.

The pressure and power dependence of $O(^1D_2)$ production has been examined for a 5% O_2-He gas mixture in our crossed beam apparatus. This was accomplished by monitoring, at the peak of the broad product angular distribution, the OH signal intensity coming from Reaction (9) as a function of beam source pressure and RF power level. Since the oxygen and hydrogen beam velocities are nearly equal the OH count rate is indicative of the $O(^1D_2)$ particle flux. (Whereas if the hydrogen beam were much faster than the oxygen beam the OH count rate would be indicative of the $O(^1D_2)$ number density at the collision center.) The curved shape of the intensity versus pressure data shown in Fig. 16a indicates that some $O(^1D_2)$ quenching does occur at higher pressures, but not to the extent which would require operating the sources at pressures below 250 torr. The intensity versus RF power curves shown in Fig. 16b clearly indicate that higher source powers (and hence plasma temperatures) significantly increase the flux of $O(^1D_2)$ emanating from the nozzle. In the near future gas mixtures composed of less than 5 percent oxygen will be characterized in order to determine the optimum oxygen-helium mixture for maximizing $O(^1D_2)$ production.

DISCUSSION

The high pressure, supersonic, radio frequency dis-
charge beam source which has been described in the pre-
ceeding sections of this paper offers several improvements
in the important operating characteristics of beam trans-
lational energy, beam intensity, velocity distribution
width, and beam composition when compared to either thermal
or low pressure discharge effusive sources. For example,
the atomic oxygen translational energies which have been
accessed in our laboratory span the range from 0.1-0.5 eV,
with future extension of this range up to 0.7 eV being
possible for operation with dilute oxygen-helium mixtures.
These energies are considerably higher than those accessible
with effusive sources constructed from either thoria (ThO_2)[39]
or iridium.[40] Also, the atomic oxygen intensity produced
by an effusive thermal oven, operating with Knudsen number =
1, would be ca. 4×10^{16} atoms sr^{-1} sec^{-1}.[41] This intensity
was calculated using an O_2 pressure of 1 torr, a calculated
equilibrium constant of $K_p = 1.2 \times 10^{-2}$ torr for the process
$O_2 \rightleftharpoons 2O$ at 2500K, and assuming that the source orifice
was 2 mm high. The fluxes available from low pressure dis-
charge sources are comparable to this, with atomic oxygen
fluxes of ca. 3×10^{16} atoms sr^{-1} sec^{-1} being realized for
operation under effusive flow conditions (with 10% molecular

dissociation, a temperature of 350K,[42] Knudsen number = 1, and a slit height of 2 mm). The above atomic oxygen intensities are much lower than the measured intensities produced by our seeded nozzle source: ca. 5×10^{17} atoms sr^{-1} sec^{-1} for oxygen-argon mixtures and $\simeq 5 \times 10^{18}$ atoms sr^{-1} sec^{-1} for oxygen-helium mixtures. Also note that the Maxwellian velocity distributions typical of effusive sources are quite often too broad for carrying out well defined collision experiments, necessitating the use of mechanical velocity selectors which further reduce their intensity by at least an order of magnitude. It is there-fore evident that the nozzle source described here is capable of producing atomic oxygen fluxes which are at least 1-3 orders of magnitude higher than those possible with conventional effusive sources, with the actual inten-sity gain depending upon the peak velocity and velocity widths which are used for this comparison. The high atomic oxygen fluxes produced by this source should permit extremely well defined collision experiments to be carried out in which the supersonic beam source would be coupled with either a high resolution mechanical velocity selector or with a magnetic sublevel quantum state selector in order to further define the atomic beam.

The ability of this source to generate seeded beams
having high molecular dissociation at pressures up to
several hundred torr total pressure is undoubtedly due
to plasma localization at the nozzle tip and to the
highly efficient power coupling which has been achieved
between the RF tank circuit and the plasma. The use of
radio frequency rather than microwave power simplified the
above as radio frequency generated plasmas can be easily
drawn out of the region enclosed by the coupling coil,
while microwave generated plasmas tend to strongly localize
in the region surrounded by the coupling cavity. The
facile frequency variability and impedance matching of the
RF circuitry described earlier also simplifies operation
at high pressures. The water cooled nozzle, which ensures
extremely stable and reproducible day to day operation of
the source, would have to be replaced with a more cumber-
some and less efficient oil-cooled design if microwave
radiation were used. The ability of this source to generate
terminal beams containing $O(^1D_2)$ atoms is at this time
unique, and would not have been possible if the discharge
were removed from the region immediately behind the orifice.

The atomic oxygen is probably generated in the dis-
charge by a variety of kinetic processes. Thompson[43] has
shown, for low pressure discharges, that dissociation can

be directly induced by electron-O_2 collisions via the
Schumann-Runge continuum $O_2(^3\Sigma_g^-) + [O_2(^3\Sigma_u^-)] \rightarrow O(^3P_J) +$
$O(^1D_2)$ for collision energies ≥ 7.1 eV. Metastable argon
collisions could also lend to dissociation via this pro-
cess.[11] Metastable helium atoms, due to their high
energies, have the ability to Penning ionize molecular
oxygen. Ionization in this manner, followed by dissocia-
tive recombination between O_2^+ and an electron has been
proposed as the primary source of atomic oxygen in
oxygen-helium RF discharges.[8]

The generation of other atomic and electronically
excited species should also be possible with this source.
In our laboratory we have briefly tested dilute hydrogen-
helium mixtures (125 torr total pressure, 145 watts)
and have observed atomic hydrogen production. The genera-
tion of a supersonic molecular beam containing $O_2(^1\Delta_g)$
without the simultaneous presence of atomic oxygen in the
terminal beam should be possible. This could be accomplished
by pulling the discharge back, away from the nozzle tip, and
by introducing a small amount of mercury into the gas
mixture. The resulting mercuric oxide coating located
after the discharge zone would effectively remove the
atomic species present in the gas.[44] The feasibility of
generating atomic nitrogen beams with a high temperature

version of this source is currently being explored in our
laboratory.

REFERENCES

1. J. T. Herron and R. E. Huie, J. Phys. Chem. Ref. Data, 2, 467 (1973).

2. S. J. Arnold and H. Rojeska, Appl. Opt. 12, 169 (1973).

3. R. J. Madix and A. A. Susu, Surface Sci. 20, 377 (1970).

4. W. D. McGrath and J. J. McGarvey Planet. Space. Sci. 15, 427 (1967).

5. R. J. Cvetanović, Advan. Photochem. 1, 115 (1963).

6. J. B. Anderson, R. P. Andres, and J. B. Fenn, in Adv. Chem. Phys., Vol. 10, J. Ross, Ed. (John Wiley and Sons, New York, 1966), p.27.

7. N. Abauf, J. B. Anderson, R. P. Andres, J. B. Fenn, and D. G. H. Marsden, Science 155, 997 (1967).

8. D. R. Miller and D. F. Patch, Rev. Sci. Instrum. 40, 1566 (1969).

9. P. A. Gorry, C. V. Nowikow, and R. Grice, Chem. Phys. Lett. 49, 116 (1977).

10. AD-998 alumina: Coors Porcelain Company, Golden, Colorado, USA.

11. H. S. Johnston, Gas Phase Reaction Kinetics of Neutral Oxygen Species, Chemical Kinetics Information Center, Nat. Stand. Ref Data Sys., Nat. Bur. Stand. 20, (U.S. Government Printing Office, Washington, D.C., 1968), p.4.

12.   H. G. Wagner and J. Wolfrum, Angew. Chem. Internat. Edit. 10, 604 (1971).

13.   F. K. McTaggart, Plasma Chemistry in Electrical Discharges (Elsevier, Amsterdam, 1967), p.38.

14.   The Radio Amateur's Handbook, 46th ed., D. DeMaw, Ed. (ARRL, Newington, 1969), p.44.

15.   The Radio Amateur's Handbook, 46th ed., D. DeMaw, Ed. (ARRL, Newington, 1969), p.49.

16.   Radio Engineering Handbook, 5th ed., K. Henny, Ed. (McGraw-Hill, New York, 1959), Chap.18, p.23.

17.   Model MN-2000: R. L. Drake Company, Miamisburg, Ohio, U.S.A.

18.   Paddlewheel flowswitch: Perkin-Elmer Ultek, Inc., Palo Alto, California, U.S.A.

19.   Carborundum hot pressed boron nitride: Carborundum Co., Refractories and Electronics Division, Latrobe, Pennsylvania, U.S.A.

20.   Y. T. Lee, J. D. McDonald, P. R. LeBreton, and D. R. Herschbach, Rev. Sci. Instrum. 40, 1402 (1969).

21.   M. S. Child, Molecular Collision Theory (Academic, New York, 1974), p.3.

22.   W. L. Fite and R. T. Brackman, Phys. Rev. 113, 815 (1959).

23.   D. Rapp, P. Englander-Golden, and D. D. Broglia, J. Chem. Phys. 42, 4081 (1965).

24. J. B. Anderson and J. B. Fenn, Phys. Fluids, $\underline{8}$, 780 (1965).

25. J. J. Valentini, Ph.D. dissertation, University of California, Berkeley, California, 1976.

26. D. H. Levy, L. Wharton, and R. F. Smalley, in Chemical and Biochemical Applications of Lasers, C. R. Moore, Ed. (Academic, New York, 1977), Vol. 2, p.1.

27. D. R. Miller and R. P. Andres, in Sixth Rarefied Gas Dynamics, L. Trilling and H. Wachman, Eds. (Academic, New York, 1969), Vol. 2, p.1385.

28. D. R. Miller and R. P. Andres, J. Chem. Phys. $\underline{46}$, 3418 (1967).

29. J. G. Skofronik, Rev. Sci. Instrum. $\underline{38}$, 1628 (1967).

30. G. Scoles and F. Torello, "Production of Molecular Beams from Free Expanding Jets, Part 1", Report of the Gruppodi Strutture Della Materia del C.N.R., August 1967.

31. Scientific Foundations of Vacuum Techniques, S. Dushman and J. M. Lafferty, Eds. (John Wiley and Sons, New York, 1962), p.324.

32. J. B. Anderson, R. P. Andres, and J. B. Fenn, in Molecular Beams, J. Ross, Ed. (John Wiley and Sons, New York, 1966) p.312.

33. D. L. Baulch, D. D. Drysdale, D C. Horne, and A. C. Lloyd, Evaluated Kinetic Data for High Temperature Reactions (Butterworth, London, 1972), Vol. 1, p.49.

34. A. T. Hir chy and J. P. Aldridge, Rev. Sci. Instrum. 4., 581 (1971).

35. E. Sköld, Nucl. Instrum. Meth. 63, 114 (1968).

36. K. Schofield, J. Photochem. 9, 55 (1978).

37. A. Aquilanti, G. Liuti, F. Pirani, F. Vecchiocattivi, and G. G. Volpi, J. Chem. Phys. 65, 4751 (1976).

38. J. J. Valentini, private communication.

39. W. Espe, Materials of High Vacuum Technology Vol. 12 - Silicates, (Pergamon, Oxford, 1968) p.564.

40. P. L. Moore, P. N. Clough, and J. Geddes, Chem. Phys. Lett. 17, 608 (1972).

41. H. Pauly and J. P. Toennies, in Methods of Experimental Physics, B. Bederson and W. L. Fite, Eds. (Academic, New York, 1968), Vol. 7A, p.232.

42. D. St. A. G. Radlein, J. C. Whitehead, and R. Grice, Mol. Phys. 29, 1813 (1975).

43. J. B. Thompson, Proc. Roy. Soc. A. 262, 503 (1961).

44. A. M. Winer and K. D. Bayes, J. Phys. Chem. 70, 302 (1966).

FIGURE CAPTIONS

Fig. 1.   Sectioned view of the plasma beam source mounted
           in a differentially pumped chamber. A-Lucite
           insulating flange. B-Nozzle coolant return.
           C-Quartz nozzle gas inlet. D-Cajon ultra-torr
           fittings. E-Nozzle coolant inlet. F-RF power
           input from RG-213/U coaxial cable. G-Variable
           air capacitor. H-Coupling coil coolant outlet.
           I-Coupling coil coolant inlet. J-Ceramic feed-
           through for RF return and coil coolant. K-Ceramic
           feedthrough for RF input and coil coolant.
           L-Poly-Flo tubing sections. M-Stainless steel
           source chamber. N-Plates for 5000 V/cm ion
           deflecting field. O-1200 1/sec diffusion pump,
           differential region. P-4200 or 8000 1/sec
           diffusion pump, source region. Q-Epoxy resin
           mechanical support. R-Electrical ground wire.
           Not shown: Wire mesh RF shielding which covers
           the air capacitor/RF feedthrough assembly.

Fig. 2.   Sectioned view of the internal source components.
           A-Variable ground tap. B-Swagelock reducer.
           C-Water-cooled quartz nozzle. D-Coupling coil.
           E-Quartz support rod for water inlet/outlet
           assembly. F-Swagelock union joining copper and

Polyflow tubing. G Cajon VCO fitting. H Kovar-
pyrex section. I Graded seal, pyrex to vycor.
J Aluminum support block to electrical ground.
F boron nitride skimmer, 0.8Å mm. i An enlarge-
ment of nozzle tip; arrows indicate low conduc-
tivity water flow direction.

Fig. 3. Impedance matching circuitry.

Fig. 4. Block diagram of the plasma generating electronics.
The double solid lines indicate the equipment used
for high power operation, while the double dashed
lines indicate the bypassing necessary for pre-
liminary tune up of the source.

Fig. 5. a) Newton diagrams for O He and O_2 He elastic
scattering. b) Differential elastic scattering
cross sections for O He and O_2-He. The wide
angle falloff of the O He curve conclusively
demonstrates atomic oxygen production.

Fig. 6. Pressure dependence of O_2 dissociation:
○ 5% O_2 Ar, 165 watts; ● 5% O_2-Ar, 130 watts;
△ 10% O_2-Ar, 195 watts; □ 10% O_2-Ar, 140 watts;
■ 5% O_2-He, 130 watts; ▲ 10% O_2-He, 130 watts;
◇ 10% O_2-He, 165 watts; – – – performance data
for the source described in Reference 8.

Fig. 12.   P.I. power dependence of plasma temperature.

       ◯   ?, Ar, ?? torr;   ⬤   ?   Ar, ?? torr;

       ◻ ? ?, H?, ??? torr.

Fig. 13.   a. Atomic oxygen number density as a function of
pressure for argon containing mixtures.

       ◯ ? ? O?, Ar, 165 watts;   ⬤   ? ? Ar, ?? watts.
b. Atomic oxygen number density as a function of
pressure for helium containing mixtures.

       ◯ ? ? O?, He, 165 watts;   ⬤   ? ? H?, ?? watts.
These curves have all been corrected for the light
m/e = 16 contribution arising from dissociative
ionization of ma = 32 in the electron bombardment
ionizer.

Fig. 15.   Laboratory angular distribution of OH from the
reaction $O(^1D_2)$ + H_2 → OH + H at a relative
collision energy of 2.7 kcal/mole. The solid
line is a calculated fit to the experimental
data which employed a symmetrical center of mass
product distribution for the OH product. The
excellent fit between the calculated and experi-
mental data, taken in conjunction with with wide
angle falloff (~40°) of the distribution,
demonstrates the presence of $O(^1D_2)$ atomic oxygen
in the terminal beam.

Fig. 16. a. Relative ^1b_g intensity as a function of gas pressure for a 5:1 O_2:Ar, 100 watt discharge. b. Relative ^1b_g intensity as a function of R.F. power level for a 5:1 O_2:Ar mixture.

● 150 torr total pressure; ○ 300 torr total pressure. These curves indicate that the ^1b_g intensity can optimized by simultaneously operating the source at high power levels and set bars.

Fig. 1

F G H I J

E

D

C

B

A

K

L

10 cm

0.25 cm

Fig. 2

XBL782-2882

Coaxial cable
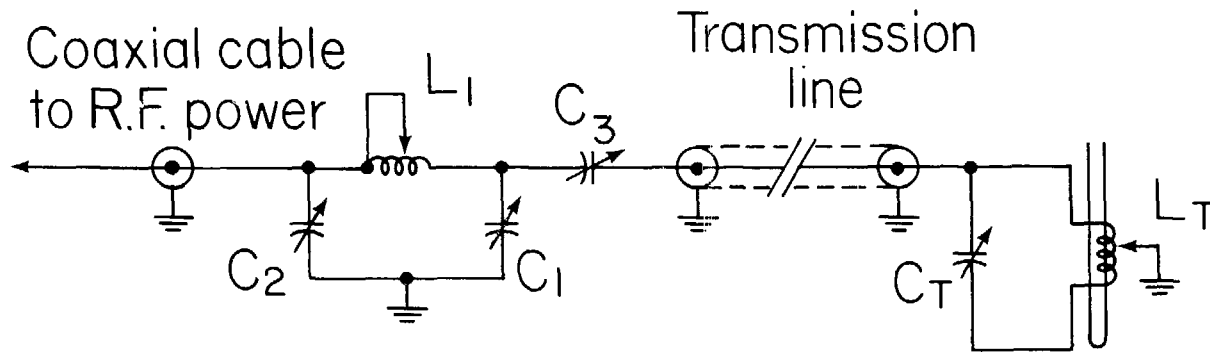to R.F. power

L_1

C_3

Transmission
line

C_2

C_1

C_T

L_T
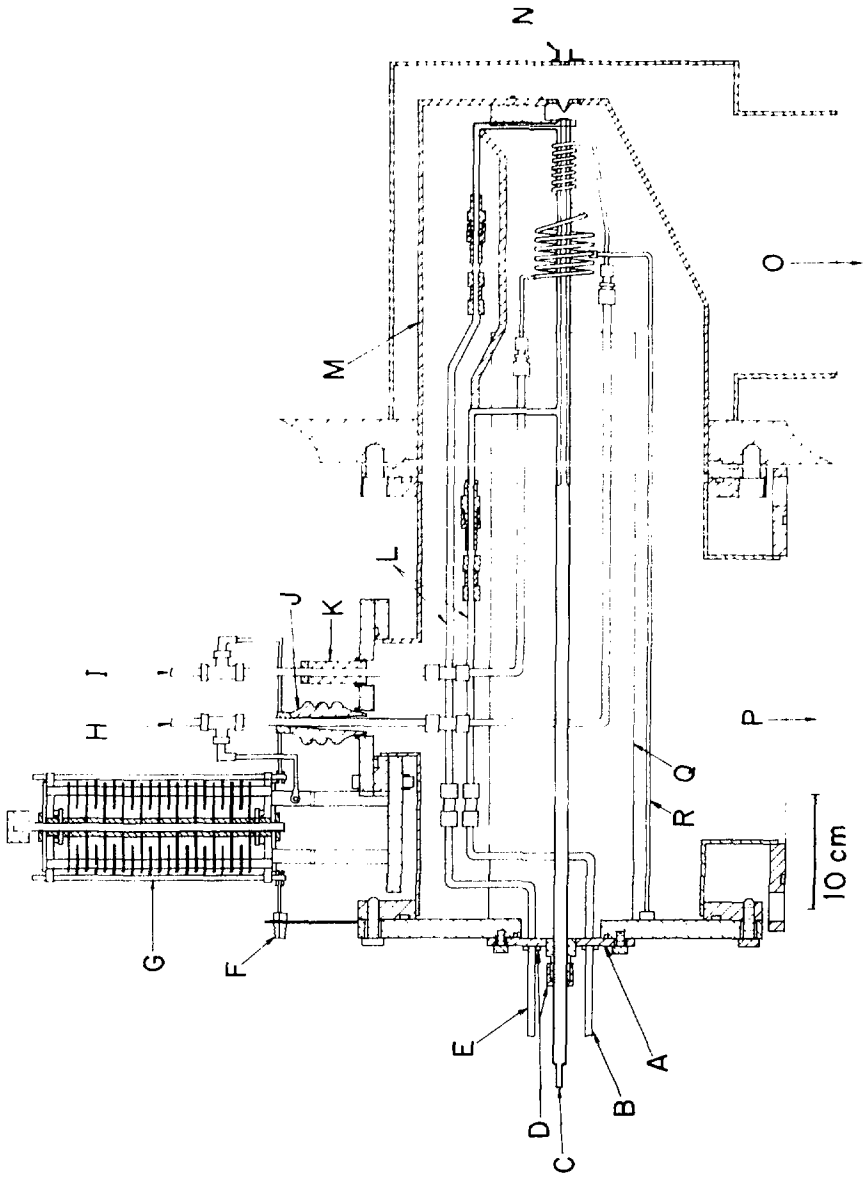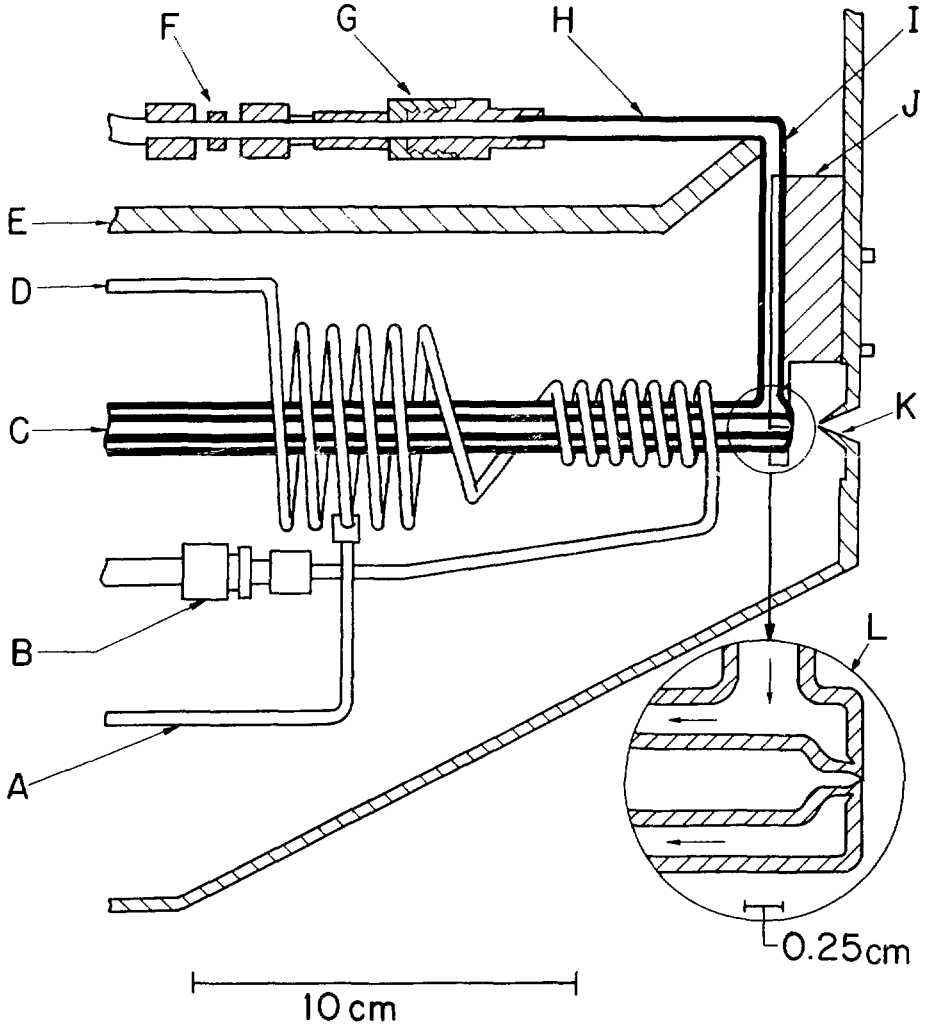
Fig. 3

XBL 797-2255

Fig. 4

XBL 797-2257
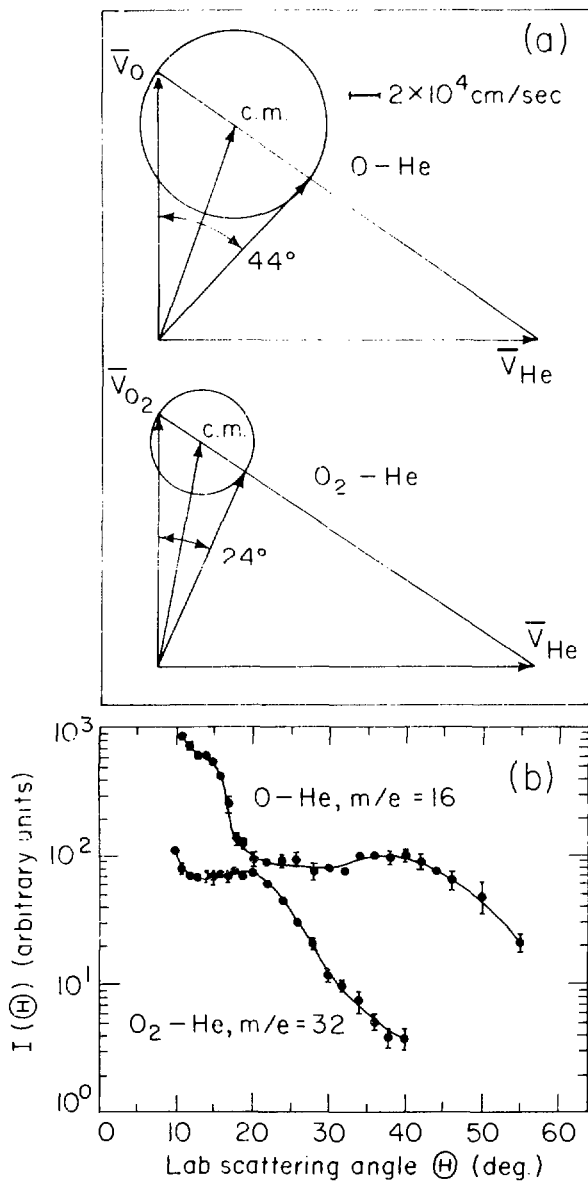
-77-

Fig. 5

XBL 797-2266

Fig. 6

XBL 797-2259

-79-

Fig. 7   XBL 797-2264

-80-

Fig. 8

XBL 797-2263

-81-
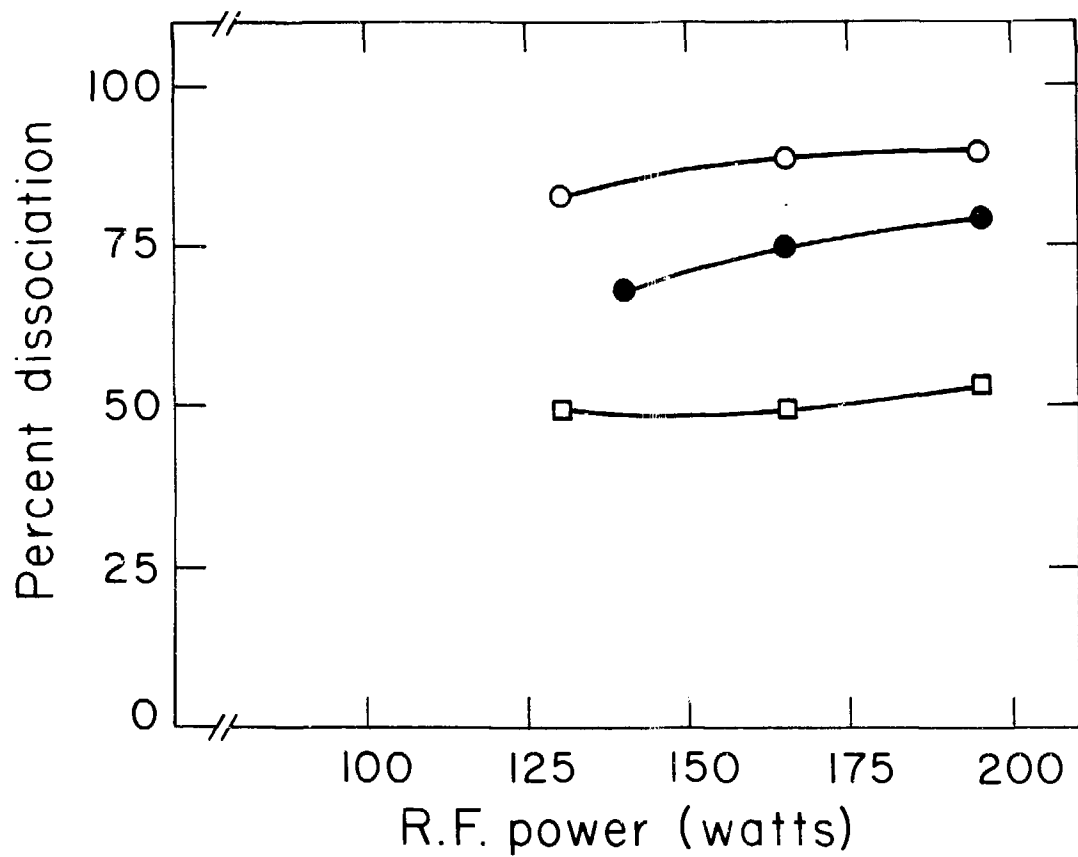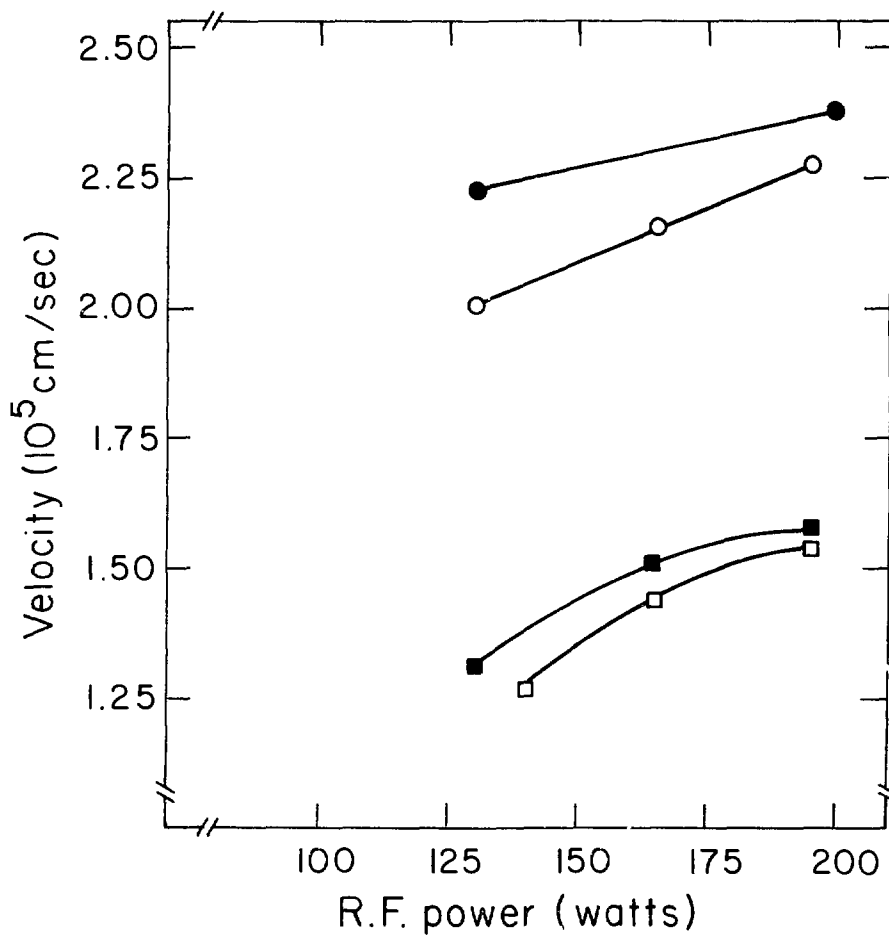
XBL 797-2262

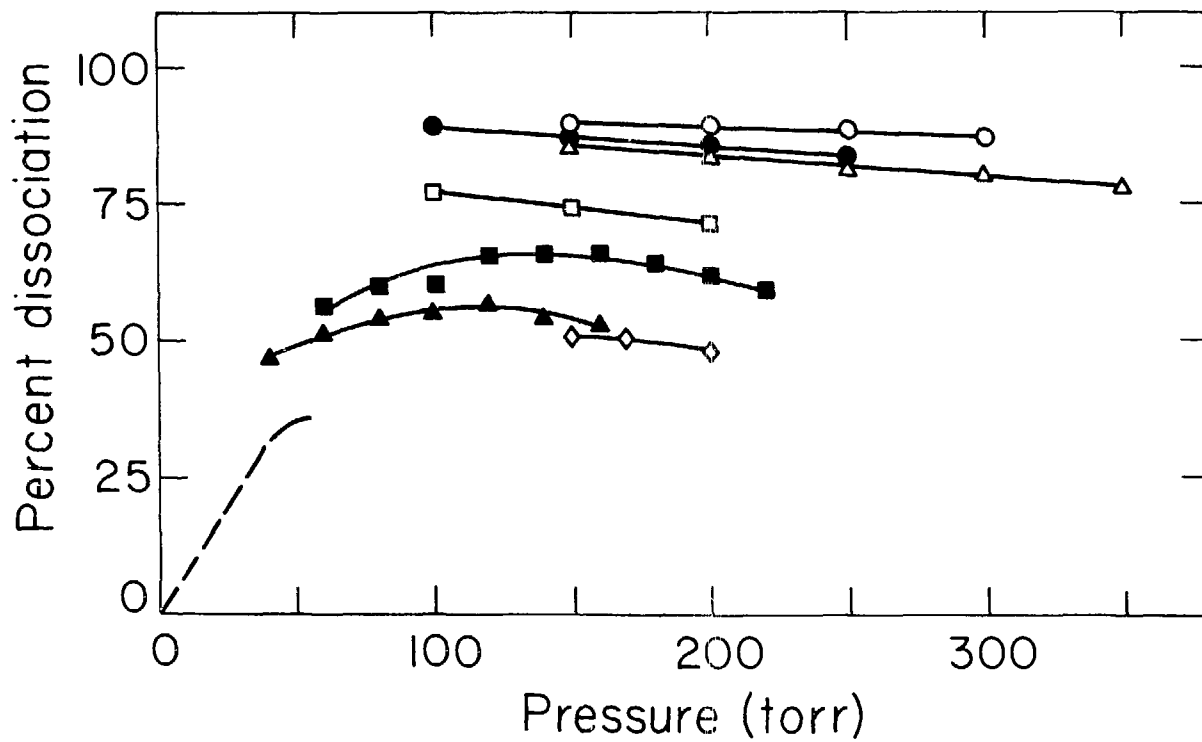Fig. 9
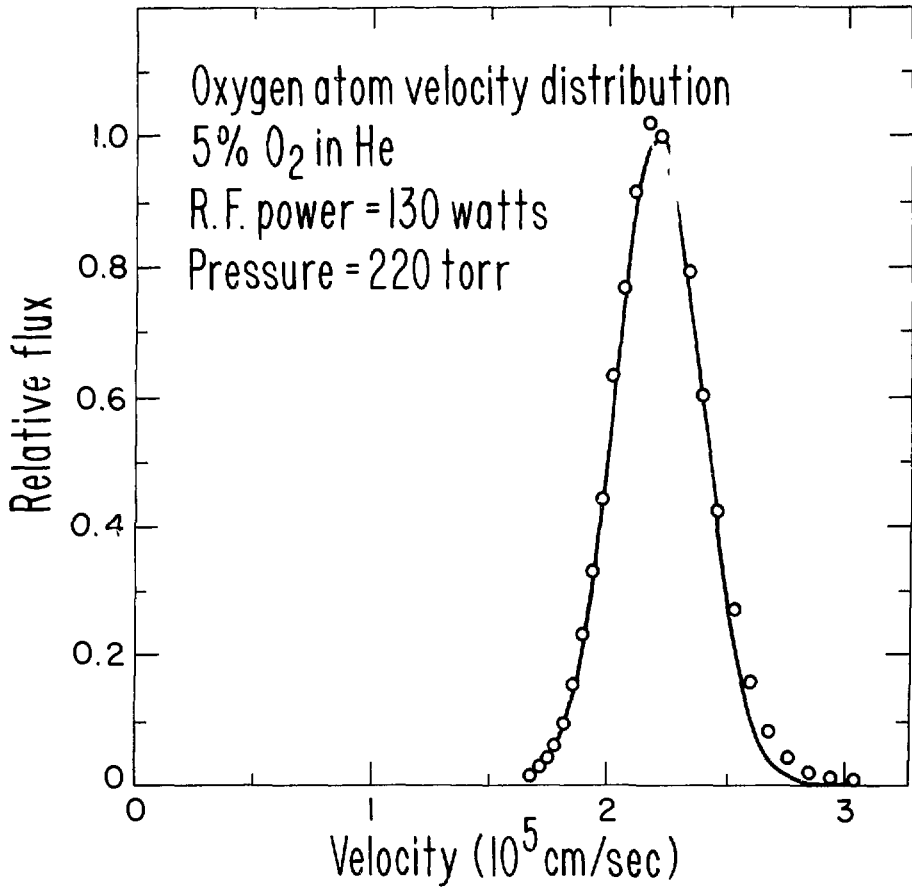
Fig. 10

Fig. 11

XBL 797-2258

Fig. 12
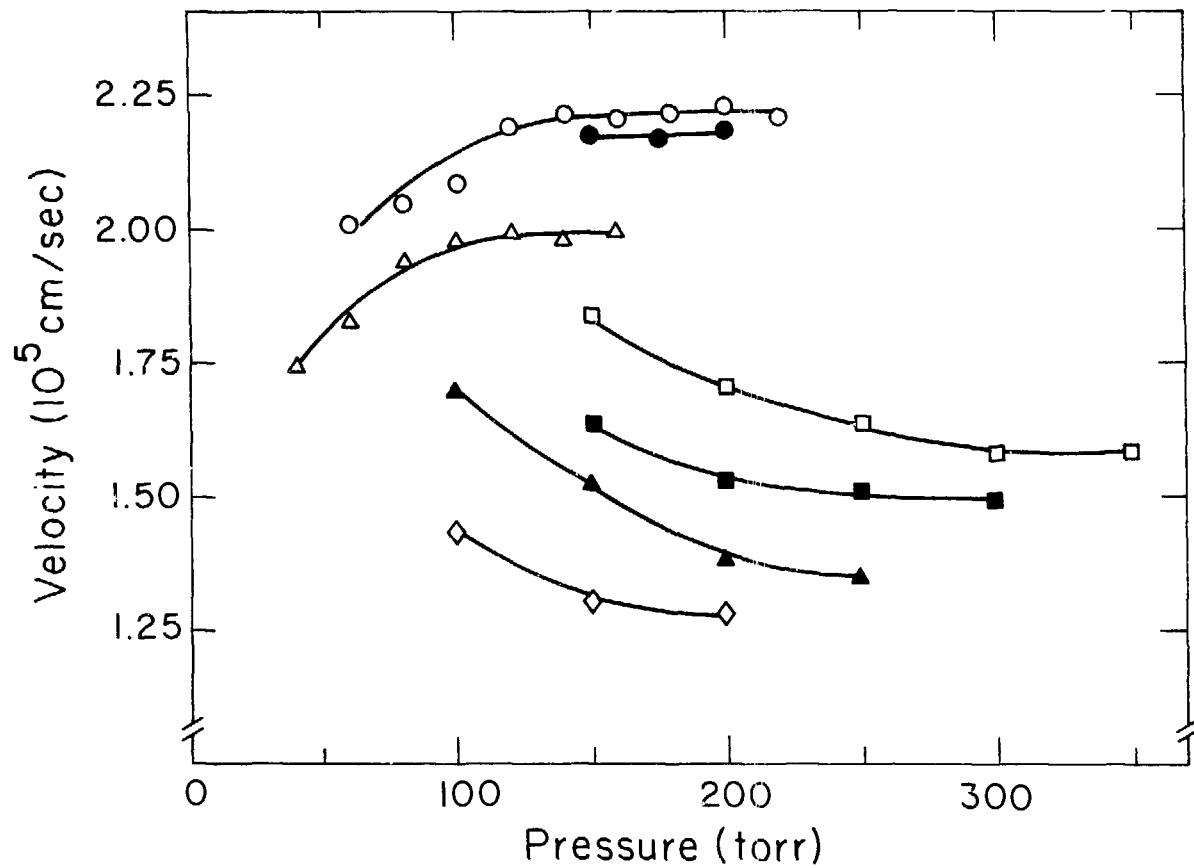
XBL 797-2261
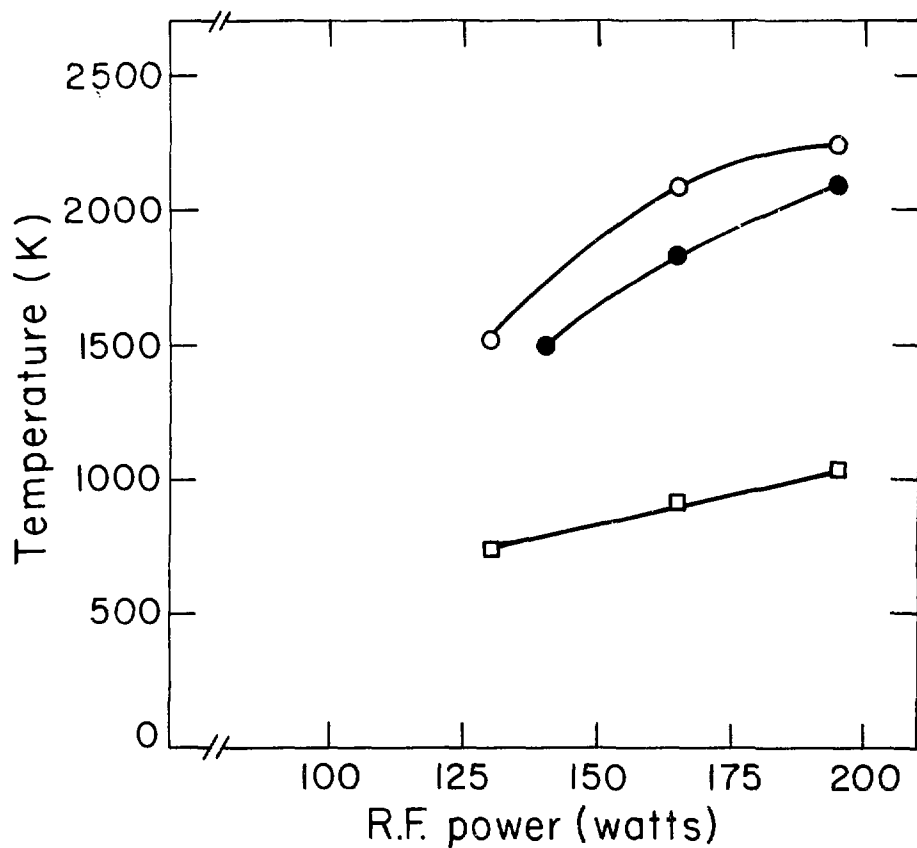
XBL 797-2260

Fig. 13
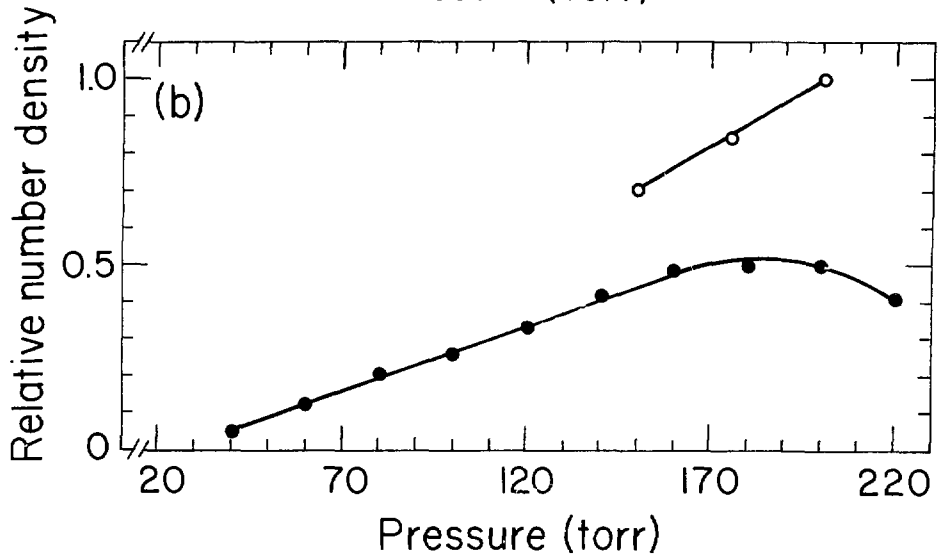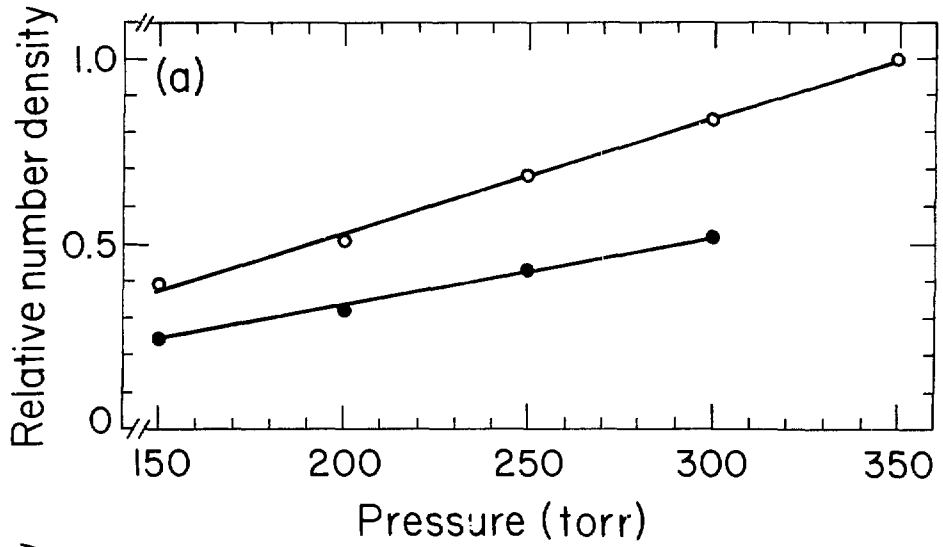
Fig. 14

XBL 797-2254

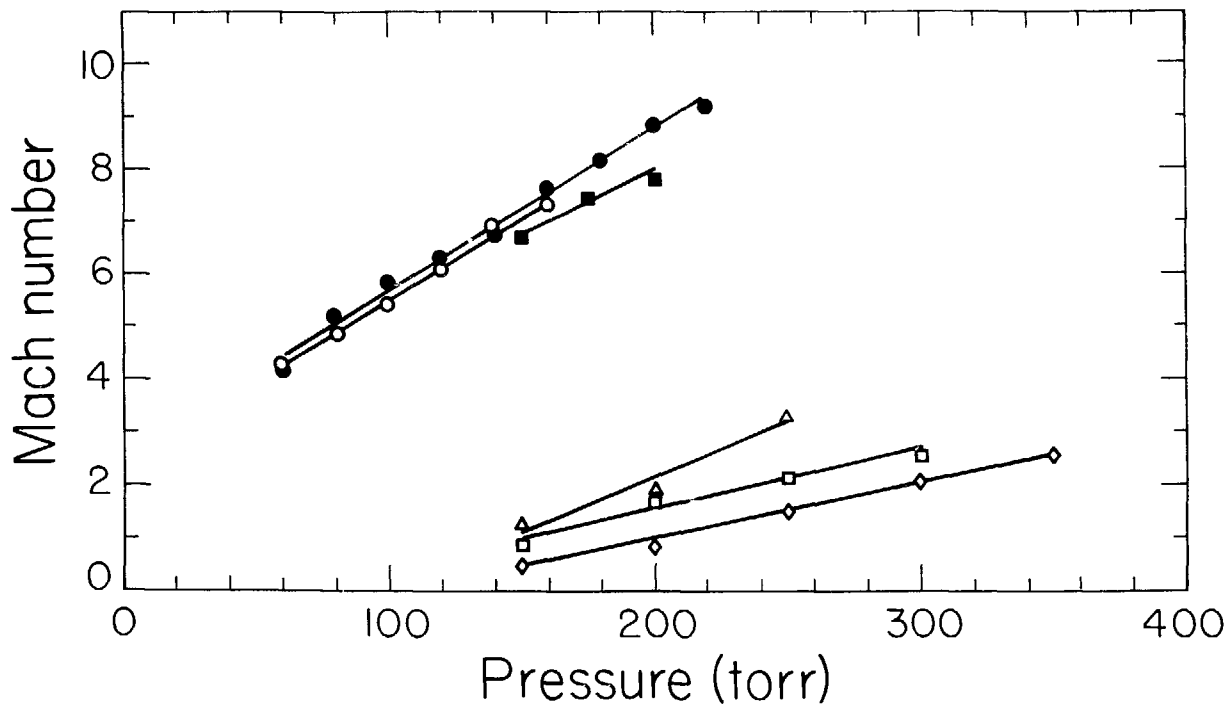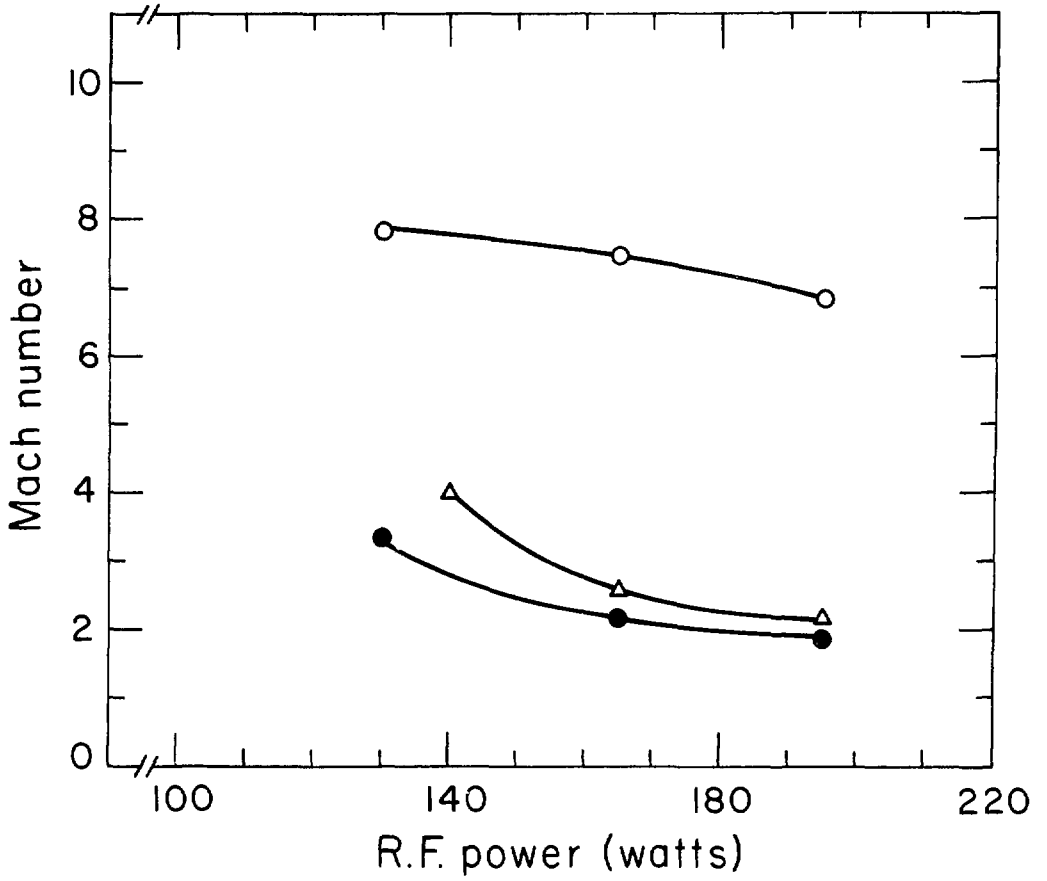Fig. 15   XBL 797-2253

(a)

Relative O(^{1}D$_2$) flux

Pressure (torr)

(b)

Relative O(^{1}D$_2$) flux

R.F. power (watts)
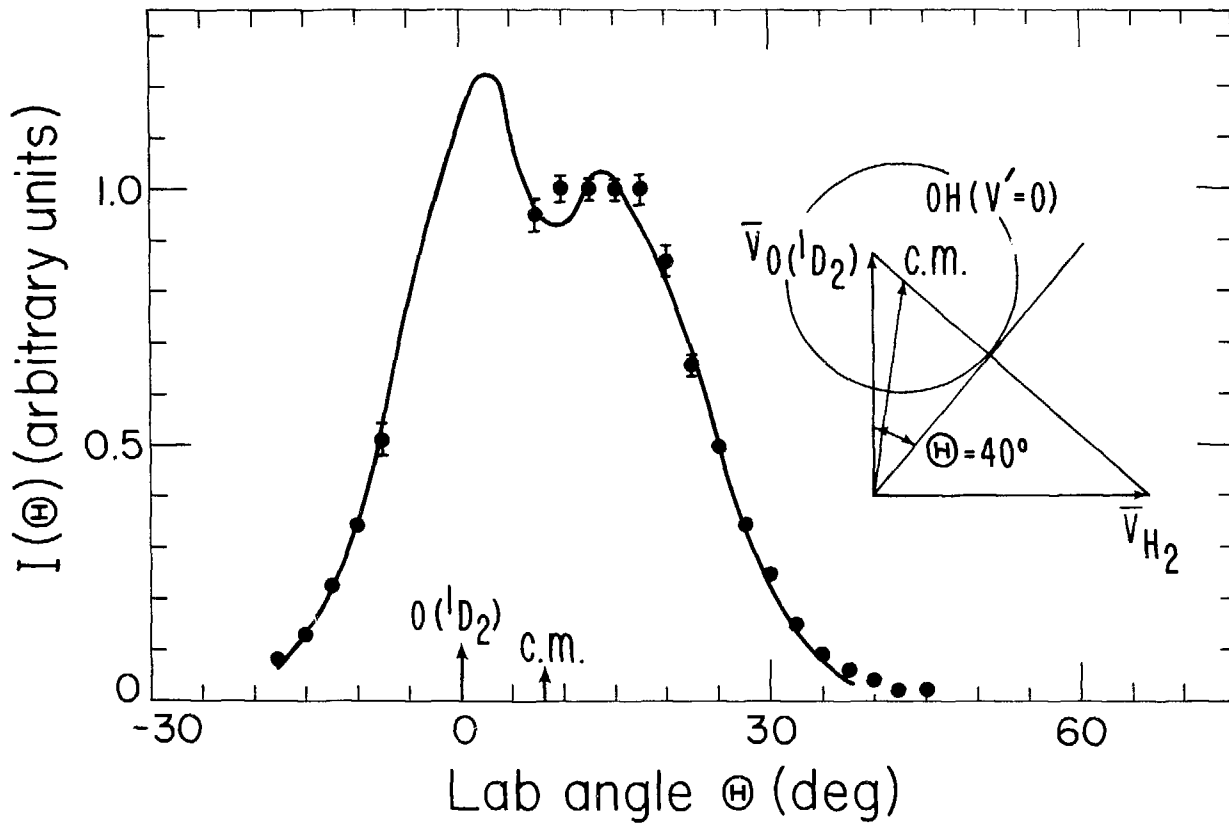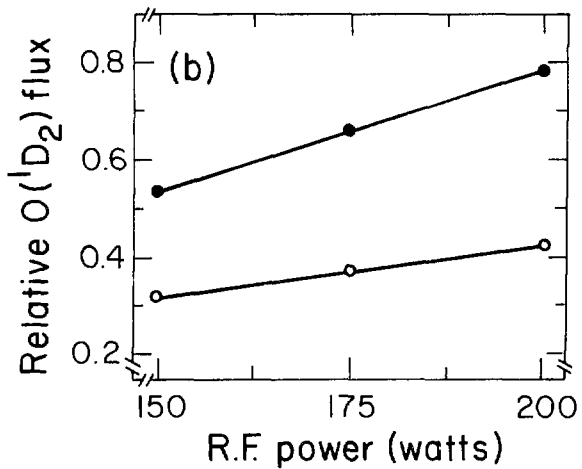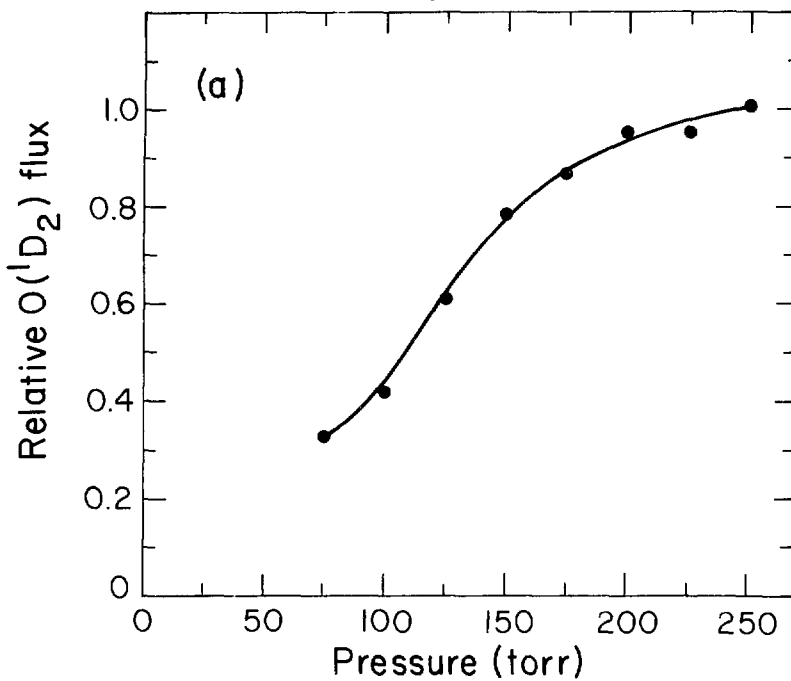
XBL 797-2256

Fig. 16

III. A CROSSED MOLECULAR BEAMS INVESTIGATION
OF THE REACTIONS $O(^3P)$ + ICl, CF_3I

INTRODUCTION

The reactions of ground state $O(^3P)$ oxygen atoms with halogen (X_2), interhalogen (XY), and halogen containing compounds (RX) have recently come under investigation in several molecular beam laboratories. These reactions are of current interest for several reasons. They are known to proceed *via* relatively long-lived collision complexes whose decomposition dynamics and energetics can be experimentally monitored in crossed beam scattering experiments. This is accomplished by observing both the angular and velocity distributions of the reaction products. These results yield a Center-of-Mass energy distribution which can then be directly compared with the energy distribution predictions of the statistical RRKM-AM unimolecular decomposition model proposed by Herschbach and his coworkers.[1] These reactions are also of interest as the ground state reactants approach on a triplet potential energy surface which correlates in many cases to an excited state of the triatomic reaction intermediate. The possibility therefore arises that reaction might proceed by a triplet → singlet surface crossing.

Crossed beam studies of the reaction $O(^3P) + Cl_2,$[2,3,4] $Br_2,$[4,5] and I_2[4,5] have been reported in the literature. These investigations were carried out in part to probe the nature of the reaction mechanism, and in doing this, to infer something about the structure of the reaction intermediate for each system. The results from these studies are consistent with the reactions proceeding by a collision complex mechanism, with only the OCl_2 collision complexes formed in the high collision energy studies of the $O + Cl_2$ reaction[2,3] having lifetimes shorter than one rotational period of the complex. The long-lived nature of the collision complexes formed in the low energy studies suggests that the complex for each reaction rests in a relatively deep potential energy well. For example, this well is believed to be on the order of 20 kcal/mole for the OBr_2 complex.[4] This initially suggests that the $O + X_2$ reactions proceed *via* a surface crossing to the lowest (most stable) singlet potential energy surface which corresponds to the bent, symmetric XOX structure. The Cl O-Cl and Br-O-Br species are in fact known to be chemically stable.[6,7] These are 20 electron systems having bent structures which Walsh's molecular orbital correlation diagrams[8] predict to be singlet species having the following MO configuration:

$$\text{XOX(singlet, bent)} \quad (1\sigma)^2(2\sigma)^2(1\pi)^4(2\pi)^4(3\pi^*)^4 \quad (1)$$
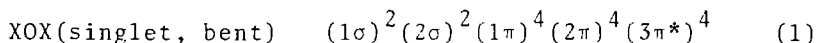
However, the "electronegativity ordering rule" derived from Walsh's orbital correlation scheme predicts that the least electronegative atom should occupy the central position of a given triatomic molecule, consistent with an OXX geometry for all halogens except OF_2. Walsh's orbital ordering scheme suggests that OXX triplet species should have bent configurations with the following MO configuration:

$$OXX(\text{triplet, bent}) \quad (1\sigma)^2(2\sigma)^2(1\pi)^4(2\pi)^4(3\pi*)^3(3\sigma*) \quad (2)$$
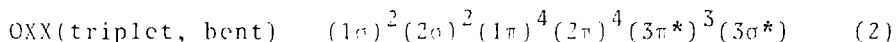
Experimental confirmation of a stable O-Cl-Cl entity has been found in cryogenic matrix isolation experiments.[9] It has been suggested by Herschbach and his coworkers,[10] as well as by Walsh in his original paper,[8] that a different MO configuration might better describe near linear OXX compounds in which the $3\sigma*$ orbital actually lies lower in energy than the $3\pi*$ orbital, resulting in an alternative triplet MO configuration:

$$OXX(\text{triplet, linear and possibly bent})$$

$$(1\sigma)^2(2\sigma)^2(1\pi)^4(2\pi)^4(3\sigma*)^2(3\pi*)^2 \quad (3)$$
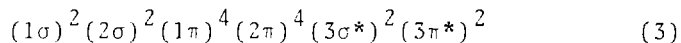
In this case a triplet ground state rather than a singlet ground state is predicted for near linear OXX triatomics.

This may persist for bent geometries as well.[4] This then allows for the presence of a relatively deep well in the triplet OXX surface which can explain the long-lived nature of the collision complexes without requiring a triplet → singlet surface crossing. In support of this argument is the behavior of the $O(^3P) + F_2$ system, which, in spite of its large exoergicity, is found to have a very low reaction probability in flow tube experiments.[11] This implies the presence of a large activation energy for this process. Since O atoms are less electronegative than F atoms, Walsh's rules would predict an F-O-F geometry to be a more stable reaction intermediate for this reaction. The low reaction probability for the $O(^3P) + F_2$ reaction supports the contention that $O + X_2$ reactions proceed on triplet potential energy surfaces via end-on attack of the oxygen atom, with the singlet surface remaining inaccessible to the initially formed triplet complex. In cases where an attractive well exists in the triplet surface ($O + Cl_2$, Br_2, I_2) a long-lived complex will be formed ultimately leading to reaction. In cases where a barrier exists in place of an attractive well in the triplet surface, i.e., $O + F_2$, reaction will not occur easily at thermal energies. (Note that insertion of $O(^3P)$ into the F-F diatomic is highly unfavorable process requiring a large activation energy.) Finally, it is presumed that the OXX triplet surface must cross the XOX singlet

surface is, highly bent geometries, implying that ends of these
reactions at high total energies should lead to the then
accessible surface crossing. High energy collisions
occurring with C_{2v} symmetry would be the most likely can
didate for this triplet → singlet crossing.

Studies of the $O(^3P) + XY$ systems $XY = ICl, IBr$
have also been carried out in crossed beam experiments
using effusive oxygen atom beam sources.[1,5,12] These
experiments have provided compelling evidence that these
reactions are governed by the geometrical constraints
imposed by Walsh's electronegativity ordering rule, and
hence, *do not* proceed *via* a triplet → singlet surface
crossing. Specifically, for the O + ICl, IBr systems the
iodine atom is the least electronegative atom present.
Walsh's rule predicts that the triplet complexes should
therefore be O-I-Cl and O-I-Br. These reactions are found
to yield exclusively IO reaction product, which is nearly
thermoneutral for each reaction. ClO and BrO are not
observed in these studies even though they are far more
exoergic than the IO channel. From this, one can only con-
clude that the long-lived complex remains on the triplet
surface. If a crossing did occur, resulting in an XOY
statistical complex, dissociation would be expected to
proceed nearly exclusively by the more exoergic ClO and
BrO channels.

In this paper results are presented for the reactions
$O(^3P) + ICl$, CF_3I obtained with our supersonic atomic
oxygen beam source. The ICl reaction was chosen as the
first reaction to be studied with this beam source since
some information was previously available about its reac-
tion mechanism, and since the narrower velocity distri-
bution of our source would hopefully add fresh insight
into the unimolecular decomposition of the O-I-Cl complex.
In a previous study Grice and his coworkers applied a
long lived collision complex model to deduce a bond energy
for the IO radical.[5,12] The applicability of using a long-
lived complex model here is not very convincing. Further-
more, the wide velocity spread of his effusive oxygen atom
beam makes quantitative assessment of the reaction energetics
difficult. Grice and his coworkers have also studied the
iodine abstraction reaction $O + CF_3I$,[13] using an oxygen
seeded in helium or neon microwave discharge beam source.
The IO product from this reaction at two collision energies
shows no evidence of the strong peaking on the realtive
velocity vector which is expected from the domination of
orbital angular momentum in a reaction with a relatively
large cross section and expected to proceed by a long-lived
collision complex. At both collision energies some product

is observed with more intense [...] than [...] the total
available energy, and hence the agreement with their theoretical
theory is very poor. Most surprisingly, their model calculation reduced the number of oscillators participating
in energy sharing from 15 to 5, and required increasing
the available energy to more than twice its maximum possible
value to produce a best fit to their data, while still
failing to account for the high energy product they
observed.

The results from our investigation of the O + ICl
reaction using a supersonic oxygen atom beam are in fairly
good agreement with the results of Grice and his coworkers.
The lifetime of the complex appears to be shorter (indicated
by the lack of forward-backward symmetry of the product IO
flux in the Center-of-Mass reference frame) and a slightly
higher bond energy is found for the IO radical. In con-
trast to this, our results for the O + CF$_3$I reaction are
not in agreement with Grice's study. We have been able
to fit our data with statistical theory using only the
energy which is actually available for product translation
and have not made any assumptions about an "effective"
number of active oscillators. The IO bond energy deter-
mined in the O + ICl experiment agrees well with that
needed to fit the O + CF$_3$I results. This reaction is found

to be similar to the I + CH$_3$I reaction which has been pre-
viously studied in detail.[14]

EXPERIMENTAL

The crossed beam apparatus used in these studies was
similar in design to one which has been previously des-
cribed in detail.[15] The seeded, supersonic atomic oxygen
beam source used in these studies was very similar to the
source described in Chapter II of this thesis. It was
actually a preliminary version of the current source,
operating with *significantly* lower pumping speed (using a
Varian HS-10 diffusion pump rather than a Varian VHS-400,
or having approximately half the pumping speed of the
current system) and having a larger nozzle orifice, ca.
0.102 mm in diameter, than that currently employed. The
atomic beam was produced by discharging a 5% O$_2$ in argon
mixture at 100 torr total pressure by 100 watts of 14.2
megahertz radio frequency power. The resulting atomic
oxygen velocity distribution had a peak velocity of 1.05 x
10^5 cm/sec and a FWHM velocity spread of 40%. This was
determined with conventional "single-shot" time-of-flight
velocity analysis with a dwell time per channel of 4 μsec.
Molecular dissociation was found to be about 80% under the

above operating conditions. The atomic oxygen velocity
distribution is wider than those typically found in low
temperature, high pressure supersonic expansions, but is
significantly narrower than the Maxwellian distributions
produced from effusive discharge sources. The relatively
large width of the atomic oxygen velocity distribution
can be attributed to the low number density at the orifice
of the nozzle, which is a direct consequence of both the
high effective plasma temperature in the nozzle, and the
low stagnation pressure at which the nozzle was operated.
In this earlier version of the source relatively low
stagnation pressures were required to ensure plasma
stability. In contrast to this, the current version of
the oxygen seeded in argon plasma beam source can be
operated at pressures approaching 400 torr with 10% O_2
in argon gas mixtures, resulting in narrower velocity
distributions and much higher atomic oxygen fluxes than
those obtainable with the source used in the O + ICl,
CF_3I experiments.

The ICl used in these experiments was practical
grade obtained from Matheson, Coleman and Bell. It was
held in a glass reservoir which was heated to 310K by a
temperature regulated oil bath. At this temperature the
ICl vapor pressure was observed to be 70 torr with a

baratron pressure gauge. The actual seeded ICl beam was
produced by flowing argon through the ICl reservoir to
bring the total operating pressure to 240 torr. This was
done to increase the stability of the ICl beam intensity
and to improve the beam's operating characteristics. This
mixture, approximately 50% ICl, was expanded through a
0.1 mm quartz nozzle which was held at 329 K to prevent
condensation of ICl in the nozzle. In fact, the entire
glass gas line was always heated to at least 10K above
the reservoir temperature to prevent ICl condensation.
The seeded ICl beam produced in the above manner was
characterized with single-shot time-of-flight techniques,
and was found to have a peak velocity of 5.02×10^4 cm/sec
and a FWHM velocity spread of 29%. Liquid nitrogen
cooled foreline traps were always placed between the
diffusion pump and its mechanical backing pump to prevent
ICl from fouling the mechanical pump's oil.

The supersonic CF_3I beam was run neat at 250 torr
total pressure through the same source used in the ICl
experiment. The CF_3I was obtained from PCR Research
Chemicals Inc., and was used without further purification.
The CF_3I beam produced in this manner had a peak velocity
of 2.66×10^4 cm/sec and a FWHM velocity spread of 30%.
The above terminal velocity of the CF_3I beam implies that

the supersonic expansion effectively converted the trans-
lational, rotational, and approximately two low frequency
vibrational degrees of freedom to beam kinetic energy.
Under these condition the reacting CH_3I molecules are
left with an average internal energy of about 1 kcal/mole.
The mean collision energy for the ICl reaction was 2.36
kcal/mole with a FWHM of 0.8 kcal/mole, while that for
the CH_3I reaction was 2.18 kcal/mole again with a FWHM
energy spread of 0.8 kcal/mole.

Laboratory angular distributions of product number
density were taken by repeated scans of 100 second counts
at each angle. Time normalization of the recorded signal
was carried out when required. The oxygen beam was
modulated at 150 Hz with a Bulova tuning fork chopper.
The actual signal at each laboratory angle was obtained
by subtracting the chopper closed count from the chopper
open count. The IO product signal at the peak of its
angular distribution for each system was ca. 15 counts/sec
with a background of 50 counts/sec. Product velocity
distributions at each angle were obtained with cross-
correlation time-of-flight techniques[16,17] with a dwell
time per channel of 12 μsec. For these experiments a
pseudorandom sequence having 50% duty cycle was employed
which had a 255-bit pattern. Representative counting times

for product velocity analysis varied between one and three
hours per angle.

RESULTS

 The only product detected in the $O(^3P)$ + ICl reaction
was the IO radical, indicating that the geometric con-
straints imposed on the $O(^3P)$ + ICl collision complex by
Walsh's electronegativity ordering rule are operative.
This also indicates that the reaction does not primarily
proceed by a triplet - singlet surface crossing. However,
the increased background at m/e = 51, the ClO mass, and
uncertainties about the relative detection efficiency of
ClO with respect to IO, only permits us to estimate at
this time that less than 10% of the reaction goes by the
more exoergic reaction channel which yields I and ClO as
products. Similarly, the only reaction product detected
in the $O(^3P)$ + CF_3I reaction was again the IO radical.

 The laboratory angular distributions of IO product
from these reactions are shown in Fig. 1. The error bars
in this figure represent one standard deviation from the
mean of 10 independent measurements. The product for both
reactions is found to peak near the center-of-mass angle
for each system with slight bimodality being apparent in

the distribution from the $O(^3P)$ + ICl reaction. This bimodality implies that a large fraction of the initial orbital angular momentum of the reactants appears as orbital angular momentum of product in the decomposition dynamics of the O-I-Cl collision complex. The product flux distributions for these reactions are shown in Figs. 2 and 3 as a function of laboratory velocity. The contour plots of Center-of-Mass IO product flux, obtained from laboratory angular and velocity distributions with Siska's iterative deconvolution technique,[18] are shown in Figs. 4 and 5 for the ICl and CF_3I reactions, respectively. These contours are the deconvoluted Center-of-Mass flux distributions, which, when averaged over the reactant beam velocities, produce the best-fit solid lines shown in Figs. 1, 2, and 3.

The laboratory number density angular distributions for these reactions appear to peak near the respective center-of-mass angles. This can be attributed to the relatively high detection probability for low energy reaction products which fall near the center-of-mass, since the transformation Jacobian which relates Center-of-Mass flux, $I_{cm}(\theta,u)$, to Laboratory number density, $N(\theta,v)$, is v/u^2.[19,20] In reality, the IO product flux peaks strongly on the relative velocity vector for each system, well removed from the center-of-mass of each

system. This can be clearly seen in Figs. 4 and 5. Product time-of-flight data could only be taken within ca. 25 degrees of the velocity vector of the center-of-mass due to the rapid fall-off of product number density in the Laboratory reference frame, as discussed above. At angles further removed than this counting times became prohibitively long for obtaining acceptable signal-to-nosie levels.

Examination of the product IO flux distributions in the Center-of-Mass reference frame reveals that symmetry does not exist about 90° for either reaction system. The O-I-Cl and CF_3I-O collision complexes therefore have lifetimes, which, on the average, are slightly less than their respective rotational periods. Fitting of the angular and velocity data with Center-of-Mass energy and angular distributions, $P(E')$ and $T(\theta)$, which were assumed to be uncoupled, indicates that the ratio of flux at 0° to that at 180° is ca. 2.0 for the ICl reaction and ca. 2.2 for the CF_3I reaction. The Center-of-Mass velocity and angular distributions actually appear to be coupled for both reactions. Figures 4 and 5 show that the most probable flux velocity actually decreases smoothly as the Center-of-Mass angle increases from 0° to 90°.

The experimental P(E') distributions shown in
Figs. 6 and 7 are the average energy distributions between
0° and 90°. The theoretical curves shown in these figures
were obtained by calculating P(E') with the RRKM-AM
model[1,21] for five discrete collision energies spanning
the experimental range, and these P(E') were then summed
over the distribution of collision energies in the experi-
ment. The parameters used in the calculations are shown
in Tables I and II. The theoretical curves in Figs. 6
and 7 were calculated for three values of the IO bond
energy: 53.0, 55.0, and 57.0 kcal/mole. All of the
vibrational modes in each collision complex, O-I-Cl and
CF_3-I-O, were assumed to participate in energy sharing.
The O-I-Cl complex was assumed to be bent at an angle of
115° with the least electronegative atom, iodine, in the
central position. This bent geometry for the triplet
O-I-Cl complex seems feasible when the earlier MO arguments
are taken into consideration. The bond lengths and
stretching frequencies were estimated from experimental
bond lengths and vibrations of the diatomics ICl and IO
using a simple bond energy bond order treatment.[22] The
O-I-Cl bending frequency was assumed to be similar to
the bend for ClO_2 and Cl_2O for lack of more similar mole-
cules. Similarly, the vibrational frequencies and geo-

metries for CF_3 and CF_3I^{23} were used to derive estimates
of the CF_3I-O complex and its critical configuration.
Note however that the choice of frequencies and the
effect of geometry on the calculated $P(E')$ is miniscule
even though these factors do influence the decomposition
rate of the complex. The stability of the complexes in
both reactions was assumed to be 16 kcal/mole. Again,
these well depths have little effect on the product
translational energy distribution, but do significantly
influence the lifetime of the complex. Initially, cal-
culation of the maximum exit-channel centrifugal barrier,
B'_m, followed the prescription of Safron et al.[1] In this
formulation B'_m for a "loose" collision complex is given
by the following expression:

$$B'_m = (\frac{\mu}{\mu'})^{3/2} \ (\frac{C_6}{C'_6})^{1/2} \ E_c \qquad (4)$$

where μ and μ' are the reduced masses of the reactants
and products, C_6 and C'_6 are the respective long-range
attraction force constants, and E_c is the collision energy.
The C_6 constants were estimated using the Slater-Kirkwood
method[24] and the polarizabilities which were available
for some of the species. The other polarizabilities were
estimated by the additive method.[25] An improved fit to

the ICl data was obtained by increasing B_m' to 0.454 E_c, approximately double the value calculated with the C_6 constants, 0.26 E_c. This increase of B_m' moved the calculated peak of $P(E')$ from 0.9 to 1.5 kcal/mole, and slightly increased the high energy tail of the energy distribution.

DISCUSSION

In a crossed beam experiment the high energy fall-off of the product $P(E')$ distribution can be used to set a rigorous lower bound on the exoergicity of the process under investigation. The accuracy of this determination depends significantly on good specification of the relative collision energy, E_c, as this reduces uncertainties resulting from any energy dependence in the reactive cross section. In their $O(^3P)$ + ICl study[5,12] Grice and his coworkers employed an effusive microwave discharge source for generating atomic oxygen. The 95% FWHM velocity spread of this Maxwellian oxygen beam leads to a large uncertainty in their collision energy. This can be seen by examining the expression which gives the relative collision energy, E_c, for a crossed beam experiment in which the beams intersect at 90°:

$$E_c = \frac{m_2 E_1 + m_1 E_2}{m_1 + m_2}$$ (5)

For a reaction in which a large mass mismatch exists between the reactants, as in the O + ICl reaction, Equation (5) reveals that E_c and its uncertainty will strongly depend on the velocity distribution of the lighter reactant. Moreover, the wide velocity spread of Grice's effusive oxygen beam and the concomitant uncertainty it produces in E_c further complicates interpretation of this particular experiment since, in the almost thermoneutral $O(^3P)$ + ICl reaction, E_c accounts for a large fraction of the total energy available for translation. In our experiment the use of two intersecting supersonic beams has allowed this reaction to be studied with a relatively well-defined collision energy, allowing an accurate minimum reaction exoergicity to be assigned. We find this lower bound on the $O(^3P)$ + ICl exoergicity to be ca. 3.5 kcal/mole under conditions where E_c was 2.36 ± 0.8 kcal/mole.

Due to the small number of internal degrees of freedom in the O-I-Cl triatomic complex the high energy fall-off of $P(E')$ is more sensitive to the total energy available in the complex than to the dynamics of its decomposition.

This has allowed us to predict the reaction exoergicity,
without a detailed knowledge of the IO internal energy
distribution, by examining the high energy fall-off of the
experimental P(E') distribution. This procedure leads to
an exoergicity $\Delta H = -5.5 \pm 2.0$ kcal/mol for the $O(^3P)$ +
ICl $\rightarrow$ IO + Cl reaction. This value, when combined with
the known heats of formation for O, ICl, and Cl,[26] allows
us to deduce a new value for the IO bond energy: $D_o(IO) =$
55.0 $\pm$ 2.0 kcal/mole. The P(E') calculations based upon
the RRKM-AM unimolecular decomposition model shown in
Fig. 6 agree with this IO bond energy when the maximum
centrifugal barrier, B'_m, is taken as an adjustable para-
meter in the calculations.

   For collisions in which the long-range dispersion
force between the reactants determines the maximum impact
parameter for capture, B'_m depends simply on the ratio of
the entrance to exit channel C_6 constants, as shown in
Equation (4). The C_6 constant for O + ICl is estimated
to be 1920 kcal $Å^6$ mole^{-1} or about half the C'_6 value for
Cl + IO, 3780 kcal $Å^6$ mole^{-1}. In order to fit the experi-
mental results we have had to increase the C_6/C'_6 ratio
used in Equation (4) by a factor of four over that cal-
culated with the Slater-Kirkwood method. This cannot be
physically realistic in view of the much greater polariz-
ability of chlorine, 2.14 $Å^3$, relative to that of oxygen,

0.77 Å^3. The capture cross section calculated with either the original C_6 value, $\sim 55 \text{ Å}^2$, or with the larger one, $\sim 88 \text{ Å}^2$, is about an order of magnitude larger than that expected for the $O(^3P)$ + ICl reaction based upon the known rate constants for the $O(^3P)$ + Cl_2, Br_2, and BiCl reactions.[27] This may either indicate that a large steric constraint is present in the entrance channel of this reaction which substantially reduces the number of reactive collision trajectories, or that the long range orbiting assumption used in calculating the capture cross section is not valid for this system. With the above discussion in mind we feel that it is not yet clear whether the improved $P(E')$ fit with the larger B_m' value indicates a "non-statistical" translational energy distribution.

The exoergicity found in this study for the $O(^3P)$ + ICl reaction, $\Delta H = -5.5$ kcal/mole, is higher than that proposed by Grice and his coworkers, $\Delta H = 3.4$ kcal/mole.[12] Their value was obtained by fitting the IO velocity distribution at the laboratory center-of-mass angle with a theoretical distribution calculated from Herschbach's RRKM-AM statistical decomposition model. This manner of obtaining the exoergicity is an extremely poor one for this system as severe Jacobian enhancement of slowly moving reaction products tends to overwhelm the information contained in the (more important) high energy tail. It must

also be stated that Grice's reliance on statistical cal-
culations to determine the bond energy of IO is somewhat
questionable for this reaction. The RRKM lifetime is
calculated to be exceedingly short, 0.3 psec, a time
regime in which nonstatistical effects have been observed
in several other reactions. Also, the density of states
in the complex at the dissociation energy is very low,
approximately 1 per cm^{-1}. Finally, uncertainties in the
treatment of angular momentum may introduce too much
flexibility to the model, making it unreliable for thermo-
dynamic data determination. In spite of the substantial
difference which exists between the reaction exergicity
found in this study and Grice's value, the derived IO
bond energies are actually in fair agreement with each
other: 55.0 + 2.0 kcal/mole (this study) and 53.0 + 3.0
kcal/mole (Ref. 12).

In support of our IO bond energy, which was obtained
without reliance on statistical models, other experimental
information must be taken into consideration. The product
P(E') distribution from the $O(^3P)$ + CF_3I reaction is shown
in Fig. 7 to agree well with statistical calculations using
the IO bond energy determined above. The high density of
states for the CF_3I-O complex at its dissociation energy

is about 10^7 per cm^{-1}, lending more credibility to the use of statistical treatment than in the ICl reaction. Our IO bond energy is also in good agreement with that determined in a flame photometry experiment,[28] and falls below the rigorous upper bound on $D_o(IO)$, 62.8 kcal/mole, which was reportedly determined from predissociation of the upper $IO(^2\pi)$ state.[12]

In their study of the $O(^3P)$ + CF_5I reaction at two higher collision energies[15] Grice and his coworkers observed IO product with energies far exceeding the total energy available for translation. The conditions of their reactants are too well specified to attribute this to uncertainty in internal energy. The explanation of this serious discrepancy must therefore lie in some systematic error. Their reported Center-of-Mass angular distribution shows no peaking on the relative velocity vector even though the kinematics of the reaction virtually requires this. In our experiment the product flux peaks on the relative velocity vector, as shown in Fig. 5, and the product translational energy distribution does in fact fall within the bounds imposed by energy availability in the complex.

The asymmetry of product about 90° in the Center-of-Mass reference frame found for both reactions is not inconsistent with statistical calculations if the intermediates in both reactions are assumed to be stable by 16 kcal/mole with respect to reaction products. The rotational period is estimated to be 0.8 - 3.0 psec for the ICl and 1-5 psec for the CF_3I reactions, in each case comparable to the calculated lifetime. The forward-backward symmetry found in the study of O + ICl at a collision energy of 0.81 kcal/mole by Radlein et al.[5] is not viewed as being in disagreement with our result as large uncertainties exist in the rotational period and stability of the O-I Cl complex, as well as in their collision energy.

Finally, the $O(^3P)$ + ICl reaction appears primarily to proceed adiabatically on a triplet potential surface. This is supported by the apparent absence of ClO as a primary reaction product. As the I + ClO decomposition channel is roughly 10 kcal/mole more exoergic than the IO + Cl channel we infer that the O-I-Cl collision complex remains on the triplet surface, from which the I + ClO product channel is inaccessible. However, due to the higher exoergicity and expected wide spread of ClO in the LAB reference frame (due to mass effects) some certainty

still exists about the branching ratio of the ClO relative
to the IO product channel. Study of this reaction at much
higher relative collision energies or with internally
excited ICl might ultimately enable the $O(^3P)$ + ICl system
to access the singlet surface, if it is not already doing
so.

CONCLUSION

Study of the reaction $O(^3P)$ + ICl in a crossed beam
experiment employing a supersonic atomic oxygen beam source
has led to a new value for the bond energy of the IO radical,
$D_0(IO)$ = 55 ± 2 kcal/mole. This value was obtained by
examining the high energy fall-off of the product trans-
lational energy distribution without reliance on any
statistical decomposition model. The product translational
energy distribution for the $O(^3P)$ + CF_3I reaction agrees
quite well with RRKM-AM predictions when the above IO
bond energy is used in the calculation. The two reactions
appear to proceed *via* collision complexes whose mean life-
times are slightly less than their respective rotational
periods. The $O(^3P)$ + ICl reaction has also been shown
primarily to proceed adiabatically in a triplet potential

surface, as indicated by the apparent absence of ClO reaction product. Walsh's electronegativity ordering rule is seen to be operative, with the least electronegative species resting in the central position of the reaction complex. An attractive well in the triplet surface can be inferred from the results of this experiment.

REFERENCES

1. S. A. Safron, N. D. Weinstein, D. R. Herschbach, and J. C. Tully, Chem. Phys. Lett. 12, 564 (1972).

2. P. A. Gorry, C. V. Nowikow, and R. Grice, Chem. Phys. Lett. 49, 116 (1977).

3. P. A. Gorry, C. V. Nowikow, and R. Grice, Chem. Phys. Lett. 55, 19 (1978).

4. D. D. Parrish, and D. R. Herschbach, J. Amer. Chem. Soc. 95, 6133 (1973).

5. D. St. A. G. Radlein, J. C. Whitehead and R. Grice, Mol. Phys. 29, 1813 (1975).

6. F. A. Cotton and G. Wilkinson, Advanced Inorganic Chemistry, Second Ed. (Interscience, London, 1966) pp. 565-7.

7. C. Campbell, J. P. M. Jones, and J. J. Turner, Chem. Commun. 888 (1968).

8. A. D. Walsh, J. Chem. Soc. 2266 (1953).

9. M. M. Rochkind and G. C. Pimentel, J. Chem. Phys. 46, 4481 (1967).

10. D. D. Parrish and D. R. Herschbach, J. Amer. Chem. Soc. 95, 6133 (1973); Footnote 16.

11. M. Kaufman and C. E. Kolb, Chem. Inst. 3, 175 (1971).

12. D. St. A. G. Radlein, J. C. Whitehead, and R. Grice, Nature 253, 37 (1975).

13. P. A. Gorry, C. V. Nowikow, and R. Grice, Chem. Phys. Lett. 55, 24 (1978).

14. J. M. Farrar and Y. T. Lee, J. Chem. Phys. 63, 3639 (1975).

15. Y. T. Lee, J. D. McDonald, P. R. LeBreton, and D. R. Herschbach, Rev. Sci. Instrum. 40, 1402 (1969).

16. K. Sköld, Nucl. Instrum. Meth. 63, 114 (1968).

17. V. L. Hirschy and J. P. Aldridge, Rev. Sci. Instrum. 42, 381 (1971).

18. P. E. Siska, J. Chem. Phys. 59, 6052 (1973).

19. L. A. Intemann, Ph.D. dissertation, Harvard University, Cambridge, Massachusetts, 1967.

20. T. T. Warnock and R. B. Bernstein, J. Chem. Phys. 49, 1878 (1968).

21. P. J. Robinson and K. A. Holbrook, Unimolecular Reactions (Wiley-Interscience, New York, 1972).

22. H. S. Johnston, Gas Phase Reaction Rate Theory, (The Ronald Press Co., New York, 1966).

23. Vibrational spectrum for CF_3I: L. H. Ngai and R. H. Mann, J. Mol. Spect. 38, 322 (1971); for CF_3: D. E. Milligan and M. E. Jacox, J. Chem. Phys. 48, 2265 (1968); for ICl: G. Herzberg, Spectra of Diatomic Molecules, (Van Nostrand, New York, 1950).

24. J. C. Slater and J. G. Kirkwood, Phys. Rev. 37, 682 (1931).

25. J. O. Hirschfelder, C. F. Curtiss, and R. B. Bird, Molecular Theory of Gases and Liquids (John Wiley and Sons, New York, 1954) pp. 947-51.

26. H. M. Rosenstock, K. Draxl, B. W. Steiner, and J. T. Herron, J. Phys. Chem. Ref. Data, 6, Suppl. #1, 1977.

27. M. A. A. Clyne, P. B. Monkhouse, and L. W. Townsend, Inter. J. Chem. Kinet. 8, 425 (1976).

28. L. F. Phillips and T. M. Sugden, Trans. Far. Soc. 57, 914 (1961).

Table I.

		OICl*	OICl$^+$
Bond length Å	r_{IO}	2.0	1.8^7
	r_{ICl}	2.5	3.5
Bond Angles degrees	< OICl	115	115
Frequencies cm^{-1}	V_{IO}	486	683
	V_{ICl}	271	R.C.
	δ_{OICl}	250	25
Moments of Inertia AMU·Å^2		175.4	301.3
		132.5	262.8
		43.0	38.5

Energetics (kcal mol^{-1})   Polarizabilities (Å^3)

ΔH	-5.5	Cl =	2.18
E_c	1.0 - 4.0	O =	0.802
$E*$	23.0 - 27.0	ICl =	7.5
$E°$	16.0	IO =	6.02

$$C_6 = 1981. \text{ kcal Å}^6 \text{ mol}^{-1}$$
$$C_6' = 3831. \text{ kcal Å}^6 \text{ mol}^{-1}$$
$$B_m' = 0.268 \, E_c$$

Table II.

		CF_3I-O*	CF_3I-O^+
Bond length Å	r_{IO}	2.0	1.87
	r_{CI}	2.54	2.82
	r_{CF}	1.33	1.33
Angles	$<CIO$	115	115
Degrees	$<ICF$	109	
Frequencies cm^{-1}	V_{IO}	486	683
	V_{CF}	1195, 1195, 1067	1223, 1223, 1077
	V_{CI}	202	R.C.
	δ_{CF}	730, 529	715, 521
	δ_{CI}	132, 132	26, 26
	δ_{CIO}	200, 200	40, 40
	τ	150	30
Moments of Inertia $AMU \cdot Å^2$		334.8	1091
		333.8	1091
		89.6	99.4

Energetics (kcal mol^{-1})

ΔH	-2.0
E_c	1.0 - 4.0
E*	20.0 - 24.0
E*	16.0

Polarizabilities ($Å^3$)

CF_3I	=	7.33
CF_3	=	3.43
O	=	0.802
IO	=	6.02

Table II.   (Continued)

$$C_6 = 2440. \text{ kcal } \mathring{A}^6 \text{ mol}^{-1}$$

$$C_6' = 7104. \text{ kcal } \mathring{A}^6 \text{ mol}^{-1}$$

$$B_m' = 0.105 \text{ E}_c$$

FIGURE CAPTIONS

Fig. 1. Laboratory angular distributions of IO product number density from the reaction O + ICl, CF_3I. Error bars represent one standard deviation from the mean of 10 measurements at each angle.

Fig. 2. Product IO flux distributions from the reaction O + ICl at eight laboratory angles. Solid lines are the best fit from the deconvolution procedure.

Fig. 3. Product IO flux distributions from the reaction O + CF_3I at seven laboratory angles.

Fig. 4. Contour map of Center-of-Mass product IO flux from the reaction O + ICl with the most probable Newton diagram.

Fig. 5. Contour map of Center-of-Mass product IO flux from the reaction of O + CF_3I.

Fig. 6. Product translational energy distributions. ••• experimental, lines are RRKM-AM calculations for three values of the IO bond energy, – – – E_{IO} = 53, ——— E_{IO} = 55, and – —— – —— E_{IO} = 57 kcal mol^{-1}.

Fig. 7. Product translational energy distributions. ••• experimental, lines are RRKM-AM calculations for three values of the IO bond energy, – – – E_{IO} = 53, ——— E_{IO} = 55, and – —— – —— E_{IO} = 57 kcal mol^{-1}.

Fig. 1

XBL 7812-14076
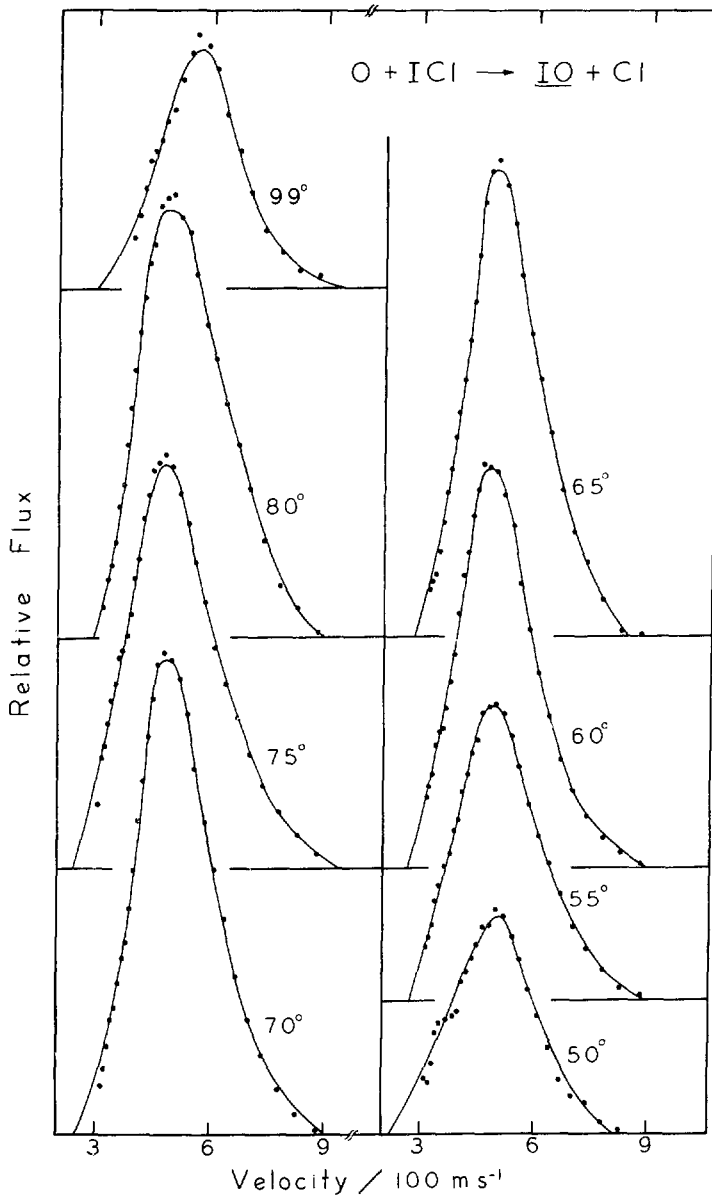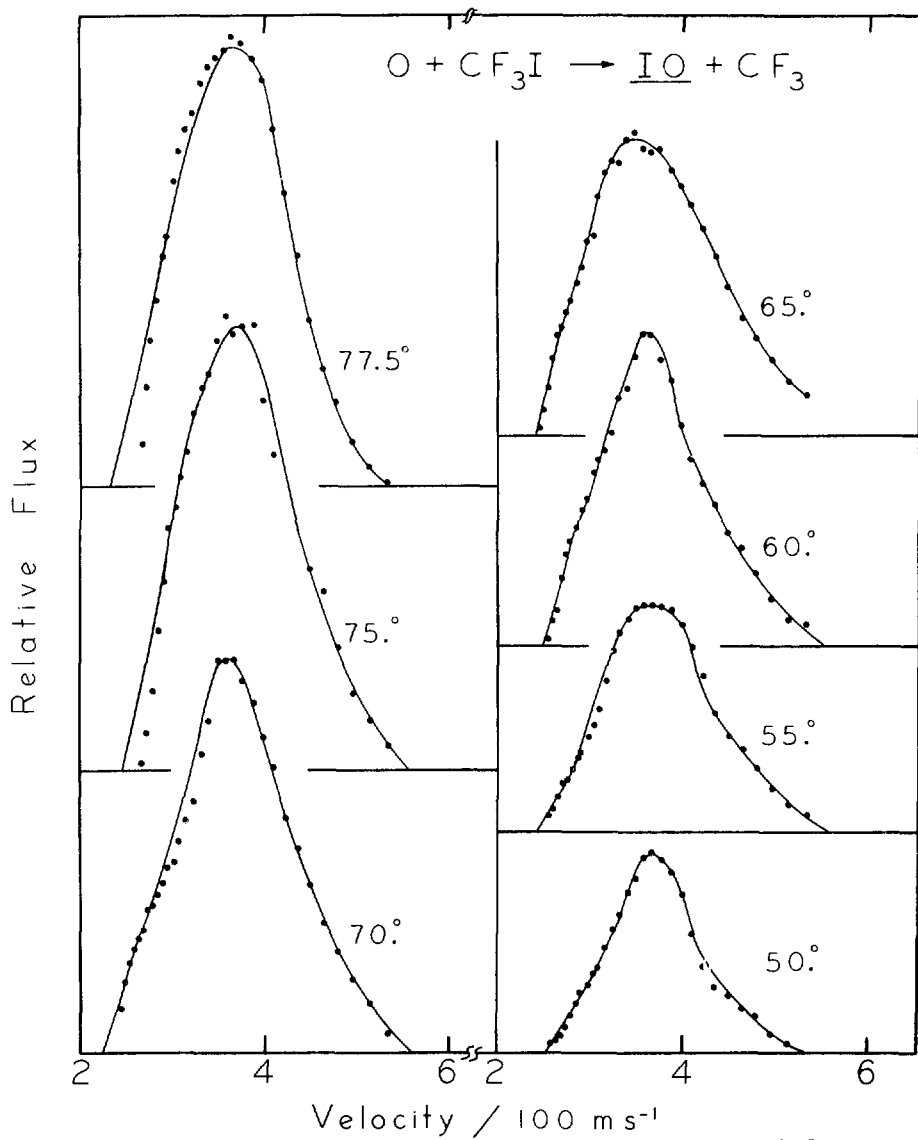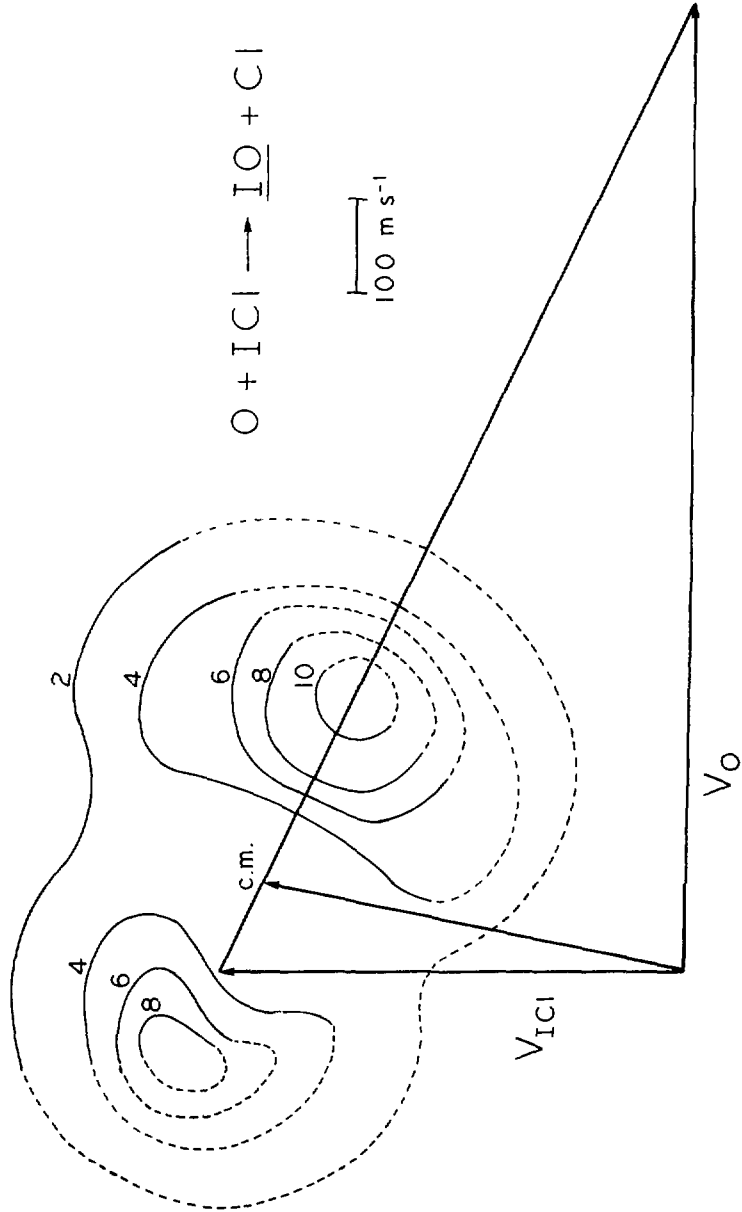
Fig. 2

Fig. 3

$O + ICl \longrightarrow \underline{IO} + Cl$

Fig. 4

XBL 7812-14055

$$O + CF_3I \longrightarrow \underline{IO} + CF_3$$

XBL 792-8647

Fig. 5

$$O + ICl \longrightarrow \underline{IO} + Cl$$

Fig. 6

XBL 7812-14051

$O + CF_3I \longrightarrow \underline{IO} + CF_3$

$P(E')$

$E'/kcal\ mol^{-1}$
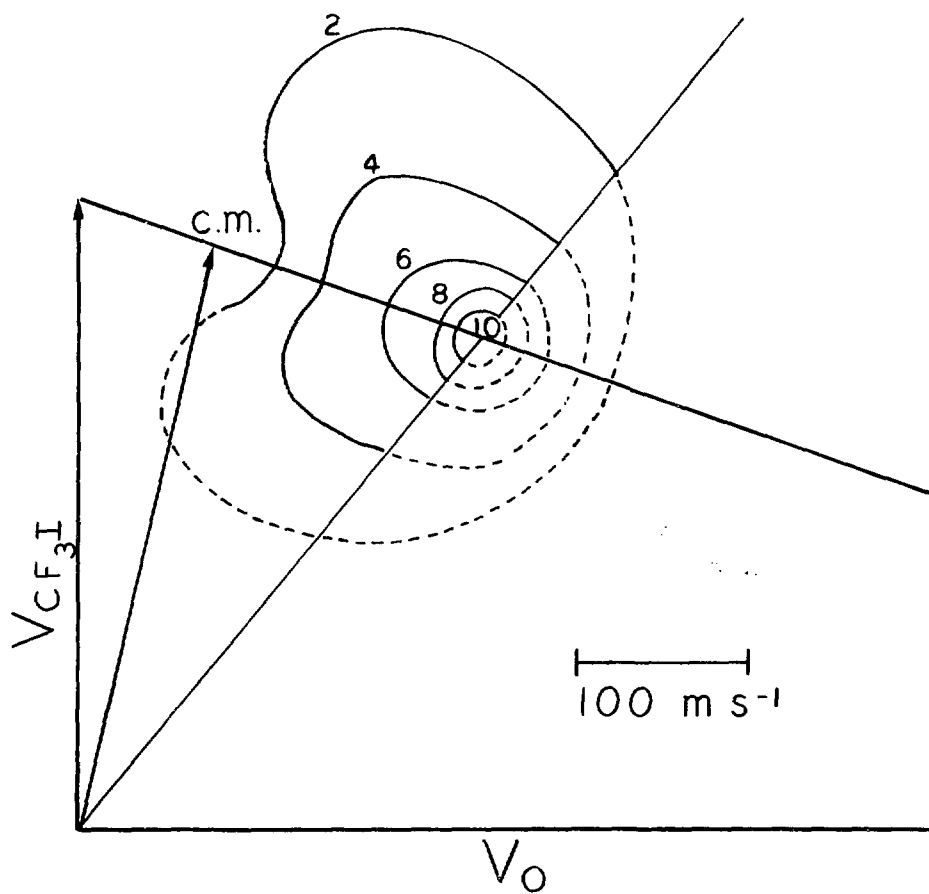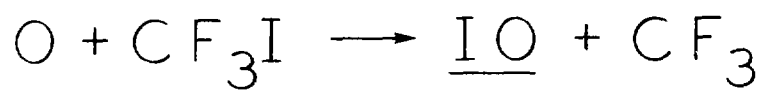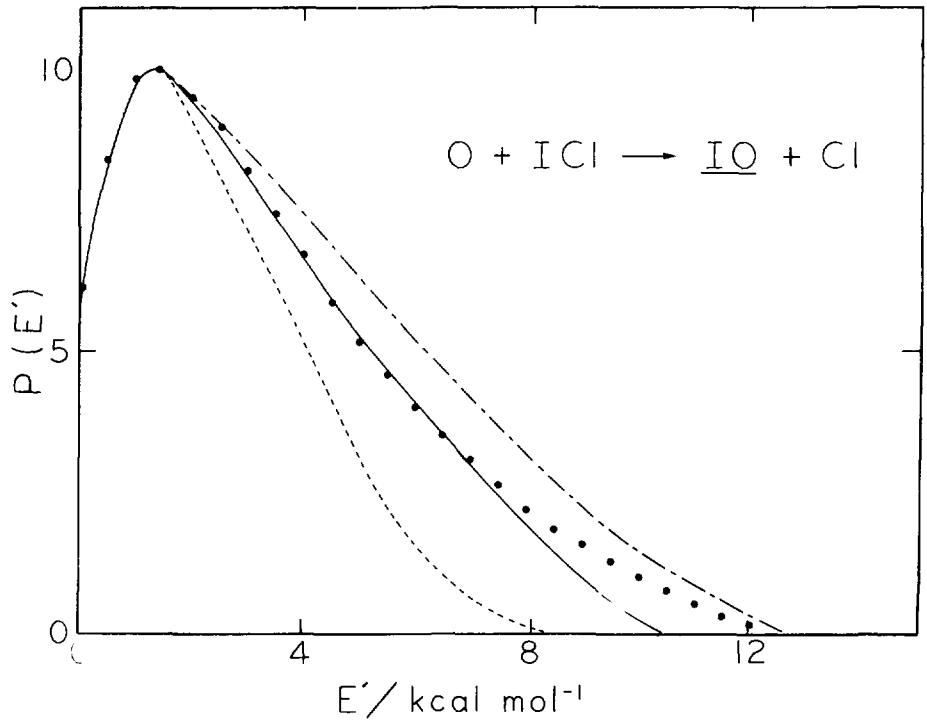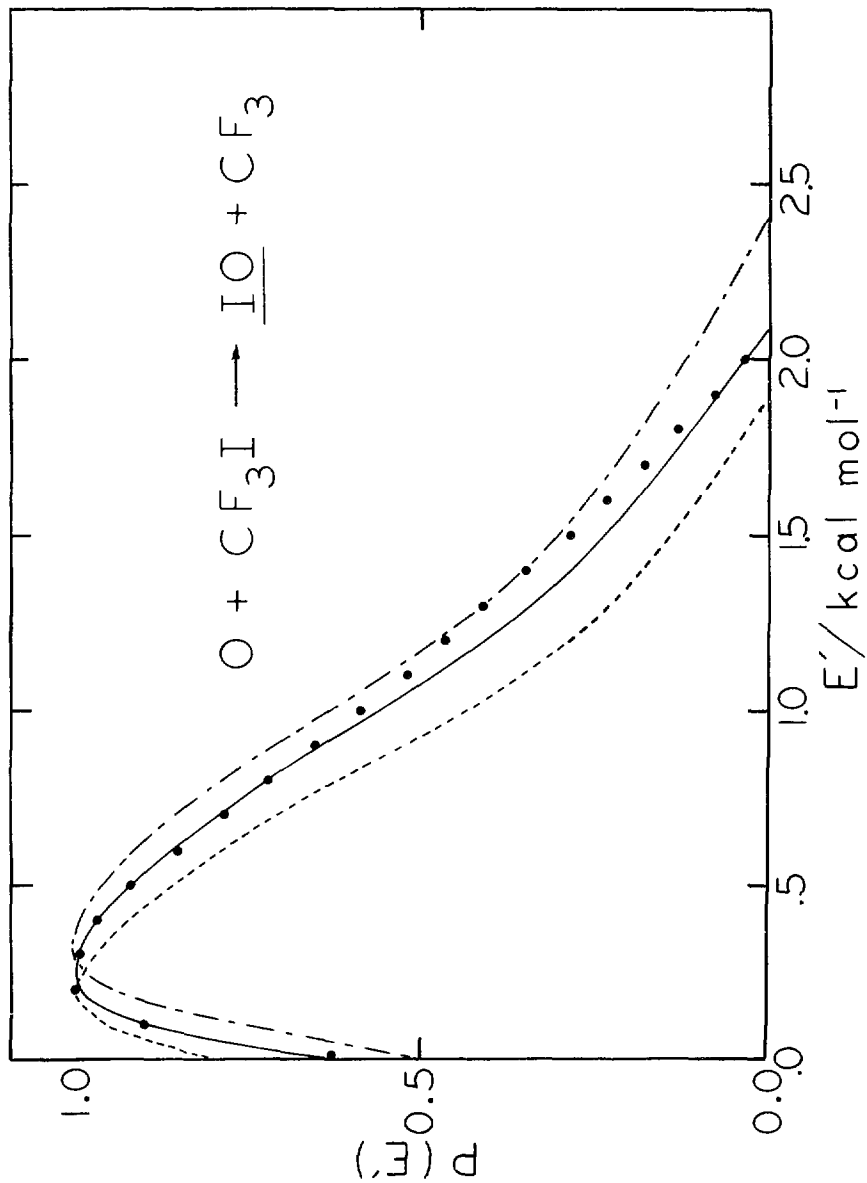
Fig. 7

XBL 7812-14050

IV. A CROSSED MOLECULAR BEAMS INVESTIGATION
OF THE REACTIONS $O(^3P)$ + C_6H_6, C_6D_6

INTRODUCTION

The reactions of ground state oxygen atoms with both
aliphatic and aromatic hydrocarbons are of considerable
interest due to their importance in combustion processes,
atmospheric chemistry, and photochemical air pollution.
A relatively large number of kinetic studies have been
reported for oxygen atom reactions with alkanes and alkenes
in which reaction rate constants have been determined.
Crossed molecular beams experiments employing photoioniza-
tion mass spectrometry have recently been conducted by
Gutman and his coworkers in order to directly identify
the elementary reaction products resulting from oxygen
atom reactions with various alkenes and alkynes.[1-3] In
contrast to the above, atomic oxygen reactions with
aromatic hydrocarbons have not been extensively studied.
The simplest reactions of this class, $O(^3P)$ + benzene and
toluene, are the only atom-aromatic hydrocarbon reactions
that have been studied by a variety of techniques.
Relative reaction rates for the $O(^3P)$ + benzene reaction
have been determined using static photolysis techniques.[4,5]
Absolute reaction rate constants for the $O(^3P)$ + benzene
reaction have been determined using pulsed radiolysis,[6]
discharge flow,[7-9] modulation-phase shift,[10,11] and flash

photolysis-NO_2 chemiluminescence[12] techniques. In spite of these studies, very little information is available on the actual elementary reaction products arising from the bimolecular reaction of atomic oxygen with benzene, and, as a consequence of this, the reaction mechanism is poorly understood. Product identification is severely complicated in the above gas phase studies by the presence of viscous, non-volatile reaction products which are possibly polymeric in character.[4,8] These non-volatile products indicate that some of the initial elementary reaction products are highly reactive species which are possibly free radicals. The major volatile reaction product which has been consistently observed is phenol, which accounts for about 10-15% of the oxygen atom consumption in these studies.[4,8,13] Phenol has been shown to account for more than 95% of the volatile products which result when this reaction is studied at atmospheric pressure.[8] Carbon monoxide has also been reported as a reaction product whose yield, in pressure dependent studies, was found to increase with decreasing pressure.[4] This pressure dependent behavior may indicate the presence of an energy rich precursor which is collisionally quenched at high pressures. However, secondary reactions may account for some of the carbon monoxide production reported in these bulk studies. In a further

attempt to identify the elementary reaction products

Sloane[15] has carried out a simple crossed beam experiment,

employing effusive beams and a non-rotatable mass spectro-

meter, in which phenol production and carbon monoxide

elimination, yielding possibly 3-pentene-1-yne, were

reported as the two open reactive pathways. It is

apparent from the above discussion that there is still

considerable uncertainty about the elementary reaction

products which arise from the electrophilic attack of

oxygen atoms on benzene, which serves as the model system

for understanding oxygen atom - aromatic ring reactions.

This paper describes the results from a series of

well-defined crossed molecular beam experiments which

have been carried out under single collision conditions

in our laboratory to elucidate the reaction dynamics and

energetics of the $O(^3P)$ + benzene reaction. The reaction

has been studied as a function of both collision energy

and isotopic substitution in order to clarify the factors

which dominate the reaction dynamics. Differential

reactive angular distributions accompanied with velocity

analysis of the reaction products at several laboratory

angles have contributed to our understanding of the

elementary reaction pathways which are operative. In

particular, these studies make use of a novel and important

feature which is inherent in crossed beam experiments employing rotating mass spectrometer detectors: the ability to identify unambiguously the primary polyatomic reaction products resulting from bimolecular reactive collisions due to the dynamic and energetic constraints which are imposed on the reaction products. These experiments are especially well suited for studying reactions involving polyatomic species since parent-daughter ion pairs created in the electron bombardment ionizer of the detector must have identical angular and velocity distributions, while reaction channels involving different dynamics (e.g. substitution versus addition reactions) are clearly distinguishable by their angular and velocity distributions. In contrast to this, traditional gas phase studies which use non-rotatable mass spectrometric particle detection for product identification are frequently severely complicated by the fragmentation of parent polyatomic species in the electron bombardment ionizers of these systems. This is particularly a problem when highly vibrationally excited polyatomic species are ionized by electron bombardment as the parent ion mass peak may be of very low intensity relative to its daughter peaks. For example, the observation of m/e = 66, $C_5H_6^+$, in the $O(^3P)$ + benzene reaction is not in itself sufficient to differentiate

between phenol fragmentation during ionization and actual

CO elimination. In the study herein described we have

made extensive use of product angular distributions to

unravel the primary reaction channels of the $O(^3P)$ +

benzene reaction.

EXPERIMENTAL

The crossed beam apparatus used in these studies was

similar in design to one which has been previously des-

cribed.[16] Briefly, two beams which are doubly differentially

pumped are crossed at 90° in a scattering chamber which has

a base pressure of ca. 1 x 10^{-7} torr. The main scattering

chamber is pumped by a 5300 ℓ/sec diffusion pump and by a

liquid nitrogen cooled cold shield which is very effective

in pumping condensable gases. Particles which are scattered

in the plane defined by the two colliding beams are detected

by a triply differentially pumped quadrupole mass spectro-

meter which rotates about the intersection point of the

two beams. The incident neutral particles are ionized in

the detector by an electron bombardment ionizer which is

operated with an electron energy of 200 eV. As the pro-

bability of ionization is proportional to the residence

time of a particle in the ionizer these experiments actually

measure the scattered particle number density, rather than particle flux, as a function of in-plane laboratory angle.

The seeded, supersonic atomic oxygen beams used in these studies were generated by a high pressure, radio frequency discharge beam source which has been described in deta elsewhere.[17,18] The high energy atomic oxygen beam was generated by discharging a 10% O_2 in helium gas mixture t 110 torr total pressure by 130 watts of R.F. power. The resulting fast atomic oxygen beam had a measured pe k velocity of 1.95 x 10^5 cm/sec and a Mach number of 5.8, hich corresponds to a FWHM velocity spread of 29%. Fo these studies the O_2 seeded in helium beam was run at r latively low R.F. power levels and at a relatively high molecular oxygen concentration in order to minimize the exci ed state $O(^1D_2)$ content of the beam.[18] Molecular dissociation was about 55% under these operating conditions. The low energy atomic oxygen beam was generated by discharging a 10% O_2 in argon gas mixture at 250 torr total pressure by 195 watts of R.F. power. The relatively slow atomic oxygen beam produced in this manner had a measured peak velocity of 1.13 x 10^5 cm/sec and a Mach number of 3.9, whi h corresponds to a FWHM velocity spread of 41%. The molecular oxygen was 80% dissociated under the operating conditions described above for the 10% O_2-Ar gas mixture, and was free of any $O(^1D_2)$ content as determined by

titration with a crossed beam of molecular hydrogen.[18]   The

oxygen-rare gas pressures were controlled by a vacuum regulator

in these studies to ensure stable beam source operation at

pressures below one atmosphere. A 5000 V/cm ion deflecting

field was placed prior to the interaction zone of the

scattering chamber in order to eliminate any interference

from ions present in the atomic beam. For both the high

and low energy experiments the oxygen beam was collimated

to an angular divergence of 2.2° by two collimating ele-

ments placed after the source skimmer.

    The benzene beam was run neat for these experiments

at its room temperature vapor pressure of about 90 torr.

The benzene reservoir was immersed in an oil bath in

order to eliminate any rapid temperature fluctuations

due to air currents present in the laboratory. The entire

glass line leading from the benzene reservoir to the beam

source was heated to at least 10K above the bath temperature

in order to prevent condensation of benzene in the gas line.

The nozzle tube and tip were heated to 326K, as determined

by chromel-alumel thermocouples, again in order to prevent

condensation from occurring and to eliminate any benzene

dimers or higher polymers from being present in the terminal

beam. (A pure, slightly heated benzene beam was decided

upon when preliminary testing of a 300 torr, saturated

benzene-argon beam produced extensive dimer formation. See
also Ref. 19 for further information about this dimerization
phenomena.) The benzene beam produced in this manner was
found to have a peak velocity of 5.18×10^4 cm/sec and a
Mach number of 5.8, which corresponds to a FWHM velocity
spread of 33%. Perdeuterated benzene, C_6D_6, obtained from
Aldrich Chemical Company with 99.5 atom percent deuterium
content, was also run as described for benzene, and had a
peak velocity of 5.14×10^4 cm/sec and a Mach number of
4.9 (36% FWHM).

Initially th most probable collision energies for
both the $O + C_6H_6$ and $O + C_6D_6$ systems were 6.5 kcal/mole
(O_2 seeded in helium) and 2.5 kcal/mole (O_2 seeded in argon).
The angular distributions shown in the next section were
taken at these energies. In subsequent experiments slightly
different beam conditions were employed ($\overline{v}_o = 2.25 \times 10^5$
cm/sec, $\overline{v}_{C_6H_6} = 5.30 \times 10^4$ cm/sec, and $\overline{v}_{C_6D_6} = 5.25 \times 10^4$
cm/sec) which resulted in somewhat higher mean collision
energies than those described above: 8.5 kcal/mole for
$O + C_6H_6$ and 8.6 kcal/mole for $O + C_6D_6$. The time-of-flight
distributions presented later in this paper were recorded
for collisions at thes higher energies.

Laboratory angular distributions were obtained by
taking several scans of 60 second counts at each angle, with

time normalization employed when warranted. The supersonic

oxygen beam was modulated at 150 Hz with a tuning fork

chopper and the number density data at each angle was

obtained by subtracting the chopper-closed count from the

chopper-open count. Product counting rates at the center-

of-mass angle for m/e = 65, the predominant mass peak for

the C_6H_6 reaction, were typically 300 cts/sec and 80 cts/sec

for the high and low energy experiments, respectively. The

m/e = 70 signal for the C_6D_6 reaction was similarly found

to be 550 cts/sec and 50 cts/sec for the high and low

energy deuterated experiments. The larger counting rates

for the high energy experiments are mainly due to the higher

intensity of the fast oxygen beam relative to the slow

oxygen beam. Velocity analysis of the various beams was

done with conventional "single shot" time-of-flight

techniques. Product time-of-flight distributions were

obtained using cross-correlation time-of-flight tech-

niques[20,21] with a 255-bit pseudorandom sequence operated

with a 12 μsec dwell time per channel. Counting times

varied considerably depending upon the laboratory angle

and product mass under investigation, with accumulation

times of 30 minutes being representative.

RESULTS

Two distinct reaction channels were observed in this study:

$$O(^3P_J) + C_6H_6 \longrightarrow C_6H_5O + H \qquad \Delta H^\circ_{298} = -15.9 \text{ kcal/mole} \quad (1)$$

$$O(^3P_J) + C_6H_6 \longrightarrow C_6H_5OH \qquad \Delta H^\circ_{298} = -102.4 \text{ kcal/mole} \quad (2)$$
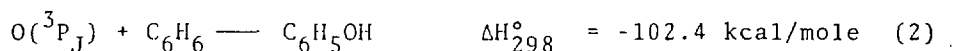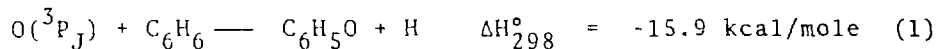
with the first channel corresponding to hydrogen elimination and the other to simple oxygen addition, presumably leading ultimately to phenol formation. No direct evidence for CO elimination from the collision complex was found:

$$O(^3P_J) + C_6H_6 \longrightarrow C_5H_6 + CO \qquad \Delta H^\circ_{298} = -73.8 \text{ kcal/mole} \quad (3)$$

where the reaction exoergicity was calculated assuming, for illustrative purposes only, that cyclopentadiene was the C_5H_6 fragment. Similarly, no OH product was detected in these experiments indicating that the hydrogen abstraction channel was closed:

$$O(^3P_J) + C_6H_6 \longrightarrow C_6H_5 + OH \qquad \Delta H^\circ_{298} = +8.4 \text{ kcal/mole} \quad (4)$$
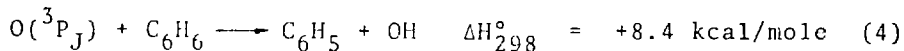
The absence of OH product is not suprising as the mean collision energies used were insufficient for endothermic abstraction to occur. The atomic oxygen reaction with predeuterated benzene was found to have the same open product channels as above, although the branching ratio between channels (1) and (2), at a given collision energy, differed significantly from the C_6H_6 reaction.

Figures 1 and 2 show the angular distributions obtained for the high collision energy studies of the $O + C_6H_6$ and $O + C_6D_6$ reactions. The highly excited primary reaction products coming from channels (1) and (2), corresponding to hydrogen elimination (mass 93) and formation of a long-lived collision adduct (mass 94), fragment in the electron bombardment ionizer of our mass spectrometer detector to give $C_5H_5^+$ (m/e = 65 and $C_5H_6^+$ (m/e = 66) due to CO elimination from the parent species during ionization. These daughter fragment ions were the major fragment ions observed for all species, and were used for monitoring both the angular and velocity distributions of the parent molecules. The daughter ions corresponding to CO elimination from C_6D_5O and C_6D_5OH, respectively, $C_5D_5^+$ (m/e = 70) and $C_5D_6^+$ (m/e = 72), were also the major fragment ions of the perdeuterated benzene reaction. The parent ions at masses 94 and 93 for C_6H_6 and masses 100 and 98 for C_6D_6 were also directly observed, but

were of much lower intensity than their respective daughter
ions. This can be clearly seen in Table I. The narrow
angular distributions shown in Figs. 1 and 2 peak around
their center-of-mass directions. Masses 66 and 72,
corresponding to the addition channel products, have FWHM
angular spreads of 14° and 13°. These distributions can
be virtually reproduced by convoluting the finite velocity
and angular spreads of the reactant beams with the resolution
parameters of the detector. This indicates that the addition
channel angular distributions follow the laboratory centroid
distributions of the two reactive systems, demonstrating
that the ions at masses 66 and 72 are predominantly daughter
ions from the addition products C_6H_6O and C_6D_6O. The
angular distributions of masses 65 and 70, having FWHM
angular spreads of 19° and 15°, are both wider than those
discussed above due to hydrogen or deuterium elimination
from the collision complex. These differences in angular
distribution widths between masses 65 and 66, and masses
70 and 72, rule out the possibility that the fragment
ions having m/e = 65 and 70 arise entirely from fragmenta-
tion of the same parent species as masses 66 and 72. This
provides definitive proof that at a mean collision energy
of 6.5 kcal/mole hydrogen elimination constitutes one of
the two major open channels for the reaction of ground

state atomic oxygen with benzene. The narrow spread of
the mass 65 and 70 angular distributions also precludes
their formation *via* elimination of the relatively massive
CO molecule from the collision complex as conservation
of linear momentum would result in a much broader distri-
bution. In subsequent high energy experiments the mass
93 and 98 parent ion angular distributions were obtained,
and were found to be in good agreement with the mass 65
and 70 distributions. This provides further support for
the hydrogen elimination channel.

The product angular distributions of the low energy
collision experiments are shown in Figs. 3 and 4. These
distributions, as has already been seen for the high
energy data, peak along their center-of-mass directions.
The mass 65 and 66 curves of Fig. 3 are superimposable
within the uncertainty of the measurements (the error bars
in Figs. 1-4 correspond to 95% confidence limits). This
is very interesting and will be discussed later in this
section. The low energy mass 70 distribution is qualita-
tively similar to the $O + C_6H_6$ results. An accurate
angular scan of mass 72 could not be obtained here due to
the presence of a slight mass 72 impurity in the secondary
(perdeuterobenzene) beam. Elastic scattering of this
impurity greatly perturbed the wide angle shape of the

reactive distribution. This impurity was also present during the high energy $O + C_6D_6$ experiments, but was of little concern since the high energy mass 72 reactive signal was much larger than the elastic signal. The high energy mass 72 reactive signal was in fact more than 50 times larger than the low reactive signal (580 counts/sec versus 10 counts/sec) due in part to differences in intensity of the oxygen beam.

Chronologically, it was decided to study the $O + C_6D_6$ system only after hydrogen elimination was observed to be a major reactive channel in the $O + C_6H_6$ system, as shown in Fig. 1. The hope here was that D atom elimination would further broaden the elimination channel's angular distribution, and thereby accentuate the dynamics of this process due to its heavier mass relative to atomic hydrogen. However, as seen in Fig. 2, this was not the case. The 2° FWHM angular width difference between the mass 70 and 72 distributions was actually less than the 4° difference observed for the mass 65 and 66 distributions. This was the first indication that the branching ratio between channels (1) and (2) was isotope dependent and prompted us to examine the relative intensities of the observable parent and daughter ion peaks for the $O + C_6H_6$ and C_6D_6 systems.

In Table I the relative intensities of the detected
ion masses, accurate to within 10%, are presented. These
values represent the relative signal levels for each system
taken at their respective center-of-mass angles. It is
immmediately obvious that the branching ratio between
channels (1) and (2) is dependent upon both collision
energy and isotopic substitution. If we assume that
mass 94 (100) fragments in the electron bombardment
ionizer to give roughly equal amounts of masses 66 (72)
and 65 (70) while mass 93 (98) fragments to yield pre-
dominantly mass 65 (70), then the results shown in
Figs. 1, 2, and 3 and Table I form a consistent picture
of the $O + C_6H_6$ (C_6D_6) reaction. The above fragmentation
scheme implies that the observed signal at m/e = 65 (70)
is a composite of both the addition and elimination
channels. For reaction conditions which do not strongly
favor channel (1) (elimination) over channel (2) (addition)
this in turn implies that the measured daughter ion distri-
butions should be quite similar, with the mass 65 (70)
angular distribution appearing *narrowed* due to its contri-
bution from mass 94 (100). This explains the unexpected
narrow width of the mass 70 angular distribution shown in
Fig. 2 since the high energy $O + C_6D_6$ system does in fact
have a large relative amount of the addition product (as

demonstrated by the large daughter ion intensity at m/e =
72). From Table I we can conclude that, for a given
collision energy, there is more of the addition product
formed in the C_6D_6 reaction relative to the C_6H_6 reaction,
and that increasing collision energy tends to favor the

addition channel over the elimination channel. The assumed
branching ratio for mass 94 fragmentation in the above
argument is based on the observed fragmentation pattern
of ground state phenol.[22] The proposed fragmentation of
mass 93 to yield predominantly m/e = 65 is based on the
relative improbability of losing a mass 27 particle versus
a mass 28 particle (CO) during ionization.

The opposite of the above argument occurs only when
the elimination channel is *very* strongly favored with
respect to the addition (phenol forming) channel. In this
case the m/e = 66 (72) daughter peak actually begins to
reflect the mass 93 (98) distribution due to the small
but finite fragmentation ratio of m/e = 66 (72) to m/e =
65 (70) for the elimination product. (For example,
examination of the cracking pattern for ground state phenol
indicates that m/e = 67 to m/e = 66 ratio is about 0.075.[22])
Carbon-13 containing fragments also become important in
the limit of low phenol production. The low energy

$O + C_6H_6$ data presented in Table I and Fig. 3 is consistent with this description. The mass 65 and 66 angular distributions at 2.5 kcal/mole collision energy were virtually superimposable within the uncertainty of the experiment, and the large (>10:1) $m/e = 65$ to $m/e = 66$ ratio indicates that the primary elementary reaction product was mass 93 (98). These conclusions, taken with those in the preceeding paragraph, indicate that the relative intensities shown in Table I do not represent the actual branching ratios for this reaction as the daughter ion signals contain contributions from fragmentation of both the addition and elimination reaction products.

Understanding the energy dependence of the product branching ratio is, at the present time, further complicated by the known presence of $O(^1D_2)$ in the high energy (helium seeded) oxygen beam. Thus, some product from the reaction $O(^1D_2) + C_6H_6$ (C_6D_6) may be contributing to the high collision energy results. Work is currently in progress in an attempt to gauge the relative contribution of this alternative reaction pathway.

Recently, we have also carried out velocity analysis of the major observable ion peaks for high energy $O + C_6H_6$ (8.5 kcal/mole) and $O + C_6D_6$ (8.6 kcal/mole) collisions. These results provide what we believe to be compelling

evidence for the presence of the hydrogen elimination
channel and for the low probability of CO elimination at
relatively high collision energies. These results support
our earlier conclusions. Figure 5 presents the cross-
correlation time-of-flight (TOF) data for the O + C_6H_6
system taken 1° from its most probable center of mass
angle. The spectra shown for m/e = 93, 66, and 65 have
all been corrected for their respective ion flight times.
Three major conclusions can be inferred from this figure.
First, note that the mass 93 (parent mass of the elimiantion
channel) and mass 65 (daughter ion from mass 93) spectra
agree very closely, especially at higher velocities. These
two data sets are also wider than the mass 66 spectrum,
indicating the influence of hydrogen elimination. There-
fore, the parent-daughter relationship of m/e = 93 and 65
is clearly established. Next, the peak of the m/e = 66
distribution peaks at the most probable center-of-mass
velocity (5.83×10^4 cm/sec) for this collision system,
confirming the assumption that the m/e = 66 signal is due
to fragmentation of the mass 94 adduct. Finally, the
absence of any high velocity peaks in the m/e = 66 and 65
spectra (with the possible exception of a very minor
contribution at channel 10) indicates the low probability
of the CO elimination channel. The Newton diagram dis-
played above these spectra helps to clarify this point.

The larger velocity circle represents the expected mass 66
velocity circle assuming that 10% of the available energy
(collision energy plus exoergicity) from the CO elimina-
tion channel goes to product translation. If CO elimina-
tion were a significant product channel a peak in the
m/e = 66 and 65 (m/e = 65 would be expected from fragmenta-
tion of mass 66 in the ionizer) TOF spectra would be
expected around channel 12. No such peak is observed,
indicating the low probability of the CO elimination
channel. The smaller circle in this Newton diagram repre-
sents the limit of expected mass 93 velocity spread about
the most probable center-of-mass velocity, assuming 100%
of the available energy for the hydrogen elimination pro-
cess goes to product translation. Good agreement is found
between the predicted velocity spread and the observed
width of the TOF spectra. (Of course most of the observed
broadening is due to the finite velocity width of the two
reactant beams, with some additional broadening coming
from recoil of the products having much less than 100% of
the available energy going to translation).

The TOF results for the $O + C_6D_6$ system are shown in
Fig. 6. At the center-of-mass angle (50°) the m/e = 98,
72, and 70 distributions are seen to peak near channel 25,
which corresponds to this system's most probable center-of-
mass velocity, ca. 5.7×10^4 cm/sec. As in the $O + C_6H_6$

reaction, the addition channel daughter ion at m/e = 72 is
narrower than the elimination channel daughter ion at m/e =
70. The parent mass of the elimination channel was also
recorded, and is seen to follow the daughter distribution
within the uncertainty of the measurement. The absence
of any high energy peaks once again indicates that CO
· elimination is a low probability event. Angle dependent
data, shown for Θ = 42° and 62° was also taken in order to
clearly demonstrate the different origins of the m/e =
72 and 70 signals. At 42° the larger width of the m/e =
70 spectrum relative to the m/e = 72 spectrum is obvious,
with this increased width due to deuterium elimination.
The overall shift of these two curves to lower velocities
relative to the Θ = 50° spectra occurs since the distri-
bution of LAB center-of-mass velocity vectors are not
orthogonal to the distribution of relative velocity vectors,
i.e., 90° in the Center-of-Mass reference frame is not
coaxial with the most probable LAB center-of-mass angle.
Furthermore, at 42° the apparent shift to higher velocities
of the m/e = 70 spectra relative to the m/e = 72 spectra
is due to the LAB to Center-of-Mass transformation. At
Θ = 62° the two curves are again separated in time space,
with their shifts relative to the Θ = 50° spectra, and with

respect to each other, explainable as above. The low
velocity tail of the m/e = 72 spectrum at this angle can
be attributed to a contaminant effusing from the
differential pumping region of the perdeuterobenzene
beam.

DISCUSSION

Under single collision conditions the $O(^3P)$ + benzene
reactions has been observed to proceed by two distinct
elementary reaction pathways. These correspond to the
addition of atomic oxygen to benzene to form a long-lived
collision adduct, presumably phenol, and to the substitu-
tion of atomic oxygen for a hydrogen atom, i.e., hydrogen
elimination. The branching ratio between these two channels
has been found to be both isotope and energy dependent,
with the addition channel being favored with respect to
elimination for increasing collision energy and deuterium
substitution. These results represent the first unambiguous
determination of the elementary reaction products which are
formed in this reaction. Our ability to measure both the
angular and velocity distributions of the parent and
daughter ion species was essential for unraveling the
complex reaction mechanism of this system.

A schematic energy level diagram picturing the important reaction pathways is shown in Fig. 7. The zero of energy in this figure was taken as the heat of formation of the reactants. The ground state of phenol, as well as the CO, OH, and H atom product channels were all located with respect to ground state reactants by their heats of formation.[23,24] A recent value for the heat of formation of the phenoxy radical was used in fixing the hydrogen elimination energy level.[25] The triplet biradical energy level of phenol was fixed relative to ground state singlet phenol by the experimentally determined singlet-triplet transition energy observed by Lewis and Kasha,[26] which is in good agreement with the splitting calculated by Dewar and Trinajstic.[27] The ground vibrational level of triplet phenol is stable by ca. 21 kcal/mole with respect to reactants. The first excited singlet state of phenol, S_1, has not been shown in this figure, but is known to fall about 105.8 kcal/mole above S_0, the ground singlet state of phenol.[28,29] This experimentally determined S_1-S_0 splitting is in fair agreement with that calculated by Dewar and Trinojstic.[27] The two dashed curves represent energy barriers of unknown magnitude corresponding to the energy needed to access the spin-forbidden triplet-singlet

transition, and the barrier to decomposition of singlet phenol to form CO and C_5H_6 (which is represented as cyclopentadiene in the figure). The pyrolysis studies of Cypres and Bettens[30] indicate that the CO and C_5H_6 do in fact correlate with phenol in its singlet ground state. The two most probable collision energies at which we have studied this reaction are indicated by E_1 and E_2 in Fig. 7. Finally, the entrance barrier of the $O(^3P)$ + benzene reaction has not been drawn explicitly, but is known to be present due to the ca. 4 kcal/mole activation energy of this reaction.[12] With this energy level diagram in mind our conceptualization of the reaction mechanism is now presented.

The initial $O(^3P)$ electrophilic attack on benzene probably forms a triplet biradical adduct whose lifetime is believed to be $\leq$ 1 nsec. This highly energetic reaction intermediate can then decay by a variety of channels: it can chemically decompose back to reactants, eliminate a hydrogen atom, or, via a radiationless transition, cross into the S_0 manifold of phenol. Hydrogen elimination from the triplet biradical is viewed as being a more favorable decay route than oxygen elimination as it is the more exoergic process. The relatively long lifetime

associated with radiative T_1-S_0 phosphorescence precludes
its consideration here as a relevant decay channel. Opening
of the aromatic ring is also not believed to be a major
decay route due to the expected large energy threshold of
this process. Under the conditions of this experiment
hydrogen abstraction is an endoergic process, and is
therefore not a thermodynamically allowed process under
our experimental conditions.

In this study two main reaction channels were actually
observed: hydrogen elimination and C_6H_6O (presumably
phenol) formation. Consequently, we view the next step
of the reaction mechanism as being a competition between
atomic hydrogen elimination from the triplet adduct, and
intersystem crossing to internally excited singlet phenol.
Our calculated statistical lifetime of this excited S_0
phenol is quite long, always >1 msec, in agreement with
our observation that some m/e = 94 (100) product from the
C_6H_6 (C_6D_6) reaction lives long enough to reach our mass
spectrometer. This observation also reinforces our belief
that a large energy barrier must exit for the unimolecular
decomposition of internally excited singlet phenol to form
CO and C_5H_6. This is not unreasonable as breaking of the
aromatic ring probably requires that the complex pass
through a highly energetic critical configuration.

Examination of the relative product intensities shown in Table I indicates that the branching ratio between the hydrogen elimination and intersystem crossing channels is energy dependent. This is seen by the increase in m/e = 66 (72) intensity which reflects the presence of the adduct product, mass 94 (100), relative to that of m/e = 65 (70) which reflects primarily the intensity of the electron product, mass 93 (98), as the collision energy is increased from 2.5 to 6.5 kcal/mole. This observation suggests that the T_1 - S_0 surface crossing probability increases with increasing energy in the regime 23.5 to 27.5 kcal/mole above the minimum energy configuration of T_1. Sloane[15] has performed a crude SCF calculation which fixes a T_1 - S_0 crossing point at ca. 38 kcal/mole above the minimum energy configuration of T_1. Although this was not a "chemically accurate" value it bears out the possibility of an energy dependent branching ratio. Also, a small energy barrier may be present in the T_1 energy surface for the geometrical rearrangement of the initially formed triplet adduct (O and H bound to the same carbon atom) to one in which the H atom is bound to the oxygen atom (phenol-like configuration). The Franck-Condon overlap integrals for the nonradiative T_1 - S_0 transition are probably larger for the "phenol-like" triplet configuration.

The near total absence of phenol product in our low energy
$O + C_6H_6$ experiment (as indicated by the low relative
intensity of m/e = 66, with some of this due in fact to
^{13}C containing C_6H_6) may also indicate the presence of the
implied energy threshold needed to access the T_1-S_0 surface
crossing.

Also in question is the actual distribution of total
energies present in the reaction intermediate. Several
kinetic studies have confirmed the existence of a 4
kcal/mole Arrhenius activation energy in the reaction of
$O(^3P)$ with benzene.[12] This implies that a small entrance
channel barrier is present in the triplet surface. Thus,
although the most probable collision energies are 2.5 and
6.5 kcal/mole, the most probable excitations of the triplet
adduct may be greater than these collision energies indi-
cate. This is certainly true for Sloane's[15] crossed
effusive beam study as his most probable collision energy
was only 0.61 kcal/mole. Apparently collisions involving
molecules in the high energy tails of his Maxwellian
disributions were the ones leading to reaction.

As mentioned above, the relative intensity data pre-
sented in Table I also indicates that the branching ratio
between hydrogen elimination and intersystem crossing is
isotope dependent. This is expected as both the rate of

hydrogen atom elimination and that of the radiationless T_1-S_0 transition are isotope dependent. The elimination channel is sensitive to the "primary isotope effect",[31] which implies that the perdeutero complex will decompose at a slower rate than the perhydro rate. This is primarily due to the higher state density of the deuterated reactant and to the higher critical energy of the deuterated transition state due to the substantially lower zero-point energy of the deuterated reactant relative to the values for the hydrogenated species. The above isotope effect implies that, for a given collision energy, the elimination/intersystem crossing branching ratio should decrease upon deuteration if the intersystem crossing rate depends weakly on isotopic substitution, as is seen in Table I, due to the slower rate of decomposition of the perdeuterated triplet adduct.

Actually, deuteration should also decrease the rate of the spin-forbidden T_1-S_0 nonradiative transition. This is a consequence of Siebrand's[32-36] "energy gap law" which states that the radiationless transition rate is an exponentially decreasing function of the energy gap. Deuteration increases the dimensionless energy gap $\Delta E_{TS}/\hbar\omega_a$ where ω_a is the frequency of the accepting mode (CH or CD stretch). The dominant factor in the above is the decrease in the Franck-Condon factor which connects

the initial (triplet donor) and final (singlet acceptor) states. This is due to the strongly decreasing vibrational overlap of these states with increasing vibrational quantum number of the accepting mode. Hence deuteration, which effectively increases the quantum number of the accepting mode due to its lower zero point energy, clearly decreases the nonradiative transition rate. This discussion indicates that the elimination/ intersystem crossing branching ratio should increase upon deuteration due to the slower nonradiative decay rate of the triplet adduct. The experimentally observed trend shown in Table I changes in the opposite direction from this, possibly indicating that the primary isotope effect may be more important in governing the decay characteristics of the triplet reaction intermediate. However, the possible presence of products due to $O(^1D_2)$ (which is known to be present in the high energy oxygen beam) does not allow quantitative analysis of the branching ratio data to be made at this time. Uncertainties about the fragmentation patterns of the parent species further complicate attempts to quantify the degree to which collision energy and isotopic substitution influence the product branching ratio. Finally, in the above conceptualization of the overall reaction mechanism, opening

of the aromatic ring and the possible influence of other
low lying electronic states (S_1 and T_2) were neglected
as the information content of the present data neither
suggest no warrant their consideration.

Earlier studies of the $O(^3P)$ + benzene reaction had
reported that CO elimination was an important reaction
pathway.[4,15] Our results indicate that CO elimination,
if it is occurring at all, is a relatively minor product
channel. The absence of any high energy peaks in the
product time-of-flight spectra shown in Figs. 5 and 6,
as discussed in detail in the preceeding section of this
paper, provides strong support for the relative unimpor-
tance of the CO elimination channel for high energy
($\geq$ 6 kcal/mole) collisions. The angular distributions
shown in Figs. 1 and 2 also support our view as they
have shown, in a very direct manner, that the m/e = 66 (72)
signal is overwhelmingly due to fragmentation of highly
excited mass 94 (100) reaction product in our electron
bombardment ionizer. However, it should be clearly stated
that if CO elimination were occurring the resulting
mass 66 (72) product would be harder to detect in our
experiment as it would have a much higher velocity, and
would be spread over a much larger solid angle, than that
arising from fragmentation of mass 94 (100). Time-of-

flight analysis of the reaction products coming from
low energy $O(^3P)$ + C_6H_6 (C_6D_6) collisions must also be
carried out in order to determine whether CO elimination
is an open channel under those conditions. As Boocock
and Cvetanović's experiment[4] was carried out under "multiple
collision conditions" secondary reactions involving $O(^3P)$
atoms and radical products might be the source of their
observed CO. More importantly, Sloane[15] also postulated
that CO elimination was a primary reaction channel. This
was based on his observation of a strong m/e = 66 signal
in his crossed effusive beam experiment, which employed a
fixed (non-rotatable) electron bombardment ionizer-quad-
rupole mass spectrometer detector. On the basis of the
appearance potentials observed for $C_5H_6^+$ (minor threshold
at ca. 9.0 eV and major product threshold at ca. 9.6 eV)
he proposed that cyclopentadiene was a minor product
and that 3-pentene-1-yne was a major product coinciding
with CO elimination. Our study has unambiguously shown
that the strong m/e = 66 peak can predominantly be associated
with fragmentation of highly excited mass 94 adduct during
electron bombardment ionization. As the mass 94 adduct
produced in the $O(^3P)$ + benzene reaction has > 102.4
kcal/mole of internal excitation relative to ground state
phenol it is not surprising that the appearance potential

for $C_5H_6^+$ production is shifted to a lower value than that found for internally cool phenol. Although Sloane discussed the above probability[15] he ultimately concluded that CO elimination was a major reaction pathway. This conclusion is contraindicated by the results of our experiment.

The presence of viscous, polymeric reaction products[4,8] in gas phase studies suggests the presence of radical reaction products. Our observation that the phenoxy radical (H atom elimination is a major reaction product, especially at low collision energies, supports this contention. The results of Mani and Sauer[6] and Bonanno et al.[8] strongly suggest that under multiple collision conditions the reaction proceeds with a slow (rate determining initial attack of $O(^3P)$ on benzene, followed by subsequent radical-radical reactions which lead ultimately to polymeric products. The discrepancy between the rate constants determined by Atkinson and Pitts[10] and Colussi et al.[4] may be due to $O(^3P)$ consumption in the former study by reaction with radicals formed in the initial $O(^3P)$ + benzene reaction. Spectroscopic examination of the polymeric residue using IR absorption and NMR suggests the presence of -OH, C-O-C, and -CHO functional groups.[8] Mass spectrometric analysis of the polymeric residue yields many mass peaks, with m/e = 185 being the highest value observed.[8]

We think it is possible that sequential attack of phenoxy radicals on benzene, and subsequently on the more reactive benzene-phenoxy reaction products, could produce a long-chain polymer, which, upon ionization, would yield mass 185 as a peak. This fragment might be an ether-like substance: $(C_6H_5-O-C_6H_4-O)^+$, m/e = 185. Although this is speculation, it seems plausible as either linkages have been inferred from IR spectra, phenoxy radicals are known to be present from this study, and m/e = 185 was observed in the mass spectrum reported by Bonanno et al.

CONCLUSION

The reaction of $O(^3P)$ with benzene has been shown to initially proceed by the addition of atomic oxygen to benzene, presumably forming a triplet biradical intermediate, which subsequently decays *via* either hydrogen elimination or nonradiative transition to the S_0 manifold of phenol. The branching ratio between these two reaction channels has been found to be both isotope and energy dependent, with the addition channel being favored with respect to elimination for increasing collision energy and deuterium substitution. Our results unambiguously confirm that oxygen addition and hydrogen elimination are *the major open* reaction channels while CO elimination, if occurring at all, is a relatively minor reaction

pathway. This study illustrates that crossed molecular
beam experiments employing both product velocity and
angular distribution analysis using mass spectrometric
particle detection are extremely well suited for unravel-
ing the complex reaction mechanisms of gas phase radical
reactions. This is due to the dynamic and energetic
constraints which are imposed on the reactive roducts
produced in a bimolecular reactive collision. Future
studies using our supersonic atomic oxygen b am source
will include reactions with aliphatic, olef nic, and
other aromatic hydrocarbons in order to ar iv at a more
complete understanding of atomic oxygen-h drocarbon
reactions.

REFERENCES

1.   J. R. Kanofsky and D. Gutman, Chem. Phys. Lett. 15,
      236 (1972).

2.   J. R. Kanofsky, D. Lucas, F. Pruss, and D. Gutman,
      J. Phys. Chem. 78, 311 (1974).

3.   J. R. Kanofsky, D. Lucas, and D. Gutman, 14th Intern.
      Symp. Combust. (1973), 285-294, Pittsburgh, PA.

4.   G. Boocock and R. J. Cvetanović, Can J. Chem. 39,
      2436 (1961).

5.   E. Grovenstein, Jr. and A. J. Mosher, J. Amer. Chem.
      Soc. 92, 3810 (1970).

6.   I. Mani and M. C. Sauer, Jr., Advan. Chem. Ser. 82,
      142 (1968).

7.   L. I. Avramenko, R. V. Kolesnikova, and G. I. Savinova,
      Isvest. Akad. Nauk. SSSR, Ser. Khim. 28 (1965).

8.   R. A. Bonanno, P. Kim, J.-H. Lee, and R. B. Timmons,
      J. Chem. Phys. 57, 1377 (1972).

9.   S. Furuyama and N. Ebara, Intern. J. Chem. Kinetics
      7, 689 (1975).

10.   R. Atkinson and J. N. Pitts, Jr., J. Phys. Chem. 78,
      1780 (1974).

11.   A. J. Colussi, D. L. Singleton, R. S. Irwin, and R. J.
      Cvetanović, J. Phys. Chem. 79, 1900 (1975).

12.   R. Atkinson and J. N. Pitts, Jr., Chem. Phys. Lett.
      63, 485 (1979).

13. J. C. Chu, H. C. Ai, and D. F. Othmer, Ind. Eng.
     Chem. 45, 1266 (1953).

14. R. E. Huie and J. T. Herron, in Progress in Reaction
     Kinetics, K. R. Jennings and R. B. Cundall, Eds.
     (Pergamon, Oxford, 1975) Vol. 8, pp. 60-63.

15. T. M. Sloane, J. Chem. Phys. 67, 2267 (1977).

16. Y. T. Lee, J. D. McDonald, P. R. LeBreton and D. R.
     Herschbach, Rev. Sc . Instrum. 40, 1402 (1969).

17. S. J. Sibener, R. J. Buss and Y. T. Lee, XIth Inter-
     national Symposium on Rarefied Gas Dynamics, Cannes,
     France, 1978, in press.

18. S. J. Sibener, R. J. Buss, and Y. T. Lee, submitted
     to Rev. Sci. Instrum.

19. K. C. Janda, J. C. Hemminger, J. S. Winn, S. E. Novick,
     S. J. Harris, and W. Klemperer, J. Chem. Phys. 63,
     1419 (1975).

20. V. L. Hirschy and J. P. Aldridge, Rev. Sci. Instrum.
     42, 381 (1971).

21. K. Sköld, Nucl. Instrum. Meth. 63, 114 (1968).

22. Atlas of Mass Spectral Data, Vol. 1, E. Stenhagen,
     S. Abrahamsson, and F. W. McLafferty, Eds. (Interscience,
     New York, 1969) p.48.

23. S. W. Benson, Thermochemical Kinetics, Second Ed.
     (John Wiley and Sons, New York, 1976).

24. H. M. Rosenstock, K. Draxl, B. W. Steiner, and J. T. Herron, J. Phys. Chem. Ref. Data 6, Suppl. #1, 1977.

25. A. J. Colussi, F. Zabel, and S. W. Benson, Intern. J. Chem. Kinetics 9, 161 (1977).

26. G. N. Lewis and M. Kasha, J. Amer. Chem. Soc. 66, 2100 (1944).

27. M. J. S. Dewar and N. Trinajstic, J. Chem. Soc. A. 9, 1220 (1971).

28. H. J. Teuber and W. Schmidtke, Chem. Ber. 93, 1257 (1960).

29. H. Zimmerman and N. Joop, Z. Electrochem. 65, 61 (1961).

30. a) R. Cypres and B. Bettens, Tetrahedron 30, 1253 (1974); b) R. Cypres and B. Bettens, Tetrahedron 31, 359 (1975).

31. W. Forst, Theory of Unimolecular Reactions (Academic, New York, 1973) p.350.

32. W. Siebrand, J. Chem. Phys. 44, 4055 (1966).

33. W. Siebrand and D. F. Williams, J. Chem. Phys. 46, 403 (1967).

34. W. Siebrand, J. Chem. Phys. 46, 440 (1967).

35. W. Siebrand, J. Chem. Phys. 47, 2411 (1967).

36. W. Siebrand and D. F. Williams, J. Chem. Phys. 49, 1860 (1968).

Table I. Relative Intensities of the Detected Ion Masses.

	Mass	Species	Collision Energy	
			6.5 kcal/mole	2.5 kcal/mole
O + C_6H_6	94	C_6H_5OH	0.01	< 0.005
	93	C_6H_5O	0.08	0.01
	66	C_5H_6	0.21	0.08
	65	C_5H_5	1.00	1.00
O + C_6D_6	100	C_6D_5OD	0.04	< 0.005
	98	C_6D_5O	0.04	< 0.005
	72	C_5D_6	1.05	0.18
	70	C_5D_5	1.00	1.00

FIGURE CAPTIONS

Fig. 1. Angular distributions from the reaction $O(^3P)$ +
C_6H_6, E_c = 6.5 kcal/mole. The primary reaction
products formed were C_6H_5O and C_6H_5OH, which
subsequently fragmented during electron bombard-
ment ionization.

Fig. 2. Angular distributions from the reaction $O(^3P)$ +
C_6D_6, E_c = 6.5 kcal/mole. The primary reaction
products formed were C_6D_5O and C_6D_5OD, which
subsequently fragmented during electron bombard-
ment ionization.

Fig. 3. Angular distributions from the reaction $O(^3P)$ +
C_6H_6, E_c = 2.5 kcal/mole.

Fig. 4. Angular distribution from the reaction $O(^3P)$ +
C_6D_6 → C_6D_5O + D, E_c = 2.5 kcal/mole. Data
corresponding to the addition channel could not
be obtained due to the presence of an m/e = 72
contaminant in the C_6D_6 beam.

Fig. 5. Product time-of-flight data for the high energy
C_6H_6 reaction. The excellent agreement between
the m/e = 93 and m/e = 65 spectra confirms that
m/e = 65 is a daughter ion of the C_6H_5O reaction
product. The absence of any fast m/e = 66 or 65
signal indicates that CO elimination is a

relatively minor reaction pathway. All spectra
have been corrected for their respective ion
flight time offsets. Newton diagram key:
larger circle indicates expected mass 66 velocity
if 10% of the available energy from the CO
elimination channel goes to product translation;
smaller circle indicates expected mass 93
velocity if 100% of the available energy from
the hydrogen atom elimination channel goes to
product translation.

Fig. 6.   Product time-of-flight data at three laboratory
angles for the high energy C_6D_6 reaction. The
low velocity tail of the m/e = 72 spectrum at
$\Theta = 62°$ is due to effusion of a contaminant from
the C_6D_6 differential pumping region. All spectra
have been corrected for ion flight time offsets.

Fig. 7.   Energy level diagram of the $O(^3P)$ + benzene
reaction. E_1 and E_2 correspond to the two
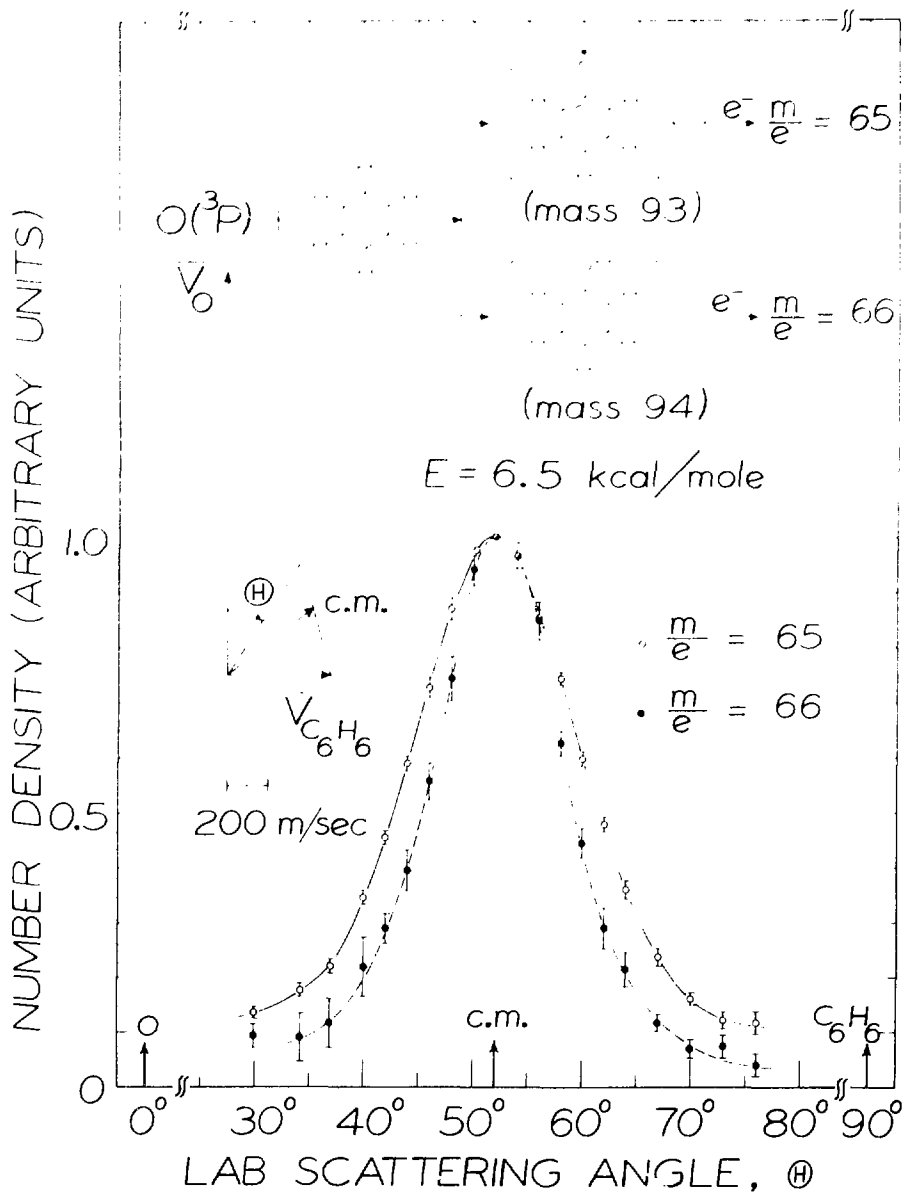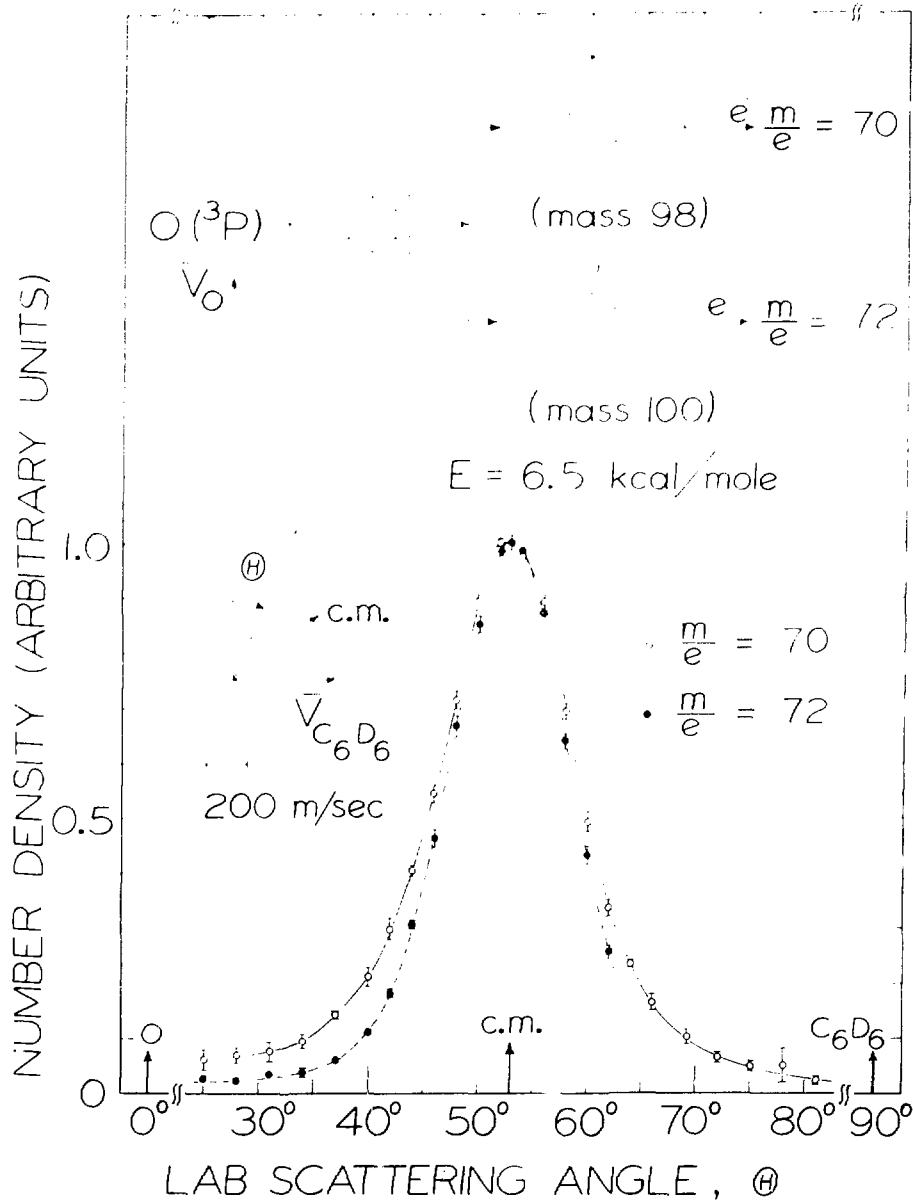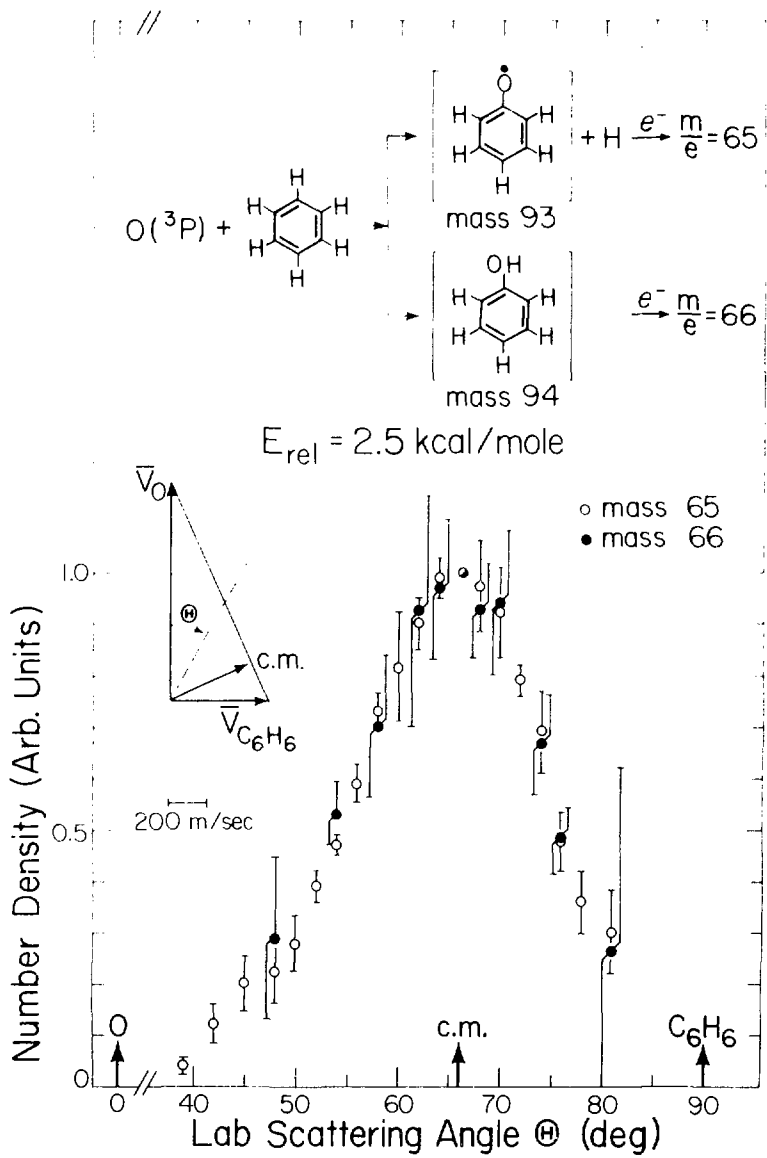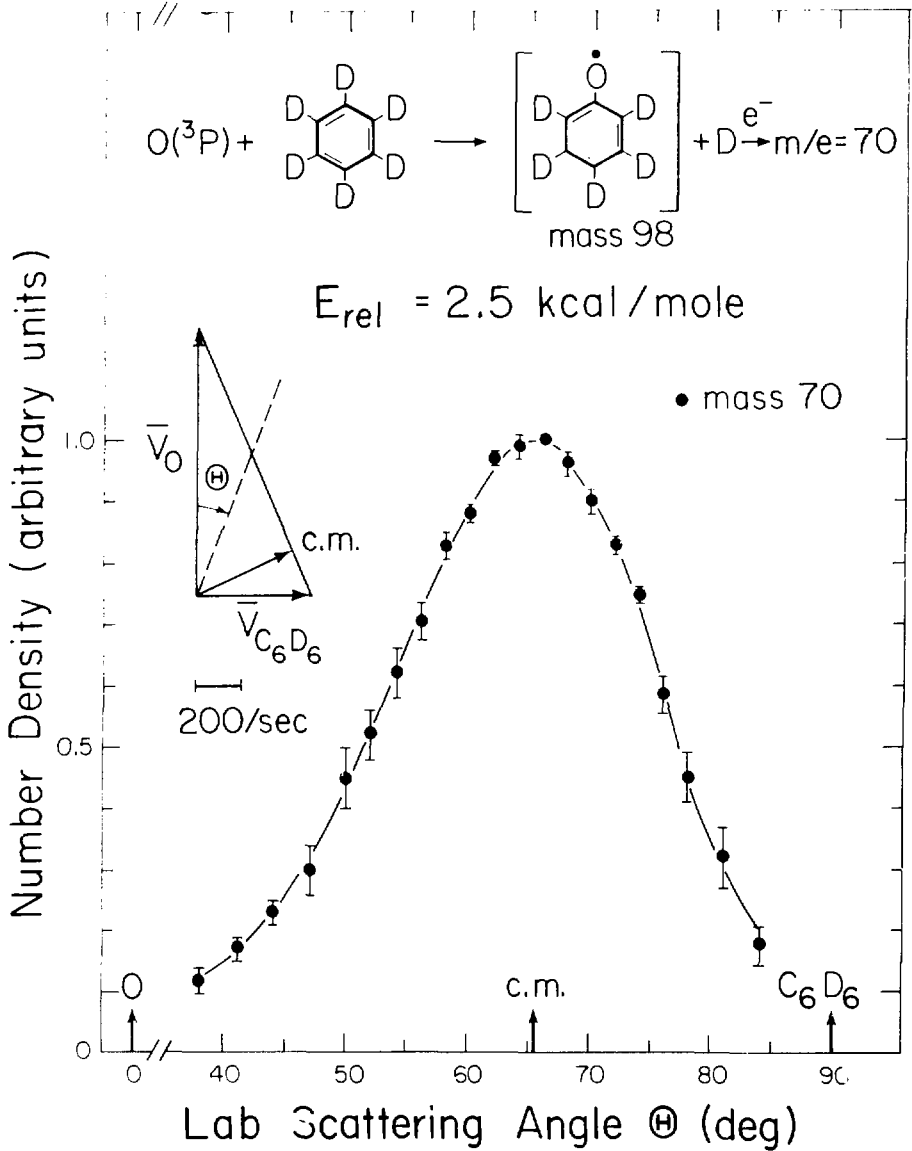collision energies used in this study.

Fig. 1

Fig. 2

$O(^3P) +$ [benzene structure]

$\rightarrow$ [phenoxy radical structure] $+H$ $\xrightarrow{e^-}$ $\frac{m}{e}=65$

mass 93

$\rightarrow$ [phenol structure] $\xrightarrow{e^-}$ $\frac{m}{e}=66$

mass 94

$E_{rel} = 2.5$ kcal/mole

○ mass 65
● mass 66

Fig. 3

XBL 798-2454

Fig. 4

Fig. 5

$O(^3P) + C_6D_6$, $E_{rel} = 8.6$ kcal/mole
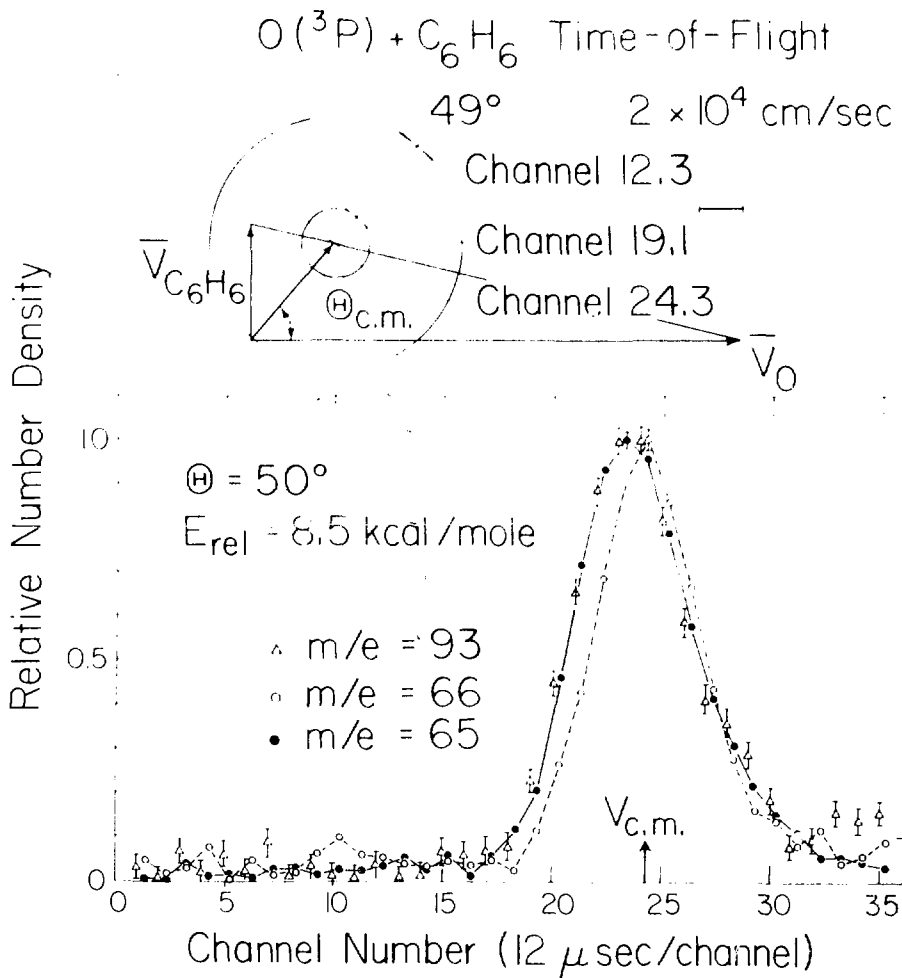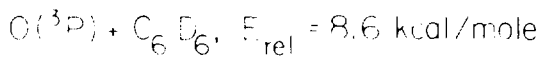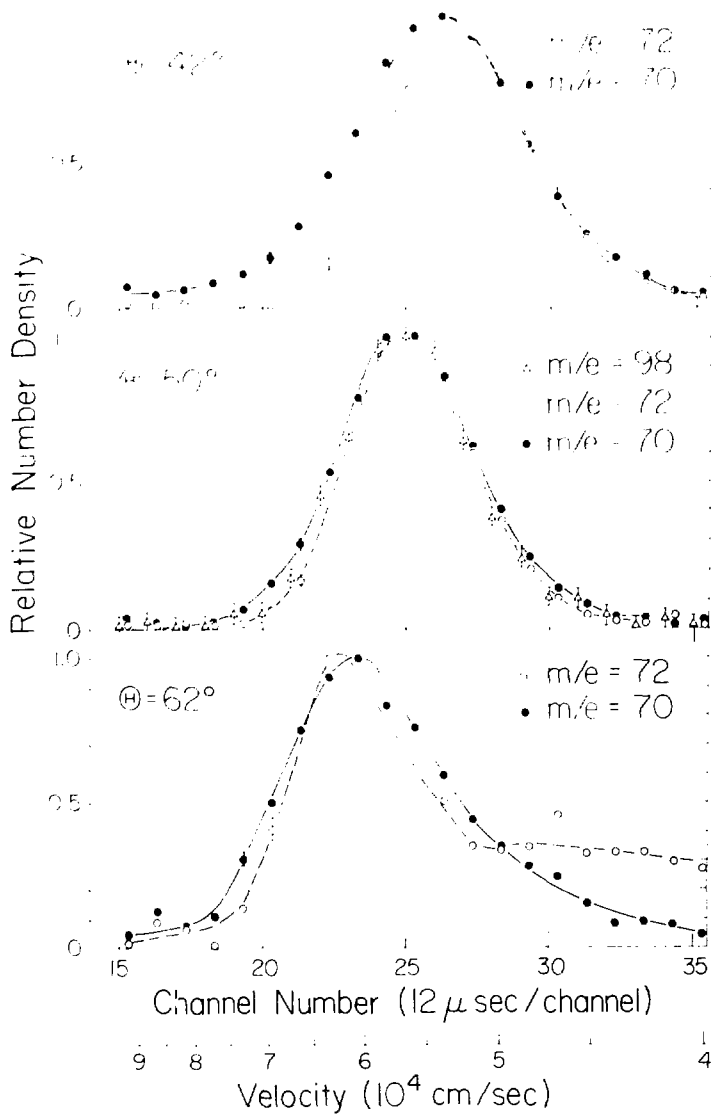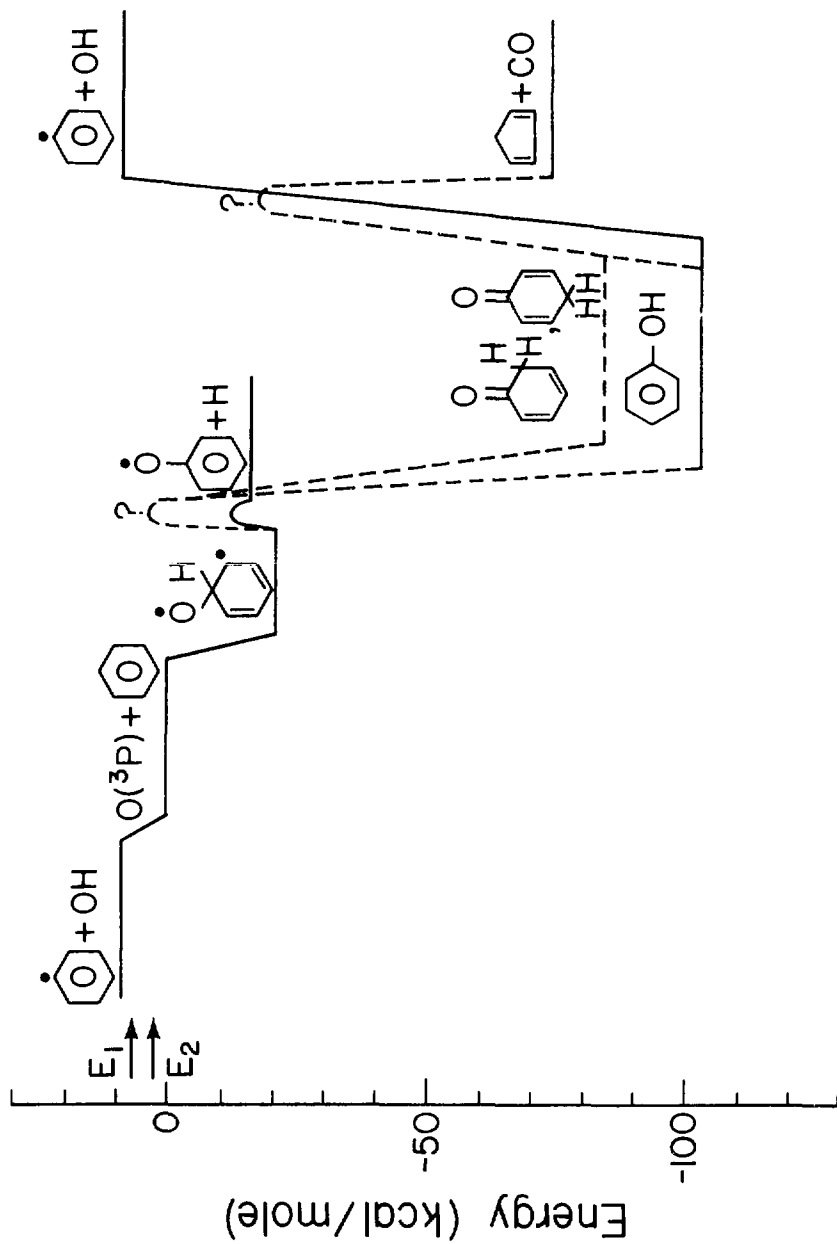
Time – of – Flight

Fig. 6

Fig. 7

XBL 799-2804

V. THE INTERNAL AND TRANSLATIONAL ENERGY
DEPENDENCE OF MOLECULAR
CONDENSATION COEFFICIENTS

INTRODUCTION

Molecular beam surface scattering experiments are
ideally suited for studying many aspects of gas-surface
interactions. Scattered particle angular distributions,
velocity distributions, and, in principle, internal
energy distributions can now be obtained from beam-surface
scattering experiments in which the incident beam (or
beams for reactive studies) is well defined with respect
to its velocity, angular divergence, incident angle, and
possibly internal quantum state. The target surface can
also be well characterized with its temperature, com-
position, and when appropriate, crystallographic plane
serving as experimentally variable parameters. Perhaps
most importantly, these experiments can yield valuable
information on the *initial* interaction between the incident
particle and the target surface since the actual gas-
surface interaction potential is sampled by "single
collision" scattering events. Beam-surface scattering
experiments therefore hold the promise of providing a
very detailed, microscopic picture of gas-surface kinetics,
as crossed molecular beam experiments are already providing
for gas phase studies.

In our laboratory surface scattering techniques are being used to study the process of gaseous condensation. Valuable information on the detailed dynamics and energetics of this process can be obtained in molecular beam scattering experiments which was previously inaccessible in more conventional studies. In particular, we have set out to understand whether, and to what extent, excitation of a polyatomic molecule's internal degrees of freedom (vibration, rotation) can influence its sticking probability upon collision with a cold surface. This question is of current interest for a variety of reasons. In addition to its obvious importance in understanding gas-surface collisional energy transfer mechanisms, it is also of fundamental significance to future heterogeneous laser isotope separation schemes. Furthermore, it is also desirable to understand how both internal and translational energy influence sticking probabilities as the resulting physisorbed molecules are, in many instances, the precursors to chemically important chemisorbed species. In this study molecular beams are therefore being used to investigate the *microscopic* behavior of physical adsorption and gas-surface energy exchange mechanisms, which should enable · to improve our understanding of the *macroscopic*, and p· ·lly important, process of gaseous condensation.

Recently, both theoretical[1-4] and experimental[4-6] investigations of the internal energy dependence of molecular condensation have appeared in the literature. Gochelashvili et al.[1] have suggested that the sticking coefficient, c, for polyatomic molecules should be expressed as $c = 1 - \exp(-E_c/E_{tot})$ where E_c is the critical adsorption energy and E_{tot} represents the total energy of the incident molecule, $E_{tot} = E_{trans} + E_{vib} + E_{rot}$. From this expression they infer that the reflection probability difference between selectively excited molecules and unexcited ones may serve as the basis for heterogeneous laser isotope separation. Their model is obviously a large oversimplification of the energy transfer pathways for this process. Basov et al.[4] have proposed a model which suggests that local heating of the phonons in the immediate region of an adsorption event (due to deposition of E_{tot}) may lead to reevaporation of the adsorbed entity. Again, this is an highly improbable description of the condensation process. Karlov and S.. tan[2] have proposed that the enhanced reflection probability of excited lecules must critically depend on the efficiency of $V \rightarrow T$ energy exchange during the initial collision event. Finally Doll[3] has proposed a simple, phenomenological model to describe internal energy effects

in condensation phenomena which suggests, based upon
adiabaticity arguments, that rotational and low-frequency
vibrational excitations will have a significant influence
on molecular sticking probabilities. All of the above
descriptions, in spite of their simplified nature, do
predict that internal excitation should inhibit conden-
sation. Experimentally, much controversy still exists
over the existence and extent of internal energy effects.
The Russian bulk kinetic experiments with CO_2 and CO
excited in electrical discharges[4] and with laser excited
BCl_3[5] suggest that the effects are significant. However,
the internal energy effect reported in the laser excited
BCl_3 experiment has not been observed in an attempted
reproduction of that experiment.[6]

It has also been suggested, for strongly interacting
chemical systems which have an energy barrier in the exit
valley of their potential energy surface leading to chemi-
sorption, that excitation of a molecule's vibrational modes
should promote its probability of dissociatively chemi-
sorbing upon impact with a catalytic surface. Stewart and
Ehrlich[7] have noted in field emission experiments that
vibrational excitation of CH_4 by thermal heating appears
to promote its dissociative chemisorption on rhodium.
Yates et al.[8] have shown in thermal desorption studies

that laser excitation of the CH_4 v_3 and (indirectly) $2v_4$ and v_4 modes does not significantly promote its chemisorption on Rh(111). Recently Ehrlich and his coworkers[9] have also shown that excitation of the methane v_3 mode to either its first or second excited level does not actively enhance its probability of dissociative chemisorption on evaporated films of rhodium. In another system of chemical interest, Gelb and Cardillo,[10] on the basis of their classical trajectory calculations, have predicted that the probability of H_2 dissociation u on collision with Cu(100) should increase 40-fold when the , is placed in its first vibrationally excited level.

In this paper a series of experiments will be described which have directly confirmed the existence of an internal energy dependence of molecular sticking probabilities for collisions of rotationally and vibrationally excited molecules with a cold surface. This internal energy dependence has been explored as a function of incident translational energy for velocity selected, and thermally excited molecular beams of CCl_4 and SF_6. A preliminary report of the CCl_4 results has been previously reported in the literature.[11] Thermal excitation rather than laser (state-selective) excitation was employed in these studies as the main interest was to establish the

presence, and to gauge the extent, of internal energy effects in the process of gaseous condensation. For relatively large polyatomic molecules, such as SF_6, thermal excitation allows us to "excite" virtually all of the incident molecules. Resonant IR laser excitation would only allow perhaps a few tenths of one percent of the incident beam to be excited due to the relatively large partition function of these molecules (i.e., low population in any particular quantum state). The data presented primarily consists of angular distributions, velocity distributions, and intensity measurements of reflected molecules as functions of incident beam velocity, internal energy, and surface temperature. In addition to the internal and translational energy dependence of sticking probability, results on energy accommodation and non-conservation of tangential momentum are also reported for SF_6 and Kr beams scattering from surfaces composed of their respective condensed (amorphous) ices.

EXPERIMENTAL

Our crossed molecular beams apparatus, which is similar in design to one which has been previously described in detail,[12] was extensively modified for this

experiment by replacing one of the beam sources, and its differential pumping region, with a cryogenically cooled target surface assembly. The initial experiments involving CCl_4 utilized a liquid nitrogen cooled surface which employed gravity fill of the cryogen to ensure effective coolant flow. Surface temperatures as low as ca. 90 K could be easily achieved with this experimental arrangement. Nichrome wire heaters embedded in the copper surface support block permitted operation at temperatures above 90 K. In subsequent studies involving SF_6 and Kr the above was replaced by a more sophisticated surface assembly which was cooled by a CTI Model-21 closed cycle helium refrigerator. Surface temperatures as low as ca. 10 K could be achieved with this cryostat. Stable operation at temperatures above 10 K was achieved with a Lake Shore Cryogenics temperature controller. The underlying target substrate for both systems was fabricated from polycrystalline copper, which was prepared with a chemical polishing procedure similar to that described by Ahearn et al.[13] 2-mercaptobenzothiazole was used as the nitrogen containing additive in our polishing procedure.[13]

The main scattering chamber was pumped by an unbaffled 5300 l/sec diffusion pump using DC-705 oil, and by a liquid nitrogen cooled cold shield which is very effective in pumping condensible gases. The base pressure of the scattering

chamber was ca. 1×10^{-7} torr during the course of these experiments. The copper "substrate" surface was therefore undoubtedly contaminated with many molecular species before the onset of beam condensation. However, at the surface temperatures used for data collection the sticking probability of the incident beam was always $\geq$ 99%, indicating that a relatively "clean" surface, consisting of an amorphous ice of the incident beam gas, was always presented to the incident molecular beam. Without UHV conditions in our main scattering chamber fairly well defined target surfaces were therefore generated *via* constant deposition of a large percentage of the incident beam. The scattered particles analyzed in these experiments were the ~1% (or less) of the incident flux which did not condense upon impact with the cryogenic surface.

Figure 1 is an assembly diagram which outlines the important experimental components. The effusive, heated, and velocity selected beam source constructed for this experiment permits independent variation of T_B and v_B, the beam temperature and beam velocity. This in turn permits the study of gas-surface collisions involving polyatomic molecules having different internal energies (i.e., beam temperatures) but the same translational energies (constant velocity selector frequency). The heated, effusive source

consisted of a 6 mm OD/4 mm ID quartz tube which was
wrapped with 0.5 mm diameter tantalum wire at a turn
density of 2.75 - 3.15 turns/cm. The wire heater extended
from the front tip of the quartz tube to a point ca. 50 cm
back from the tip in order to ensure vibrational and
rotational equilibration of the quickly flowing gas to
the oven temperature. The orifice at the front of the
tube was a slot measuring 0.75 mm x 2.80 mm. A 13 mm
OD/11 mm ID quartz tube, which was wrapped with 4 turns
of 0.0025 cm tantalum foil, was slipped over the inner
(wire wrapped) tube to act as both a radiation shield to
protect the rest of the source from excessive heating,
and to ensure proper heating of the oven by blackbody
radiation. A chromel-alumel thermocouple was attached to
the inner quartz tube, and one was also embedded between
the outer quartz tube and the tantalum radiation shield,
in order to monitor oven temperature. The true oven tem-
perature was actually obtained by fitting the effusive
velocity distributions produced from the source to
Maxwellian distributions as a function of oven power.
Plots of thermocouple voltage versus beam temperature were
then constructed for the two oven thermocouples, resulting
in linear calibration curves. Extreme care was taken to
ensure that Maxwellian distributions were in fact generated

during the above oven calibration tests by running the source at very low stagnation pressures. Krypton and oxygen were used for these calibration runs.

The velocity selector was similar to one which has been previously described.[14] Briefly, it consisted of six 0.1 mm thick aluminum disks, with each disk having 160 slots of 0.081 cm width evenly spaced arounds its circumference. The average radius to the midpoint of the slots was 4.50 cm. The selector had approximately a 20% FWHM $\Delta v/v$ bandpass function and was found experimentally to have a λ conversion factor[15] of about 201 cm, where (λ) x (frequency) = transmitted velocity. The overall length of the velocity selector was 2.74 cm. Absolute determination of the CCl_4 and SF_6 flux distributions transmitted by the velocity selector, as a function of oven temperature and selector frequency, was always carried out with high resolution single-shot time-of-flight (TOF) techniques at a dwell time per channel of 4 μsec. The velocity selector could be operated at frequencies up to ~400 Hz (most probable transmitted velocity ~8 x 10^4 cm/sec) and the source oven temperature could easily be varied between room temperature and ca. 700 K. These T_B and v_B ranges permit the internal energy (E_i) to translational energy (E_t) ratio to varied over a wide range

for polyatomic molecules. For the CCl_4 experiment the oven temperatures used were 298 K and 560 K, and for SF_6 these temperatures were 300 K and 608 K. The CCl_4 beam was run by immersing the CCl_4 reservoir in an ice-water bath, with the resulting vapor passing through a series of needle valves before entering the beam source. Similarly, after the SF_6 was passed through a vacuum regulator its flow was throttled down by a series of needle valves. Beam stability in both experiments was found to be excellent after initial oven transients lasting ~30 minutes were allowed to pass. The desirability of building oven sources having relatively low heat capacities, and hence relatively fast stabilization rates, cannot be overstated. The beams produced by this source were collimated by a series of defining elements to a FWHM angular divergence of ca. 2.2 degrees.

The first and second generation surface assemblies (liquid nitrogen and cryostat cooled, respectively) were extensively wrapped with many layers of "super insulation" (6 micron thick aluminized mylar) in order to minimize heat exchange with the surrounding environment. The surface temperature was continuously monitored with two iron-constantan thermocouples which were referenced to ice-water junctions. The vacuum feedthroughs for these

thermocouples consisted or iron and constantan wires in
order to avoid generating any stray junction potentials.
The first generation assembly was designed so that it
could be rotated out of the beam-line in order to permit
the detector to look directly into the incident beam.
This was believed to be necessary in order to reference
the incident intensity, during the course of an experi-
ment, as a function of oven and velocity selector settings.
However, subsequent measurements of reflected angular and
velocity distributions revealed that beams scattering from
room temperature (dirty) copper surfaces always thermally
accommodated to T_s, the surface temperature, as manifested
by their cosine angular distributions. The surface was
therefore acting as a "beam normalizer" since all incident
beams, regardless of their initial velocity distribution,
scattered with the same Maxwellian velocity distribution.
This permitted us to design a much more precise target
assembly, which did not have to rotate out of the scattering
plane, when the closed-cycle refrigerator was added.
Alignment of the target surface for both setups was done
by reflection of a HeNe laser. Final machining of the
second generation target support was done after experimentally
monitoring the extent of inward deflection of the flange
holding the target upon evacuation of the scattering chamber,
and then monitoring the extent of shrinkage of the assembly

upon cooldown to ca. 100K. This ensured that the surface would fall precisely at the center of rotation of the detector. For all of the experiments described in this paper the incident beam-surface angle, θ_i, was fixed at 50° from the surface normal.

The particle detector used in these studies consisted of a triply-differentially pumped electron bombardment ionizer/quadrupole mass spectrometer.[12] It could rotate about the surface allowing angular distributions and relative number density measurements to be obtained for reflected angles between 30° and 90° with respect to the surface normal. Only in-plane scattering events were detected, with the plane determined by the surface normal and the incident beam. Time-of-flight velocity distributions were obtained by placing a chopping disk in front of the entrance to the detector. Typical chopper to ionizer distances were ca. 18.2 cm. For low signal experiments conducted below the condensation point of the incident beam cross-correlation TOF techniques[15,16] were used, employing a 255-bit, ~50% duty cycle pseudorandom chopping sequence operated at 12 µsec/channel dwell time. During the initial TOF data acquisition runs, involving molecules scattered from cryogenically cooled surfaces, a radiation shield constructed from thin copper and super insulation was placed around the TOF chopping disk. This was done as radiative heating of the target surface from the TOF disk might have been

a possible systematic error in our measurements since the thermocouples were placed on the back surface of the copper substrate. However, TOF measurements made without the radiation shield yielded identical results to those obtained with the shield in place, allowing us to operate without the shield in further experiments.

Angular distributions were obtained by modulating the incident beam with a 150 Hz Bulova tuning fork chopper. The actual signal was obtained by subtracting the chopper-closed count from the chopper-open count. Repeated angular scans were taken for all angular distributions in order to achieve good signal-to-noise ratios. Typical counting times and signal rates will be discussed in the next section of this paper. In the CCl_4 experiment the detected ion was actually CCl_3^+ while for the SF_6 experiment it was SF_5^+. These daughter ions were of much higher intensity than their respective parent ions.

Finally, this series of condensation experiments was performed at $\geq 99\%$ sticking probability so that inelastic scattering events could be clearly distinguished from adsorption events followed by subsequent particle reevaporation (trapped trajectories). This is accomplished by noting that the residence times of adsorbed (trapped) molecules are several orders of magnitude larger than the

gating period, 6.67 msec, while the interaction times of inelastically scattered molecules are typically 10^{-12} sec. Thus, by gating the counting electronics at 150 Hz, as shown in Fig. 1, the inelastically scattered molecules can be distinguished from those having very long residence times. In fact, in the extreme case of $\geq$ 99.9% sticking probability, virtually all of the particles detected were inelastically scattered as the trapped molecules were effectively "frozen out" in the condensate. This is highly desirable as the scattering events carrying the important dynamical information are the inelastically scattered ones. This experiment therefore overcomes one of the main experimental difficulties associated with studying gas-surface collisions, as was briefly discussed by Zwanzig[17] in his paper on gas-surface collisional energy transfer.

RESULTS

Angular distributions have been obtained for CCl_4 and SF_6 as a function of incident velocity, internal energy, and surface temperature. The scattering behavior for these two molecules was found to be quite similar, as demonstrated below. All scattered angular distributions that were

measured above each molecule's respective condensation
temperature were cosine in shape with respect to the sur-
face normal. This, by itself, only indicates that the
copper substrate was microscopically rough and contaminated
(as it was), and that the incident beam was possibly
thermally accommodating to T_s, the surface temperature.
The upper portion of Fig. 2 shows one of the first experi-
mental angular distributions obtained for CCl_4 scattering
from a room temperature (dirty) copper surface. The small
deviations from the solid cosine (θ) curve can be attributed
in this case to slight misalignment of the surface. Sub-
sequent angular distributions obtained for CCl_4, SF_6, and
several rare gases could be well fit with the cosine (θ)
function. In order to resolve the question of possible
thermal accommodation to T_s scattered particle TOF distri-
butions were recorded for several gases as a function of
incident translational energy. The three curves shown in
Fig. 3, for incident SF_6 mean velocities of approximately
2.0×10^4 cm/sec, 3.5×10^4 cm/sec, and 5.0×10^4 cm/sec,
conclusively demonstrate that thermal accommodation to T_s
is in fact essentially complete. The proof for this is
that the three scattered particle velocity distributions,
in spite of their different incident distributions, were
superimposable with each other, and could be fit with a

calculated 300 K Maxwellian flux distribution (dashed lines
in Fig. 2). The deviations at low velocities are an arti-
fact of the experimental TOF measurement, with the low velo-
city cut-off due to the finite width of the TOF chopper disk.
TOF measurements for CCl_4, SF_6, and Kr revealed that thermal
accommodation to the surface temperature continued with
decreasing T_s until each molecule's condensation temperature
was reached. This was very fortunate as it allowed us to
monitor incident beam flux, as a function of velocity
selector setting and oven temperature, by simply making
relative reflected number density measurements as a function
of these parameters at $T_s > T_c$, the condensation temperature
for each molecule. (Since all reflected velocity distribu-
tions were identical, the relative number density measurements
taken with our detector were exactly equivalent to relative
flux determinations.) This alleviated the need to con-
tinually remove the target surface from the beam-line during
the course of the experiment, as was described in the pre-
ceeding section of this paper.

When the surface temperature was dropped below the
CCl_4 condensation temperature, $T_c(CCl_4) \approx 142K$, to $T_s =$
117K a very interesting angular distribution was recorded,
which is shown in the lower portion of Fig. 2. This distri-
bution appears to be a "hybrid", consisting of some mole-
cules which scattered with a cosine (θ) dependence, and

others which scattered in a specular-like manner. As T_S = 117K corresponds to a CCl_4 sticking probability of about 90% (as determined from the counting rate at the specular angle) this view seems plausible. This indicated that still lower surface temperatures would be needed to study inelastic scattering events as the large contribution from trapped molecules (those which had been adsorbed, thermally accommodated, and subsequently reevaporated) still dominated the detected signal.

The angular distributions taken far below the CCl_4 condensation temperature exhibited a marked difference in shape from those discussed above. Figure 4 shows the angular distributions taken with T_S - 90K and T_B (oven temperature) = 298K, while Fig. 5 shows those obtained with T_B = 560K, for several different incident velocities. For CCl_4, T_S = 90K corresponds to a sticking probability of $\geq$ 99.5%, as determined from the counting rate recorded at the specular angle. These distributions have no visible remnant of accommodated (cosine) scattering, and appear to peak 15° superspecularly from the specular angle of 50°. Typically, counting rates for the distibutions shown in Figs. 4 and 5 were 10 counts/sec, taken with a m/e = 117 background of 125 counts/sec. The lack of peak scattering angle variation found in these figures, as a function of

incident velocity, may imply that the CCl_4 molecules experience constant relative momentum loss collisions with the surface. Future TOF studies will allow this interesting feature of the data to be studied more closely.

If we assume, as in a hard cube model,[18] that the tangential momentum of the CCl_4 is conserved during the collision, then we can arrive at *lower bound estimates* of the energy accommodation coefficients, α_E, from the angular distributions shown in Figs. 4 and 5. These estimates can be easily calculated by noting the deviation of the angular distribution peaks from the specular angle. The energy accommodation coefficient is defined as

$$\alpha_E = \frac{E_i - E_r}{E_i - E_s} \tag{1}$$

where E_i is the incident beam translational energy, E_r is the reflected beam translational energy, and E_s is the mean translational energy of a molecule at T_s. Within this simple framework α_E for CCl_4 is found to be ~0.37 for v_i = 2.5 x 10^4 cm/sec and ~0.30 for v_i = 5.0 x 10^4 cm/sec. These values correspond to a 45% relative momentum loss in the momentum component perpendicular to the surface, and a 0% loss in the momentum component tangential to the surface. Again, these α_E values are only crude lower bound

estimates, as tangential momentum loss almost certainly
occurs during the scattering of heavy polyatomic molecules.
The TOF data for SF_6 presented later in this section bears
out this point. However, the overall skewing of the CCl_4
angular distribution with respect to the specular angle,
θ_s = 50°, does indicates that momentum accommodation occurs
to a greater extent in the direction perpendicular to the
surface than tangential to it.

Figure 6 shows the SF_6 angular distributions that
were obtained at T_s = 50K for three different incident
velocities. Typical counting rates at v_j = 3 x 10^4 cm/sec
were 25 counts/sec, with a m/e = 127 background rate of
230 count/sec. Signal rates were substantially higher for
faster incident velocities. This surface temperature
corresponds to ≥ 99.5% sticking probability for SF_6 at
those velocities. Once again, the angular distributions
do not vary very strongly with either incident velocity
or beam temperature. The lack of variation with beam
temperature (internal energy) may indicate a weak coupling
of internal to translational energy. However, due to the
relatively large mass of SF_6 only slight angular shifts
would be expected.

Using cross-correlation TOF techniques the question
of SF_6 energy accommodation was explored in much greater
detail than during the CCl_4 experiment. The data shown

in Fig. 7 represents a series of SF_6 reflected velocity
distributions, taken at the specular angle, as a function
of surface temperature. The dashed lines in each section
of the figure represent the calculated SF_6 Maxwellian
flux distributions at each surface temperature. The
experimental TOF distributions can be fit extremely well
with the Maxwellian distributions for T_s = 280K, 100K, and
80K indicating complete SF_6 thermal accommodation to
T_s. The low velocity deviations, as discussed earlier,
are an artifact of the measurement. However, as the sur-
face temperature was further lowered from 80K to 70K,
50K, and ultimately 20K the experimental velocity distri-
butions became *faster* than the Maxwellian distributions.
This clearly demonstrates that we are in fact analyzing
inelastic events, rather than trapped and reevaporated
ones, for very low T_s values. Note also that the onset
of condesnation for SF_6 was found to occur at $T_c \approx 79K$,
in good agreement with the data shown in this figure.

Important information about momentum exchange and
energy accommodation can be obtained from the TOF distri-
butions shown in Fig. 7. Table I summarizes the data
taken at the specular angle for SF_6 with T_B = 300K.

Table I

SF_6 Energy Accommodation

T_s (K)	α_E	$\langle E_r \rangle / \langle E_i \rangle$	$\langle E_r \rangle / \langle E_s \rangle$
70	0.82	0.29	2.21
50	0.77	0.30	3.18
20	0.77	0.25	6.79

The energy accommodation coefficients shown in this table indicate that an extreme loss of energy is occurring upon impact with the surface. Analysis of the final velocity components tangent and perpendicular to the surface conclusively demonstrates that *tangential momentum is not conserved* for collisions between SF_6 and an amorphous ice surface of SF_6. The energy exchange diagram shown in Fig. 8 clarifies this point. In this figure $\tilde{v}_r$, θ_r, $\tilde{v}_i$, and θ_i are all determined experimentally. Therefore, by measuring the reflected velocity distribution at a given angle an unambiguous analysis of momentum exchange can be carried out. The α_E values listed in Table I can only be explained by assuming tangential and perpendicular momentum loss, as indicated by the solid triangle whose sides are $\tilde{v}_r$, $\tilde{v}_{tr}$, and $\tilde{v}_{\perp r}$ in Fig. 8. The apparent weak dependence of α_E

on T_s at low surface temperatures (i.e., in the limit of preferentially removing all thermally accommodated SF_6) indicates that impulsive collisions are dominating the scattering.

Similar data was obtained for Kr scattering from krypton ice as a function of T_s. This is shown in Fig. 9 and briefly summarized in Table II.

Table II

Krypton Energy Accommodation

T_s (K)	α_E	$\langle E_r \rangle / \langle E_i \rangle$	$\langle E_r \rangle / \langle E_s \rangle$
40K	0.99	0.14	1.09
25K	0.77	0.29	3.75
20K	0.79	0.26	4.11

Once again the reflected velocity distributions have much higher average velocities than thermally accommodated ones for surface temperatures lower than the beam condensation temperature (T_c(Kr) < 40K). Analysis of the reflected velocity distributions also indicate that tangential momentum is not conserved. The slight deviation of the 40K experimental TOF distribution from the theoretical

curve on its high velocity side may be real, and can possibly
be explained by microscopic reversibility arguments. Very
briefly, one might expect evaporating particles to be
slightly deficient in high velocity events since the con-
densation probability of fast incident particles is less than
that for slowly incident ones.

Finally, and most importantly, we have conducted an
extensive investigation of how translational and internal
energy influence the sticking probability of CCl_4 and SF_6
for collisions involving these molecules and their respective
condensed phases. In Fig. 10 the relative reflection
probability for CCl_4, as a function of incident velocity,
is shown for two different oven temperatures (internal
energies), T_B = 298K and T_B = 560K. These curves were
generated by measuring the relative amount of flux reflected,
as a function of velocity selector setting, for T_S = 90K.
More specifically, the experimental data points were
obtained by normalizing the reflected number density
detected at a given angle, as a function of oven temperature
and velocity selector setting, to the incident beam flux
for the same values of v_i and T_B. Two clear trends can be
seen from the data shown here. First, reflection probability
has a very strong dependence on incident translational
energy, with the probability of reflection increasing

dramatically with increasing incident velocity. Second, the relative reflection probability curves for two different internal energies differ at low incident velocities, and asymptotically merge with each other in the limit of high incident velocity. This is the first indication that the internal energy (i.e., the energy stored in rotation and vibration) of a polyatomic molecule can influence its sticking probability, c, where RP (reflection probability) = 1-c.

The above results, obtained as a function of velocity selector frequency, needed to be deconvoluted with respect to the bandpass function of the selector since the transmitted velocity distributions were fairly wide, having a FWHM $\Delta v/v$ of about 20%. This was accomplished using an iterative, ratio method deconvolution procedure. Following the basic form of Siska's iterative deconvolution procedure[19] we have:

$$f_o(v) \quad = \quad h(v) \tag{2}$$

$$f_{n+1}(v) \quad = \quad f_n(v)[h(v)/g*f_n] \tag{3}$$

where, in our case, h(v) is the experimental (folded) reflection probability for a given velocity selector

setting, $g(v,v')$ is the experimentally determined velocity selector transmission function, and $f_n(v)$ is the nth deconvoluted (unfolded) approximation to $h(v)$. The actual convolution integral, $g*f$, was defined as:

$$g*f_{n+1} = \int_{v_i}^{v_f} dv' g(v,v') f_n(v')$$

$$\approx \sum_{i=1}^{n} g(v,v') f_n(v') \qquad (4)$$

where v_i and v_f are the initial and final velocities transmitted by the selector at a given frequency. The actual $g(v,v')$ distributions were obtained with high resolution single-shot TOF operating at 4 μsec/channel dwell time. The convolution integral was calculated with trapezoidal rule numerical integration. Each successive $h(v)$ was generated by least squares fitting a fourth-order polynomial to $f_n(v)$, where $f_n(v) = RP_n(v)$. After a few iterations, typically 3-5 cycles, the deconvolution procedure converged, and was tested by refolding $f_{n,final}(v)$ with $g(v,v')$:

$$g*f_{n,final} = \int_{v_i}^{v_f} dv' g(v,v') f(v') \approx h(v) \qquad (5)$$

For most velocity ranges it was found that the refolded distribution, $g*f_{n,final}$, virtually reproduced the experimental data, indicating a successful deconvolution. However, for relatively fast velocities ($v \geq 4.5 \times 10^4$ cm/sec) the deconvolution routine experienced difficulties since a very strong function of velocity, $RP(v)$, was being folded with a fairly broad bandpass function. The dashed lines shown in Fig. 10 represent the results of this $RP(v)$ deconvolution for CCl_4.

The internal energy dependence of condensation probability can be expressed in a quantitative manner by plotting the ratio of the refleciton probability curves, for different oven temperatures, as a function of incident velocity. We have explicitly calculated the *reflection enhancement factor*, EF, which is actually the ratio of relative reflected fluxes for molecules having the same translational velocity, v_i, and different internal energies:

$$EF(T_s = 90K, v_i) = \frac{(\text{Fraction of flux reflected}; T_B = 560K)}{(\text{Fraction of flux reflected}; T_B = 298K)} \quad (6)$$

$$= \frac{\left(\dfrac{n_r^{90} \, v_r^{90}}{\text{Incident flux } (T_B; v_i)} \right) \Big|_{T_B = 560K}}{\left(\dfrac{n_r^{90} \, v_r^{90}}{\text{Incident flux } (T_B; v_i)} \right) \Big|_{T_B = 298 K}}$$

where n_r^{90} and v_r^{90} are the reflected number densities

and velocities at T_s = 90K for each beam temperature.

Figure 11 shows the EF values determined for CCl_4, which

were obtained from Fig. 10 using equation (6). The

solid line in Fig. 11 corresponds to the reflection

enhancement factor that was calculated with the experi-

mental RP(v) curves, while the dashed line corresponds

to the deconvoluted result. The EF curves shown in

this figure conclusively demonstrate that internal

excitation of a molecule's rotational and vibrational

degrees of freedom leads to an increase in its reflec-

tion probability (decrease in sticking probability) in

the limit of low incident velocity. EF $\approx$ 4 implies that

internally excited CCl_4 molecules with $<v_i> \approx 2.7 \times 10^4$

cm/sec are four times more likely to scatter from the

CCl_4 ice suface than vibrationally and rotationally

"cool" ones. Furthermore, the EF curves shown in this

figure indicate that in the limit of high incident

velocities EF goes asymptotically to unity, indicating

that internal excitation has little influence upon con-

densation probability for high energy particles. This

will be discussed in detail in the next section of this

paper. Note that the actual v_r^{90} values which appear

in equation (6) were not experimentally determined here,

and that the EF values shown in Fig. 11 were calculated

assuming equal reflected velocities for scattered molecules which had the same incident velocities but differing internal energies. In reality, the scattered molecules which were initially internally excited may scatter with slightly larger reflected velocitie   The EF val..r of Fig. 11 may therefore be viewed as lower bound estimates for enhanced scattering due to internal excitation.

Figures 12 and 13 show respectively the reflection probability curves and reflection enhancement factors for SF_6 with oven temperatures of 300K and 608K, as a function of incident velocity. The solid lines once again correspond to the experimental distributions while the dashed lines are the deconvoluted results. The qualitative shapes of these curves are quite similar to those found for CCl_4, indicating that internal excitation can inhibit condensation in the limit of low incident translational energy. The velocity range explored in these experiments could not be extended to include velocities lower than about 2.5×10^4 cm/sec or higher than 5.5×10^4 cm/sec due to the extremely low signal level of the $T_B \sim 300K$ data in these velocity regimes. The RP(v) and EF(v) curves shown in Figs. 10-13 are the main results of this series of beam-surface scattering experiments.

Extreme care was taken to guarantee that these reflection probability distributions were not an artifact

of some systematic experimental error. The reflection
probability was monitored in a series of tests as a
function of beam intensity, and was found to linearly
track the beam intensity. This indicated that impurities
on the surface (from background gas in the scattering
chamber) were not significantly affecting the results.
More importantly, the actual transmitted velocity distri-
butions for the hot and room temperature source settings
were not always superimposable for the same velocity
selector frequency. This occurred since the bandpass
function of the selector was folded with the shape of
the flux distribution effusing from the quartz slot.
At high velocities the long tail of the high temperature
flux distributions skewed the transmitted velocity
distributions to higher velocities. Figures 14 and 15
show the actual incident CCl_4 and SF_6 velocity distri-
butions, as a function of velocity selector frequency,
for both room temperature and elevated source temperatures.
These curves were obtained by taking TOF measurements with
the detector looking directly into the transmitted beam.
The low frequency distributions for hot and room temperature
beams virtually superimpose for both CCl_4 and SF_6, while
at higher frequencies the hot distributions are noticeably
skewed to higher velocities. The virtual overlap of the

low frequency distributions for different source temperatures is quite fortunate as the low velocity data points in Figs. 10-13 are the most crucial ones for supporting the presence of internal energy effects. Nevertheless, the experimental EF curves shown in Figs. 11 and 13 have been corrected for these shifts, and the successful deconvolution of the data with respect to the actual incident velocity distributions exactly corrected for the problem.

DISCUSSION

The results shown in the preceeding section clearly indicate that the internal energy of a polyatomic molecule becomes increasingly more important in determining its sticking probability as its translational energy is decreased. This can be understood in terms of the energy loss which must occur in the direction perpendicular to the surface for condensation to occur. A simple energy level schematic for gas-surface scattering is shown in Fig. 16. The potential energy well in this figure represents the gas-surface interaction potential, E_1 and E_2 represent low and high energy incident trajectories referenced to the dissociation limit of the gas-surface

potential, and ΔL, as drawn, indicates the total energy
loss which ultimately occurs for the L_1 trajectory if it
becomes trapped and subsequently accommodated to T_s, for
low T_s values. In this simplified picture of the conden-
sation process the extent of *initial* energy loss in the
direction normal to the surface determines whether a
particle becomes trapped, and subsequently accommodated to
T_s, or whether it will inelastically scatter from the sur-
face. For trapping to occur the low and high energy
trajectories must lose at least L_1 and L_2, respectively,
upon initial impact with the repulsive wall of the gas-
surface interaction potential. Energy losses less than
these critical amounts will lead to "direct inelastic"
scattering events which have a strong memory of their
initial state. As the translational energy of an incident
molecule is increased we therefore see that increasingly
more energy must be lost in the initial collision for
condensation to occur. The steadily decreasing probability
that this threshold energy loss will occur for increasing
incident translational energy gives rise to the RP(v)
curves shown in Figs. 10 and 12 for CCl_4 and SF_6. In the
limit of *high* incident translational energy we would there-
fore expect that coupling of internal energy (rotation,
vibration) to translation upon impact with the repulsive
wall of the gas-surface potential (i.e., $V, R \rightarrow T$ collisional

energy transfer) would have very little influence on the
condensation probability for the molecule. Conversely,
this overview of the condensation process seems to indicate
that any collisional V,R · T energy exchange for *slowly*
incident molecules would lead to a significant decrease
in that molecule's sticking probability, as is experi-
mentally found, and shown in Figs. 11 and 13.

Since gaseous condensation is essentially a problem
of translational accommodation, it is interesting to
compare the relative effectiveness of internal and trans-
lational energy for inhibiting sticking. Using the vibra-
tional quantum partition function for an ideal polyatomic
molecule, the mean vibrational energy difference between
CCl_4 at 298K and 560K is found to be ca. 3.7 kcal/mole,
while the rotational energy change between these two
temperatures is well approximated by $3/2 \, k\Delta T$, or ca. 0.8
kcal/mole. In going from 2.7×10^4 cm/sec to 5.0×10^4
cm/sec the CCl_4 translational energy increases from about
1.3 to 4.5 kcal/mole. Over this velocity range the de-
convoluted $T_B = 300K$, $RP(v)$ curve for CCl_4 increased
by a factor of about 15, while the largest EF found was
only about 4. Therefore translational energy appears
to be more "efficient" per unit of energy than internal
energy in inhibiting condensation. This comparison is

not totally fair as all of the internal modes certainly
do not collisionally couple to translation upon impact.
However, the trend outlined above is probably representative
of the behavior exhibited by relatively large polyatomic
molecules. Similar calculations for SF_6 lead to the
same qualitative result as above. The increase in vibra-
tional energy for SF_6 in going from T_B = 390K to 608K
is found to be about 8.3 kcal/mole, while the gain in
rotational energy is 0.9 kcal/mole. Similarly, its trans-
lational energy increases from 1.3 to 4.4 kcal/mole upon
increasing its mean incident velocity from 2.7×10^4 to
5.0×10^4 cm/sec. The SF_6 T_B = 500K, RP(v) curve increased
by a factor of ~10 over this translational energy range,
while EF for the most favorable case was only about 4.6.

Finally, it must be emphasized that the internal
energy reflection enhancement factor should probably be
treated theoretically with a dynamic, collisional energy
transfer description akin to gas phase inelastic scattering
models. Adsorption-reevaporation models, such as those
proposed by several Russian groups at the Lebedev
Institute,[1,4] are totally inadequate for describing the
results found in this experiment.

CONCLUSION

Molecular beam surface scattering experiments have been carried out which have shown that the internal energy of a molecule can significantly influence its sticking probability upon collision with an amorphous ice of its own condensed phase. This internal energy effect is greatest for molecules having relatively low incident translational energies. For CCl_4 and SF_6 the largest reflection enhancement factors found, as defined in this paper, were respectively 3.7 and 4.6. Reflected particle velocity analysis carried out with cross-correlation time-of-flight techniques has revealed that a very large degree of translational energy accommodation is occurring for inelastically scattered SF_6 molecules, with thermal accommodation coefficients, α_E, as large as 0.77 being achieved. The weak surface temperature dependence of α_E found for Kr and SF_6 in the limit of low surface temperature implies that impulsive collisions are dominating the observed scattering events. Tangential momentum is not conserved in these collisions. Finally, these studies were conducted in the limit of very high sticking probability ($\geq$ 99%) so that the trapped (accommodated) molecules would be essentially frozen out upon impact with the surface, leaving only the "direct

inelastic" scattering events contributing to the detected
signal. This condition is highly advantageous as the
directly scattered molecules contain the important
dynamic and energy exchange information sought after in
this experiment.

REFERENCES

1. K. S. Gochelashvili, N. V. Karlov, A. N. Orlov, R. P.
    Petrov, Yu. N. Petrov, and A. M. Prokhorov, Zh. Eksp. Teor.
    Fiz. Pis. Red. $\underline{21}$, 640 (1975) [JETP Lett. $\underline{21}$, 302 (1975)].

2. N. V. Karlov and K. V. Shaĭtan, Zh. Eksp. Teor. Fiz.
    $\underline{71}$, 464 (1976) [Sov. Phys. JETP $\underline{44}$, 244 (1976)].

3. J. D. Doll, J. Chem. Phys. $\underline{66}$, 5709 (1977).

4. N. F. Basov, E. M. Belenov, V. A. Isakov, Yu. S. Leonov,
    E. P. Markin, A. N. Oraevskii, V. I. Romanenko, and
    N. B. Ferapontov, Zh. Eksp. Teor. Fiz. Pis. Red. $\underline{22}$,
    221 (1975) [JETP Lett. $\underline{22}$, 102 (1975)].

5. K. S. Gochelashvili, N. V. Karlov, A. I. Ovchenkov,
    A. N. Orlov, R. P. Petrov, Yu. N. Petrov, and A. M.
    Prokhorov, Zh. Eksp. Teor. Fiz. $\underline{70}$, 531 (1976) [Sov.
    Phys. JETP $\underline{43}$, 274 (1976)].

6. G. K. Anderson and J. T. Lee, Opt. Lett. $\underline{3}$, 10 (1978).

7. C. N. Stewart and G. Ehrlich, J. Chem. Phys. $\underline{62}$, 4672
    (1975).

8. J. T. Yates, Jr., J. J. Zinck, S. Sheard, and W. H.
    Weinberg, J. Chem. Phys. $\underline{70}$, 2266 (1979).

9. S. G. Brass, D. A. Reed, and G. Ehrlich, J. Chem. Phys.
    $\underline{70}$, 5244 (1979).

10. A. Gelb and M. J. Cardillo, Surf. Sci. $\underline{64}$, 197 (1977).

11. S. J. Sibener and Y. T. Lee, Proceedings of the XIth
     International Symposium on Rarefield Gas Dynamics,
     Cannes, France, 1978, in press.

12. Y. T. Lee, J. D. McDonald, P. R. LeBreton and D. R.
     Herschbach, Rev. Sci. Instrum. 40, 1402 (1969).

13. J. S. Ahearn, Jr., J. P. Monaghan, Jr., and J. W.
     Mitchell, Rev. Sci. Instrum. 41, 1853 (1970).

14. T. P. Schafer, Ph.D. dissertation, the University
     of Chicago, Chicago, Illinois, 1972.

15. K. Sköld, Nucl. Instrum. Meth. 63, 114 (1968).

16. V. L. Hirschy and J. P. Aldridge, Rev. Sci. Instrum.
     42, 381 (1971).

17. R. W. Zwanzig, J. Chem. Phys. 32, 1173 (1960).

18. R. M. Logan and R. E. Stickney, J. Chem. Phys. 44,
     195 (1966).

19. P. E. Siska, J. Chem. Phys. 59, 6052 (1973).

FIGURE CAPTIONS

Fig. 1. Assembly diagram of the experimental scattering
         apparatus. In later experiments a closed-cycle
         helium refrigerator replaced the liquid nitrogen
         cooling of the target substrate.

Fig. 2. Upper section: T_s = 280K CCl_4 experimental
         angular distribution. The solid line is a plot
         of the cosine (θ) function. Lower section:
         Angular distribution obtained at a sticking
         probability of ca. 90%. This curve exhibits
         characteristics belonging to both peaked and
         cosine scattering. The arrows indicate the
         specular angle in each of these figures.

Fig. 3. Reflected velocity distributions for SF_6 scatter-
         ing from a room temperature (dirty) surface.
         The dashed lines represent Maxwellian flux dis-
         tributions for 324K. This figure confirms thermal
         accommodation for incident molecules. The three
         velocity selector frequencies correspond to mean
         incident translational velocities of about 2.0 x
         10^4, 3.5 x 10^4, and 5.0 x 10^4 cm/sec.

Fig. 4. Angular distributions obtained for two trans-
         lational velocities with T_B = 298K. This data
         was taken at a sticking probability of $\geq$ 99.5%.

Fig. 5.   Angular distributions for internally excited CCl_4 taken at a sticking probability of $\geq 99.5\%$.

Fig. 6.   Angular distributions for three different incident SF_6 velocities with $T_B = 300K$ and $608K$. These distributions were obtained in the limit of very low T_s, at a sticking probability of $\geq 99.5\%$

Fig. 7.   Reflected SF_6 velocity distributions as a function of decreasing surface temperature. The dashed lines in each section of the figure are the calculated Maxwellian flux distributions for each T_s value. The onset of SF_6 condensation occurs at $\sim 79K$.

Fig. 8.   Schematic velocity diagram for gas-surface scattering events. $\vec{v}_{tr}^{cube}$ represents the tangential velocity vector within the "hard-cube" approximation.

Fig. 9.   Reflected krypton velocity distributions as a function of surface temperature, taken at the specular angle. The dashed lines in each section of the figure are the calculated Maxwellian flux distributions for each T_s value.

Fig. 10. CCl_4 reflection probability as a function of incident velocity for $T_B = 298K$ and $560K$. The dashed lines are the deconvoluted reflection probability curves for which the finite bandpass function of the velocity selector has been taken into account.

Fig. 11. Internal energy reflection enhancement factor
curve for CCl_4 as a function of incident velocity.
EF = 4 implies that internally hot (560K) CCl_4
molecules have a four times higher probability
of being reflected from a cold (90K) surface than
do room temperature molecules. The dashed line
is the deconvoluted EF curve for which the finite
bandpass function of the velocity selector has
been taken into account.

Fig. 12. SF_6 reflection probability as a function of
incident velocity for T_B = 300K and 608K. The
dashed lines are the deconvoluted reflection prob-
ability curves for which the finite bandpass
function of the velocity selector has been ta'en
into account.

Fig. 13. Internal energy reflection enhancement factor
curve for SF_6 as a function of incident velocity.
The dashed line is the deconvoluted EF curve for
which the finite bandpass function of the velocity
selector has been taken into account. The dotted
line is an extrapolation of the deconvoluted EF
curve to v_i = 5.5 x 10^4 cm/sec.

Fig. 14. Experimentally determined CCl_4 incident flux
distributions, as a function of velocity selector
frequency, for T_B = 298K and 560K.

Fig. 15. Experimentally determined SF_6 incident flux distri-
butions, as a function of velocity selector fre-
quency, for T_B = 300K and 608K.

Fig. 16. Schematic energy diagram of a gas-surface inter-
action potential.

Liquid nitrogen inlet

ROTATABLE COOLED SURFACE

TO MASS SPECTROMETER

Outlet

Embedded surface heaters (not shown)

Chopper

Velocity selector

Effusive source

Wire heater

1200 ℓ/sec

1800 ℓ/sec

Gas inlet
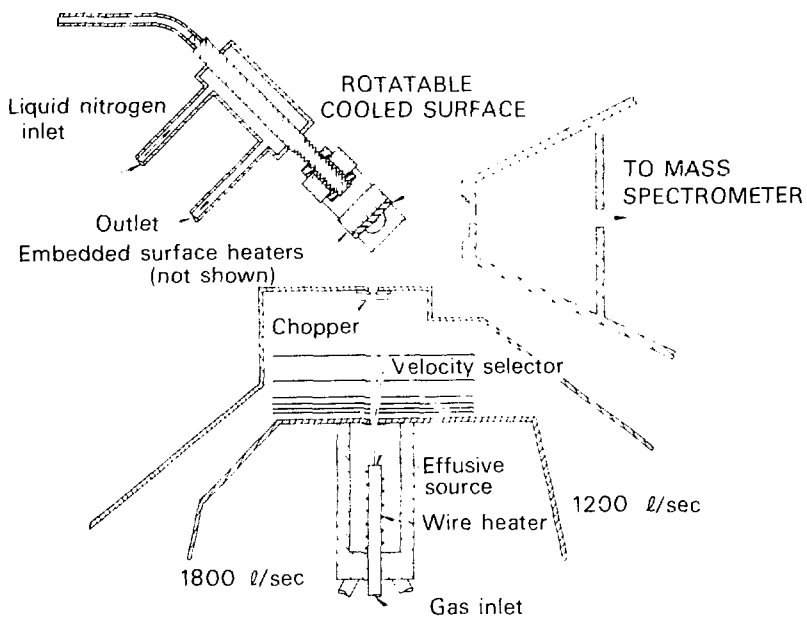
XBL 7712-10907
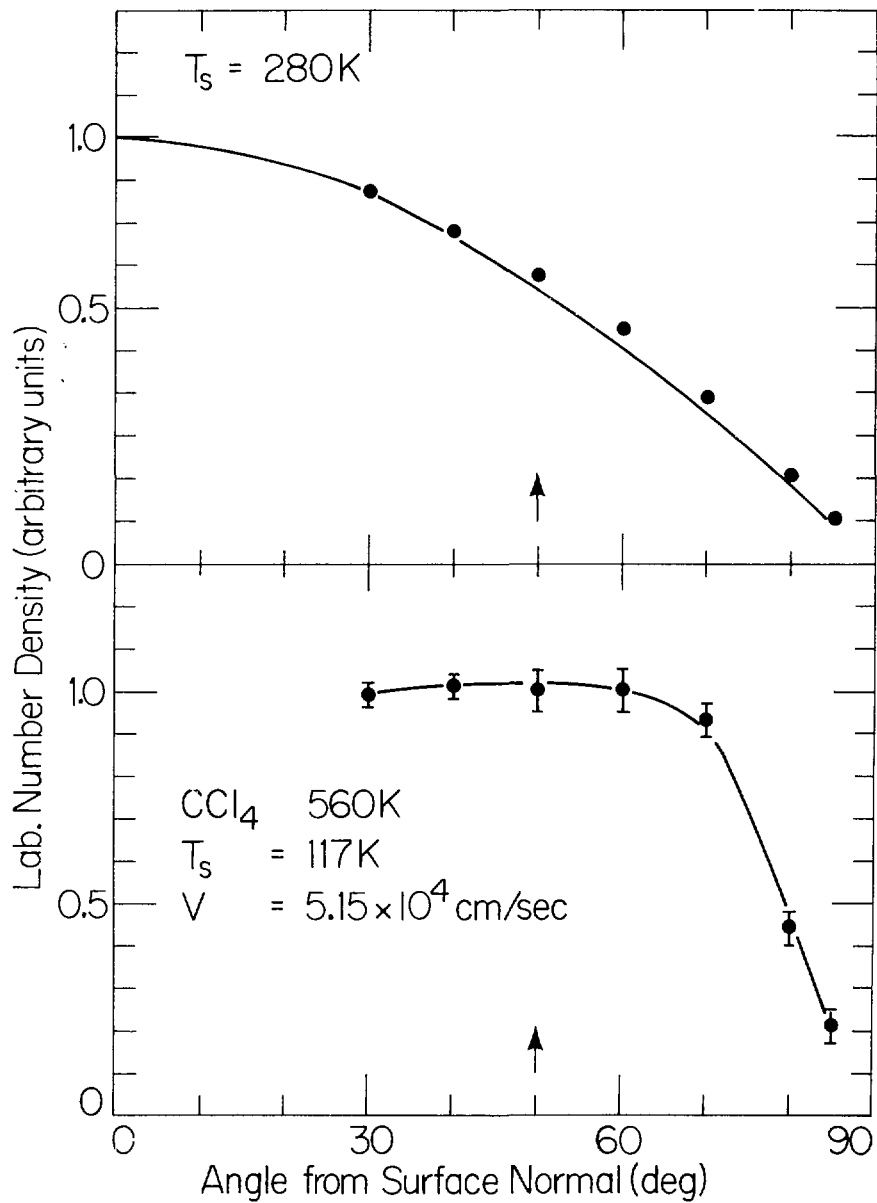
Fig. 1

Fig. 2

XBL799-2817
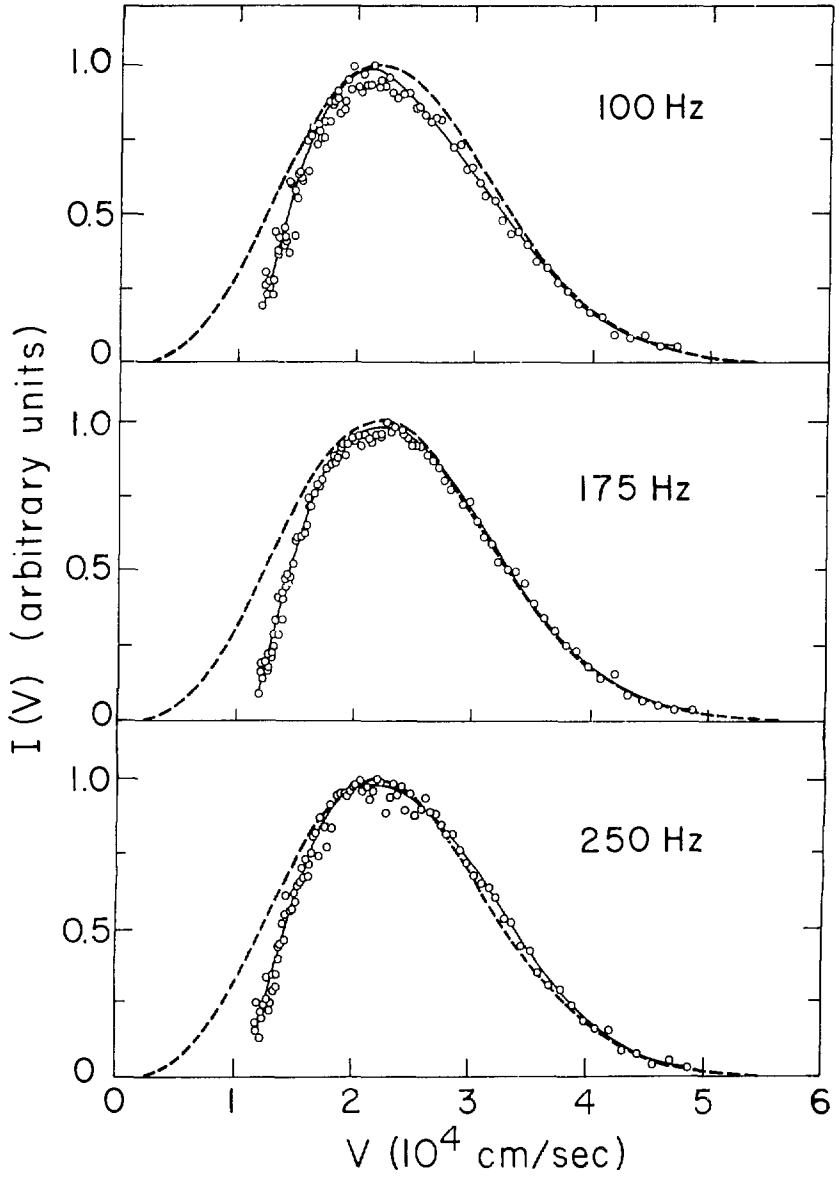
Fig. 3   XBL 7810- 6003
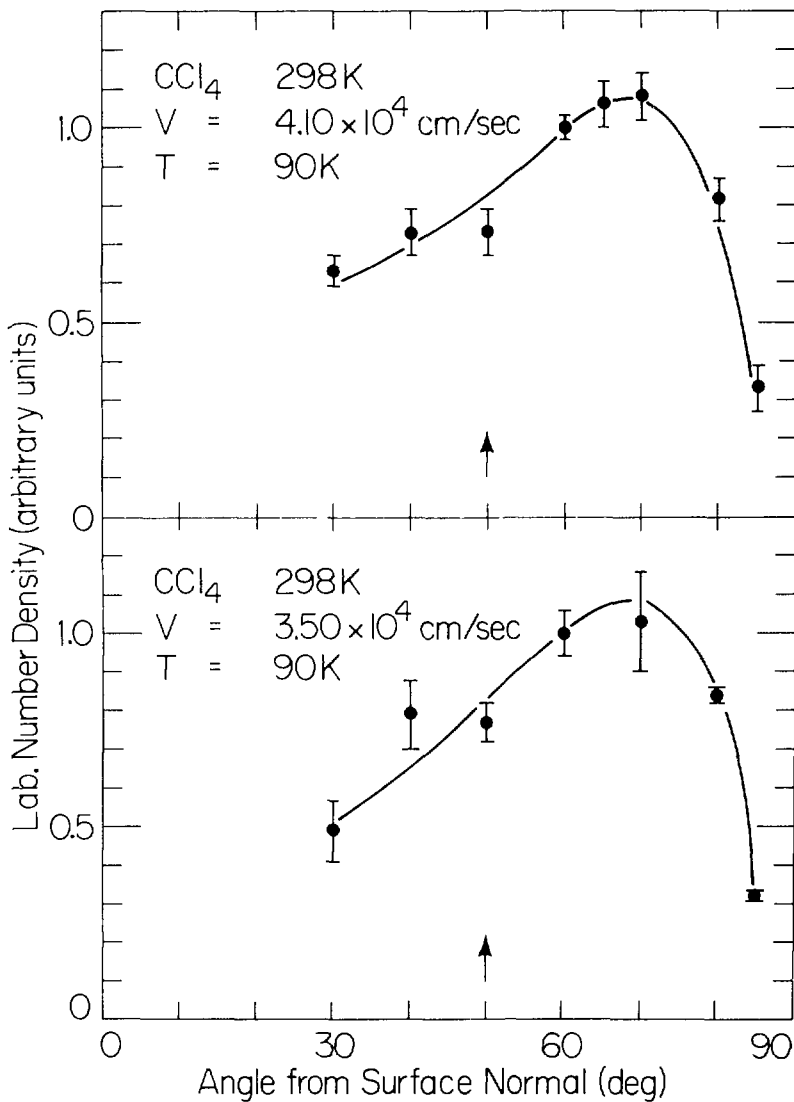
Fig. 4

XBL 799-2815

Fig. 5

XBL 7711-10905
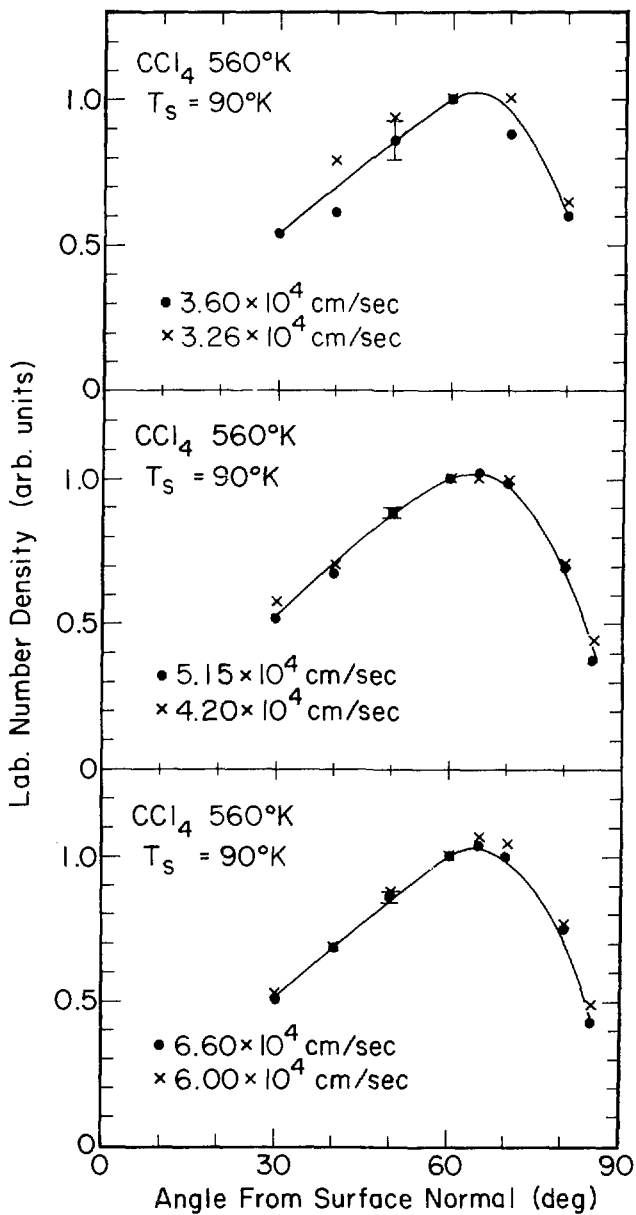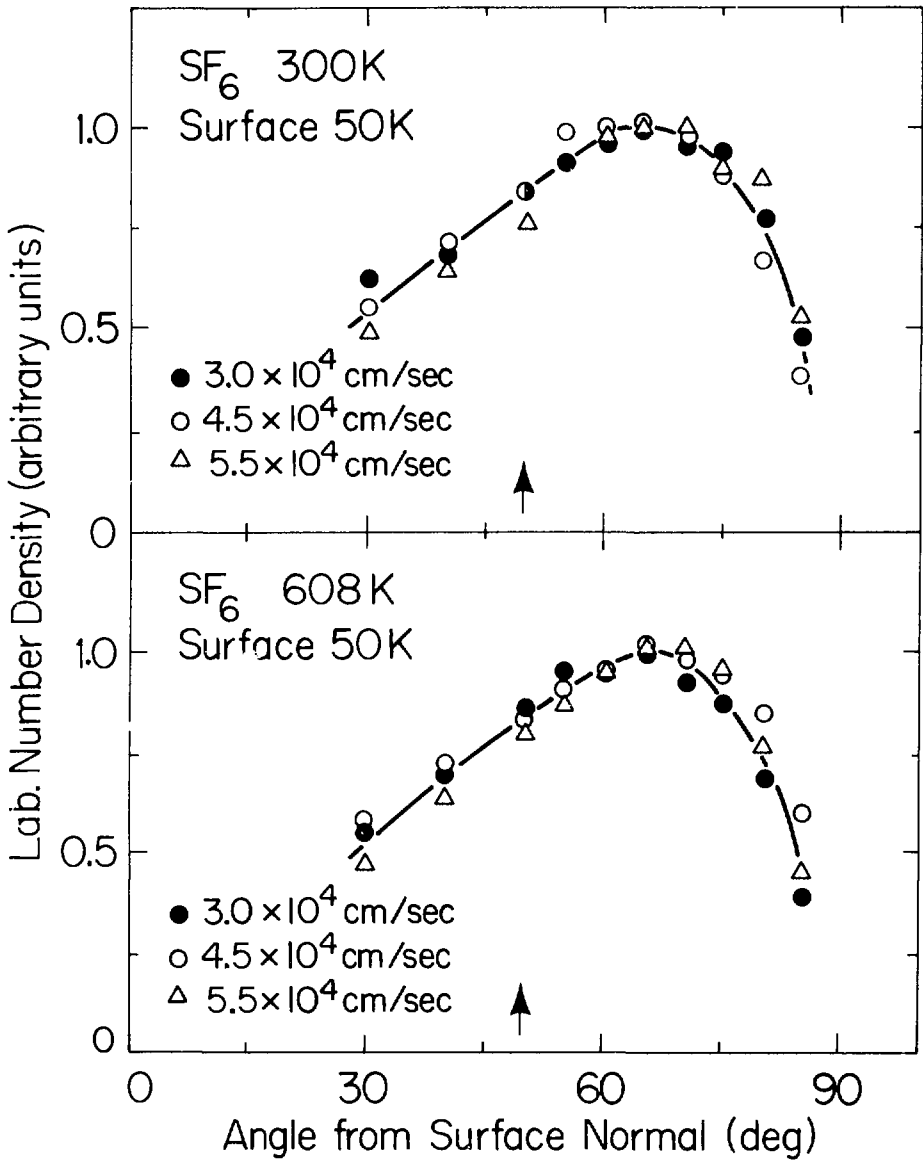
Fig. 6
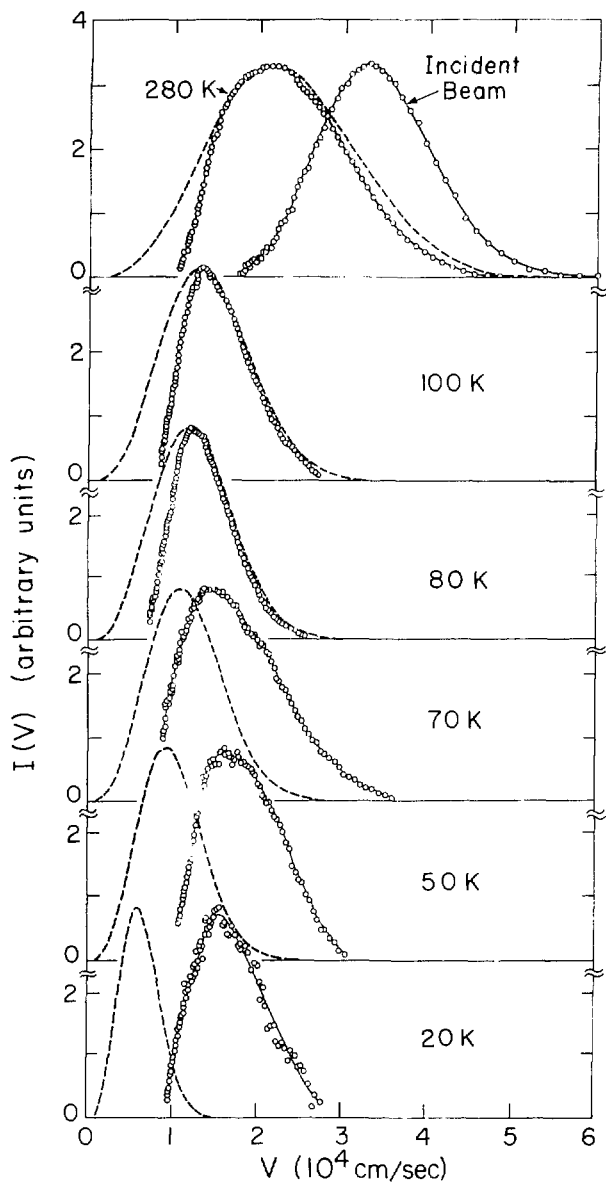
XBL 799-2816

Fig. 7

XBL 7810-5945

ENERGY ACCOMMODATION

$$\alpha_E \equiv \frac{E_i - E_r}{E_i - E_s}$$
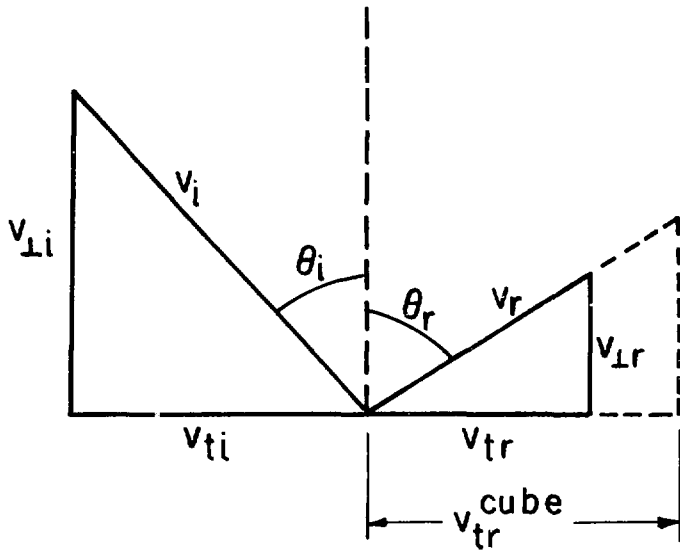
Fig. 8
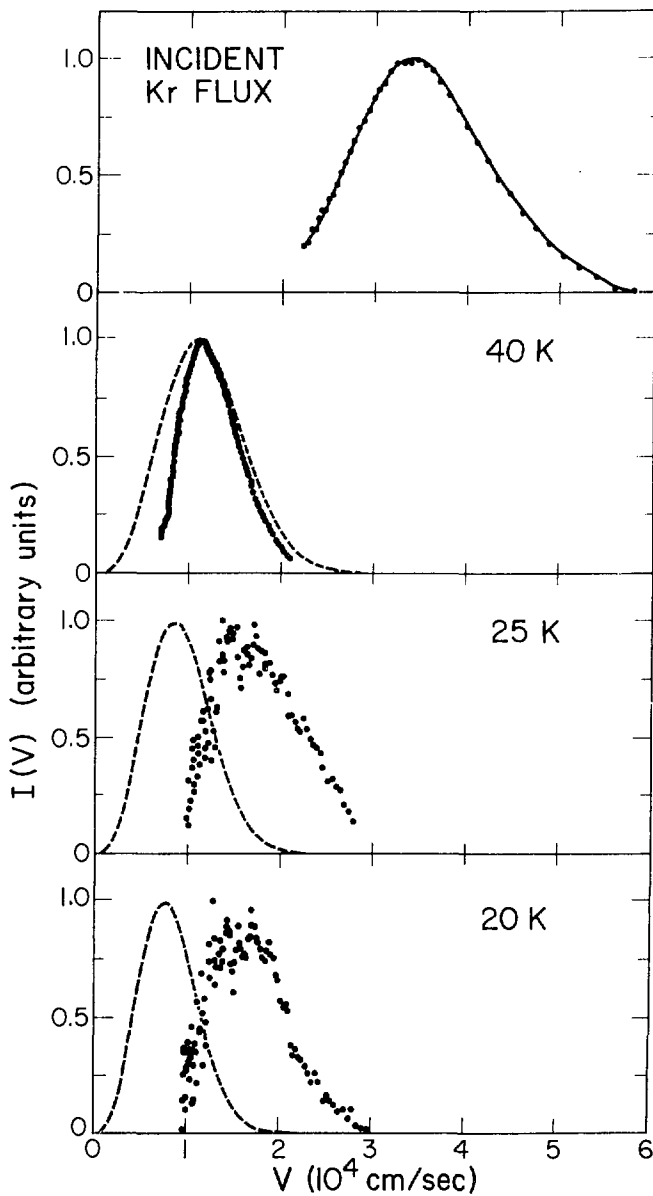
XBL 7810-11636

Fig. 9
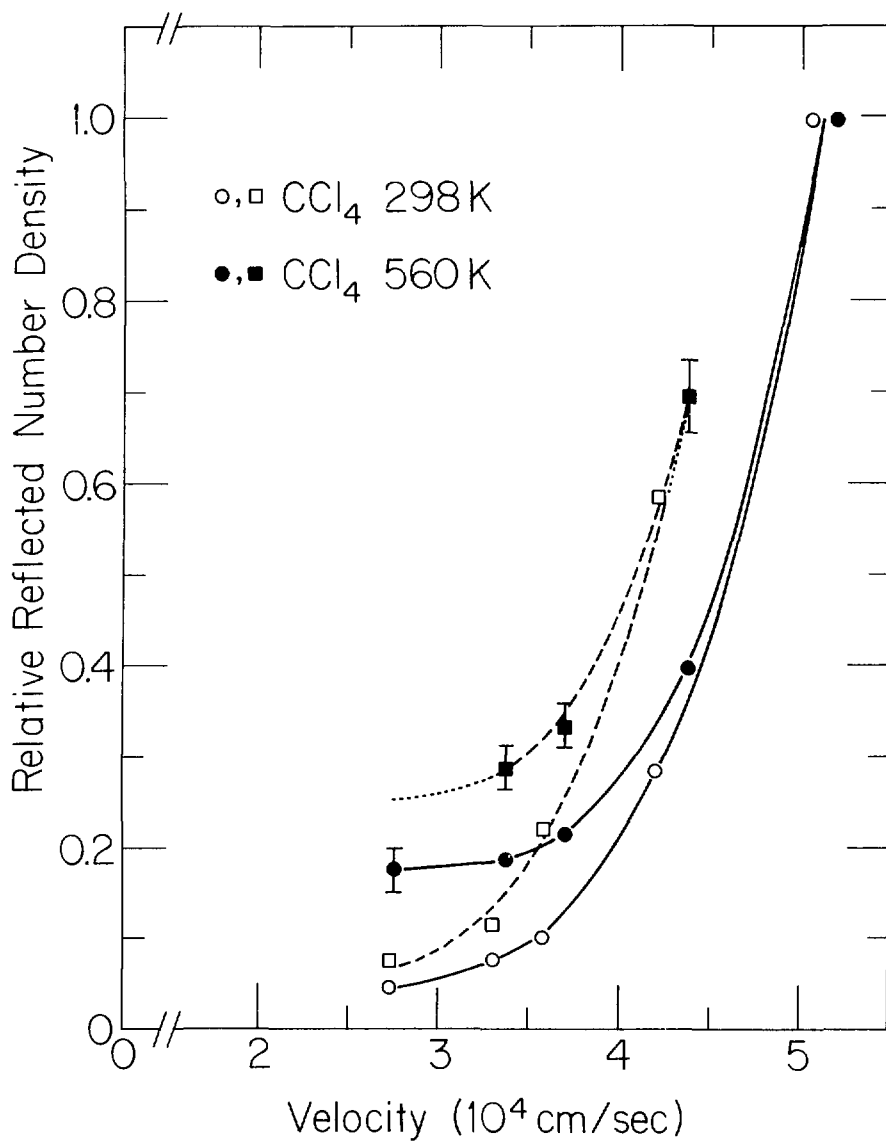
Fig. 10

XBL 799-2806

Fig. 11

EF for CCl$_4$
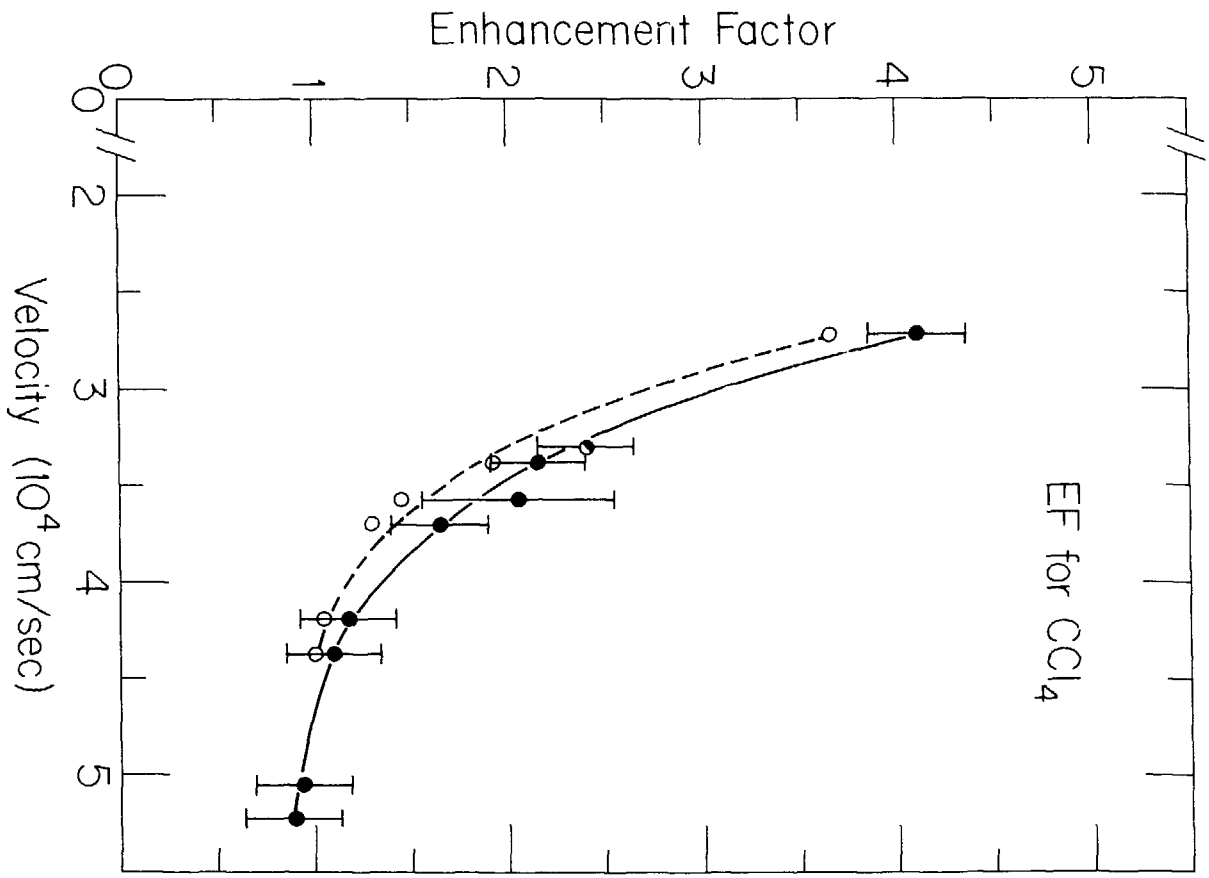
XBL799-2805

Fig. 12   XBL799-2818

EF for SF$_6$

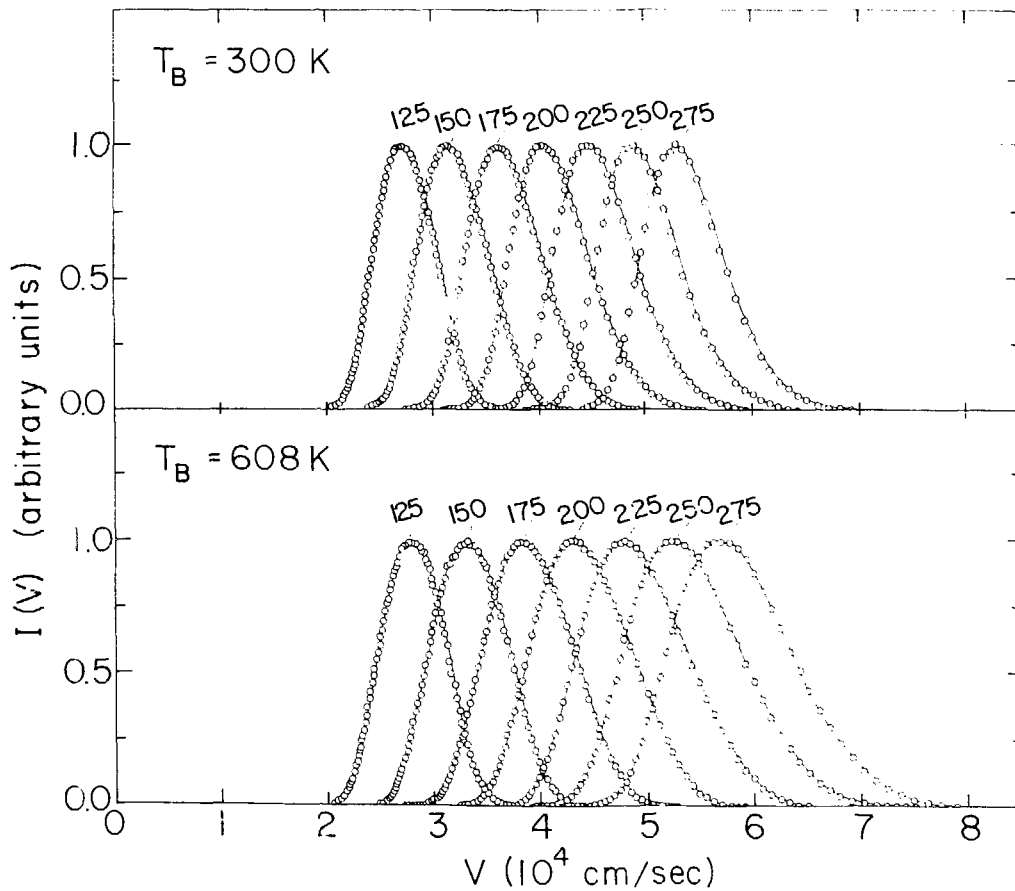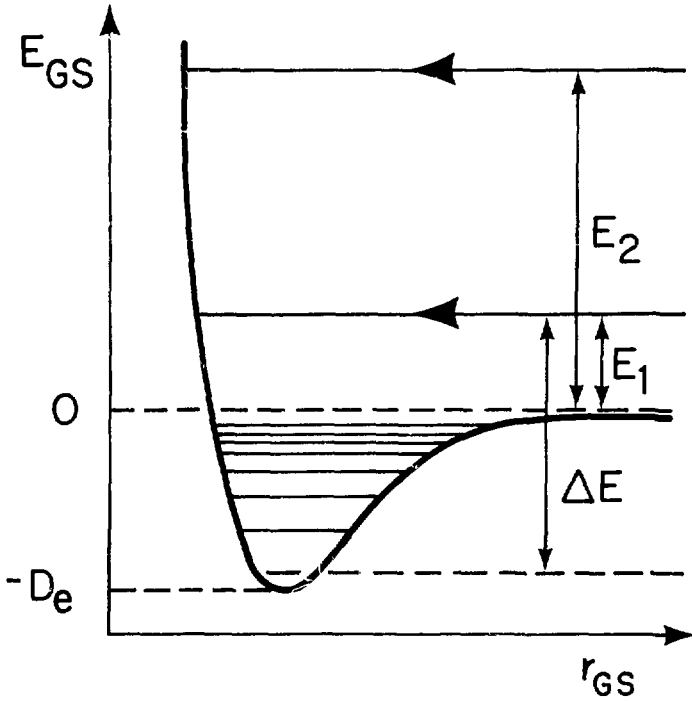Enhancement Factor

Velocity (10^4 cm/sec)
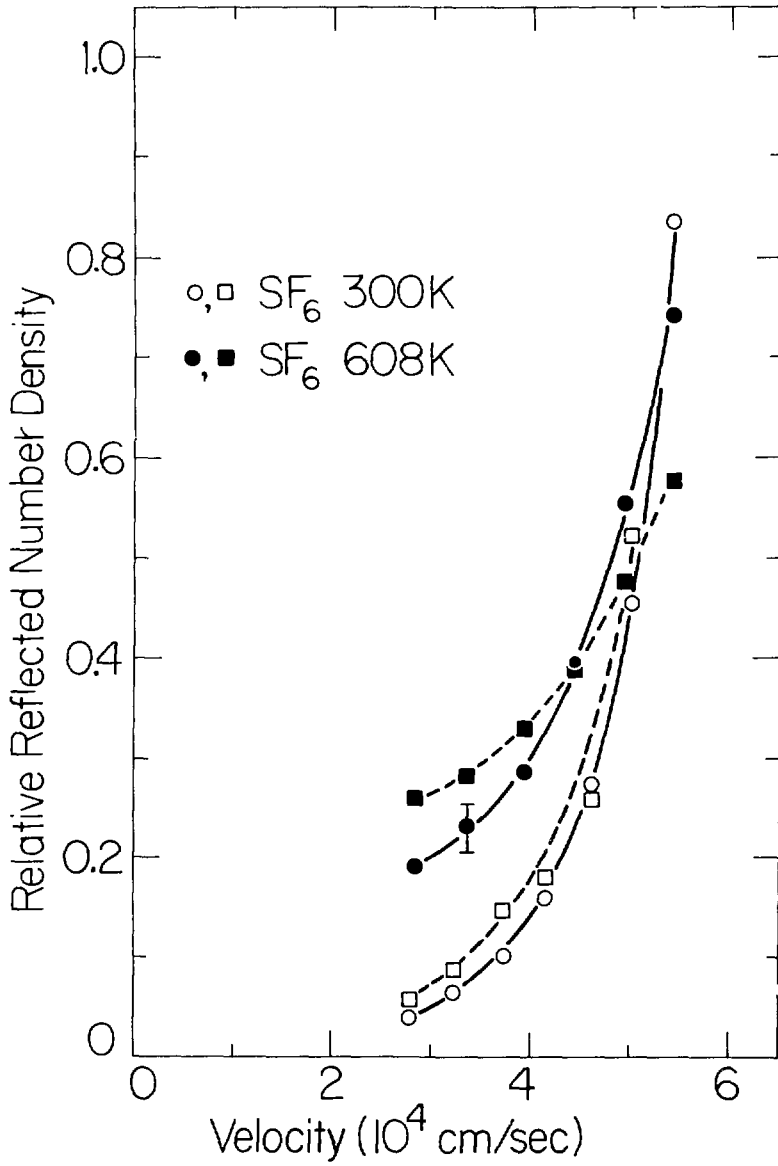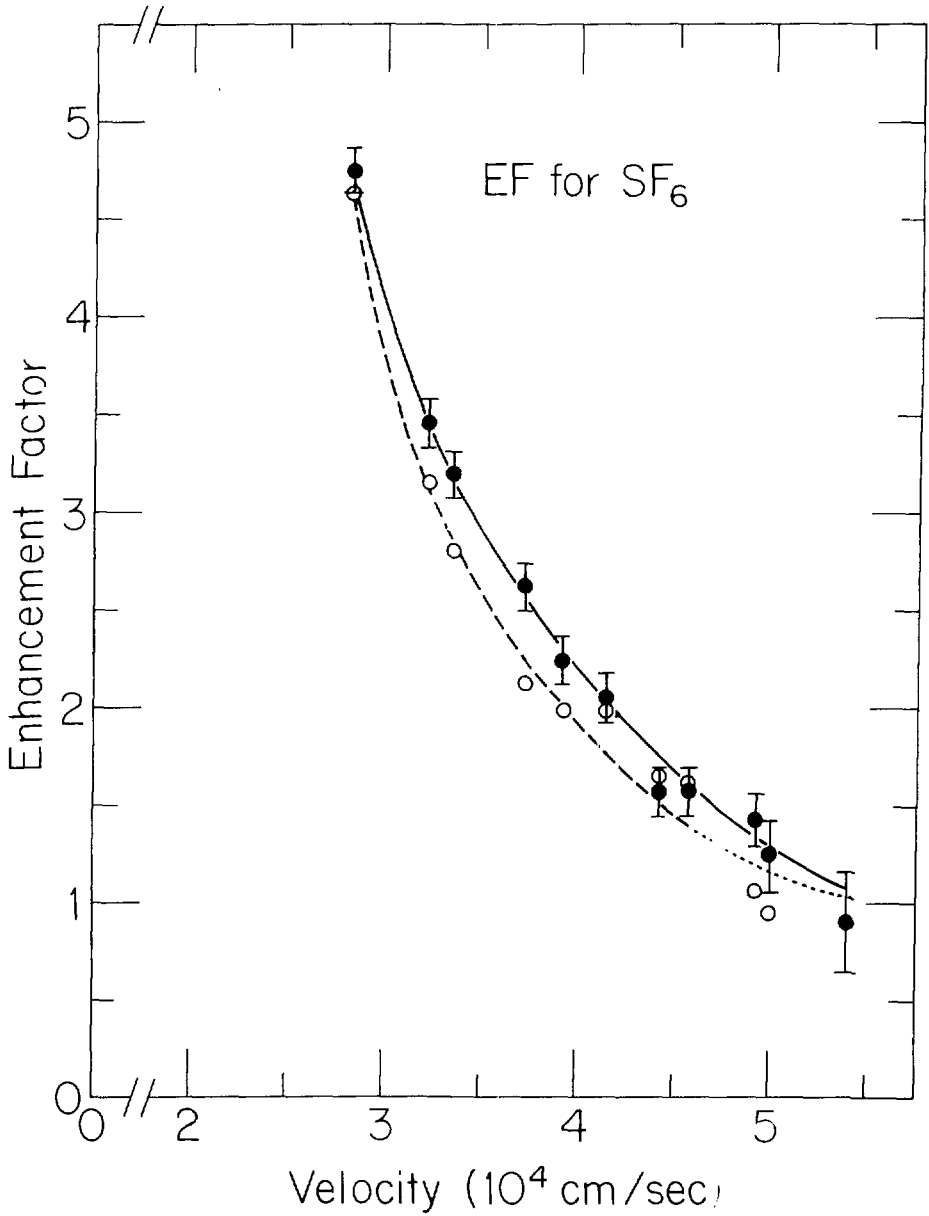
Fig. 13
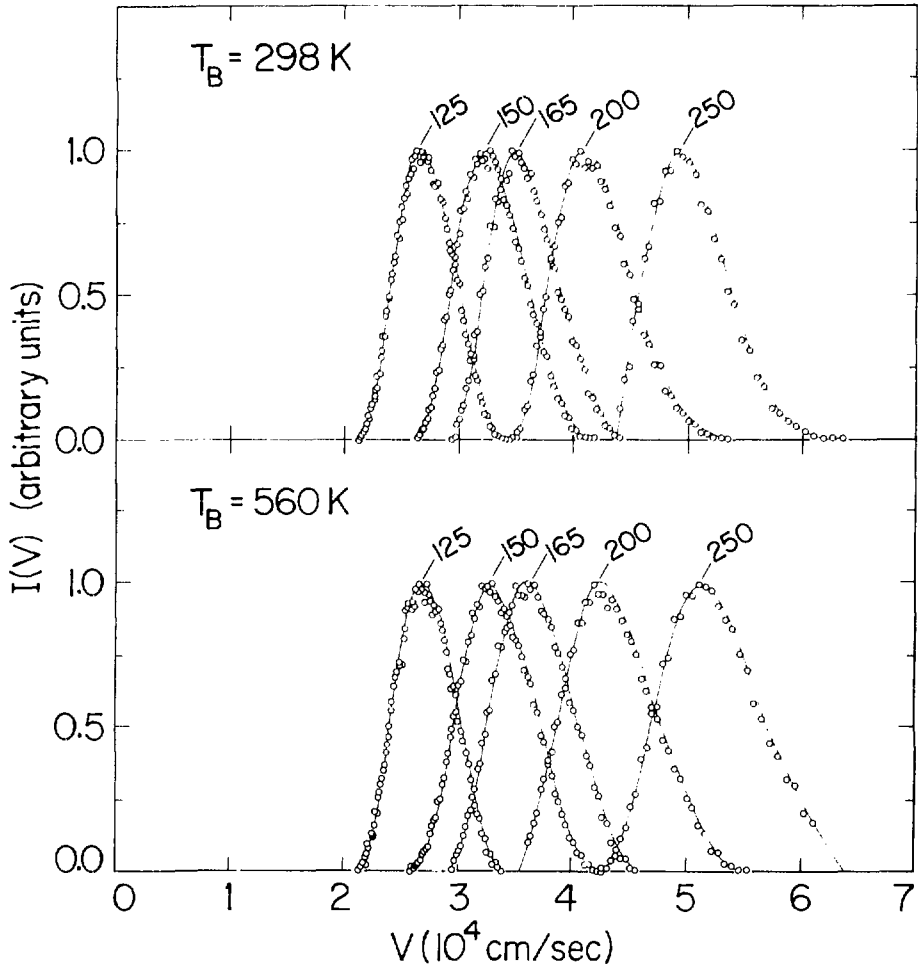
XBL799-2807

Fig. 14

XBL 799-2813

Fig. 15

XBL 7810-5940

XBL799-2814

Fig. 16